University of Leoben
Chair of Casting Research
Department of Metallurgy
Univ.Prof. Dipl.-Ing. Dr. Peter Schumacher

Master Thesis

Topic:

Aspects of grain refinement in copper alloys

by

Andreas Cziegler, BSc.

Supervisor:

Univ. Prof. Dipl.-Ing. Dr. Peter Schumacher

Innovation in Motion Miba

Leoben, April 2015

Statutory Declaration

I declare in lieu of oath, that I wrote this thesis and performed the associated research myself, using only literature cited in this volume.

Eidesstattliche Erklärung

Ich erkläre an Eides statt, dass ich diese Arbeit selbständig verfasst, andere als die angegebenen Quellen und Hilfsmittel nicht benutzt und mich auch sonst keiner unerlaubten Hilfsmittel bedient habe.

Date	Andreas Cziegler

Acknowledgement

This work was carried out at the Chair of Casting Research at the University of Leoben in cooperation with MIBA Gleitlager GmbH.

Therefore, I would like to thank Univ. Prof. Dipl.-Ing. Dr. Peter Schumacher for the supervision of this thesis. I would also like to thank the MIBA Gleitlager GmbH, Dipl.-Ing. Alexander Eberhard and the Österreichische Forschungsförderungs-gesellschaft (FFG).

Furthermore, I would like to thank Mr. Winfried Fischer, the technician of the Chair of Casting Research for his support.

Abstract

The purpose of this work was to investigate the grain refinement mechanism of copper alloys. The literature review showed that the grain refinement of copper and copper alloys seems to be a complex mechanism that is strongly dependent on the alloy system, the range of the alloying elements, the impurities and the casting conditions. As grain refinement depends on nucleation and growth restriction the growth restriction factors of the alloying elements of the copper-system were calculated using binary phase diagrams. A comprehensive list containing 63 alloying elements ranked according to their growth restriction factor was given. It was shown that phosphorus is the most powerful segregant in the copper-system, followed by beryllium and lithium. In addition to the growth restriction factor suitable nucleation sites for copper alloys were examined. More than 1000 compounds were observed according to their lattice disregistry to the copper lattice with a focus on binary compounds. Regarding the lattice disregistry and the melting point it was shown that SrO, ZrO_2 and BN are the most suitable compounds acting as nucleants in copper alloys. Based on the calculation of the growth restriction factor melting experiments were carried out to validate the influence of the addition of tin, zinc, phosphorus, magnesium and iron on the variation of the grain size of high purity copper. The addition of phosphorus was found to decrease the grain size, whereas the addition of tin, zinc, magnesium and iron was found to increase the grain size. The variation of the grain size is assumed to be of a complex interaction between the growth restriction factor, and its effect on constitutional undercooling and growth restriction by influencing the growth velocity and therefore latent heat release, and the cooling rate. Furthermore, the cooling rate is assumed to be affected to a great extent by the decrease of thermal conductivity of the columnar zone at the mould and by the variation of latent heat release with increasing solute content.

Kurzfassung

Ziel der Arbeit war es, die Grundlagen der Kornfeinung von Kupferlegierungen zu erarbeiten. Eine vorhergehende Literatursuche zeigte, dass die Kornfeinung in Kupfer und Kupferlegierungen in großem Maße vom Legierungssystem, dem Gehalt der Legierungselemente, den Verunreinigungen und den Prozessbedingungen abhängt. Da die Kornfeinung sowohl über die effiziente Keimbildung, als auch über die Wachstumsbehinderung bestimmt wird, wurden im ersten Schritt die Wachstumsbehinderungsfaktoren der Legierungselemente des Kupfers über binäre Phasendiagramme berechnet. Darauf aufbauend konnte eine umfangreiche Liste mit 63 Legierungselementen, gereiht hinsichtlich ihres Wachstumsbehinderungsfaktors, erstellt werden. Es zeigte sich, dass Phosphor die höchste wachstumsbehindernde Wirkung im Kupfer aufweist, gefolgt von Beryllium und Lithium. Im zweiten Teilbereich der Arbeit wurden geeignete Verbindungen, die als Keimstellen wirken können, untersucht. Über 1000 Verbindungen wurden hinsichtlich ihres Passungsfehlers zum Kristallgitter des Kupfers betrachtet, wobei das Hauptaugenmerk auf binäre Verbindungen gelegt wurde. Unter Berücksichtigung des Passungsfehlers und des Schmelzpunktes erwiesen sich SrO, ZrO_2 und BN als die geeignetsten Verbindungen. Aufbauend auf der Berechnung der Wachstumsbehinderungsfaktoren wurden Schmelzversuche durchgeführt, um die Wirkung der Legierungselemente Zinn, Zink, Phosphor, Magnesium und Eisen auf die Korngröße von Reinstkupfer zu untersuchen. Die Resultate zeigten, dass Phosphor zu einer Abnahme der Korngröße führt, währenddessen die Zunahme der Gehalte an Zinn, Zink, Magnesium und Eisen zu einem Anstieg der Korngröße führt. Es wird angenommen, dass die Korngröße über eine komplexe Wechselwirkung zwischen dem Wachstumsbehinderungsfaktor, und dessen Einfluss auf die konstitutionelle Unterkühlung und die Wachstumsbehinderung über die Beeinflussung der Wachstumsgeschwindigkeit und somit der latenten Wärmefreisetzung, und der Abkühlrate bestimmt wird. Des Weiteren wird angenommen, dass die Abkühlrate in großem Maße über die abnehmende Wärmeleitfähigkeit der columnaren Randschale und der Änderung der latenten Wärmemenge mit steigendem Legierungsgehalt bestimmt wird.

Index

Acronyms

at%	atomic percentage
bcc	base centered cubic structure
CCR	chair of casting research
CET	columnar-to-equiaxed transition
DAS	dendrite arm spacing
Eq.	equation
fcc	face centered cubic structure
Fig.	figure
GRF	growth restriction factor
hcp	hexagonal closed packed structure
mc	mixed crystal
MTL	Materials Technology Laboratory
NFZ	nucleation free zone
RED	Richardson-Ellingham-Diagram
SEM	scanning electron microscopy
TEM	transmission electron microscopy
wt%	weight percentage

List of nomenclature

a and b	constants for solutes	[-]
c_0	alloy concentration	[wt%]
Δc_0	concentration difference between the liquid and the solid	[wt%]
$c_{0,i}$	content for each solute in a multicomponent system	[wt%]
$\overrightarrow{c_0}$	multicomponent composition point vector	[wt%]
c_l	concentration of the liquid phase	[wt%]
c_s	concentration of the solid phase	[wt%]
$c^*_{l,i}$	liquid composition in a multicomponent system	[wt%]
$c^*_{s,i}$	solid composition in a multicomponent system	[wt%]
D	diffusion coefficient	[m^2/s]
d	particle diameter	[m]
f	volume fraction	[-]
$f(\theta)$	shape factor	[-]
fs	fraction solid	[-]
G	temperature gradient	[K/m]
ΔG_{cr}	activation barrier for nucleation	[J/mol]
$\Delta G_{cr,hom}$	activation barrier for homogeneous nucleation	[J/mol]
$\Delta G_{cr,het}$	activation barrier for homogeneous nucleation	[J/mol]
G_L^v	Gibbs free energy for the liquid phase per volume unit	[J/mol]
G_S^v	Gibbs free energy for the solid phase per volume unit	[J/mol]
ΔG_I	term of surface contribution to the work required to form a nucleus	[J/mol]
ΔG_V	term of volume contribution to the work required to form a nucleus	[J/mol]
$\Delta G(r)$	free energy change for building a cluster of radius r	[J/mol]
ΔG^v	change in the Gibbs free energy per volume unit	[J/mol]
ΔG^d	activation energy for the transfer of atoms from the liquid to the nuclei through the solid/liquid interface	[J/mol]
ΔH_m^v	change in enthalpy per volume unit	[J/mol]

I	*nucleation rate*	$[1/m^3s]$
I_0	*pre-exponential factor approximately equal to 1041*	$[1/m^3s]$
i and j	*solutes*	[-]
k	*partition coefficient*	[-]
k_B	*Boltzmann constant*	[J/K]
k_{c0}	*concentration of the solid phase*	[wt%]
$k_{bin,i}$	*partition coefficient for each solute*	[-]
k_i	*partition coefficient for each solute i,*	
	calculated at the multicomponent liquidus point (T_L, $\overrightarrow{c_0}$)	[-]
m	*slope of the liquidus line*	[K/wt%]
$m_{bin,i}$	*liquidus slope for each solute*	[K/wt%]
m_i	*slope of the liquidus surface in a multicomponent system*	[K/wt%]
n	*number of atoms*	[-]
$N(n)$	*total number of clusters*	[-]
N_0	*number of atoms in the liquid*	[-]
P	*supercooling parameter*	[K]
Q	*growth restriction factor*	[K]
Q_{fit}	*quadratic fit of the GRF*	[K]
$Q_{\sum bin}$	*overall GRF in a multicomponent system*	[K]
$Q_{bin,i}$	*individual GRF in a multicomponent system*	[K]
Q_{multi}	*GRF of a multicomponent system with n solutes*	[K]
r	*radius*	[m]
r_{cr}	*critical radius*	[m]
ΔS^v	*entropy of fusion per unit volume*	$[J/m^3K]$
T	*temperature*	[K]
ΔT	*undercooling, respectively total undercooling*	[K]
T_l	*local equilibrium liquidus temperature*	[K]
T_q	*local liquidus temperature*	[K]
ΔT_c	*constitutional undercooling*	[K]
ΔT_k	*kinetic undercooling*	[K]
ΔT_r	*undercooling due to the curvature of the tip*	[K]

ΔT_t	*thermal undercooling*	*[K]*
T_L	*liquidus surface*	*[K]*
ΔT_{fg}	*undercooling that is required to enable free growth*	*[K]*
T_m	*melting point*	*[K]*
V	*growth rate*	*[m/s]*
z	*distance of the interface*	*[m]*
α	*alpha mixed crystal*	*[-]*
γ	*interfacial energy*	*[J/m²]*
Θ	*wetting angle*	*[°]*
$\sigma_{S,L}$	*interfacial energy between the nucleus and the liquid phase*	*[J/m²]*
$\sigma_{S,n}$	*interfacial energy between the nucleus and the nucleant*	*[J/m²]*
$\sigma_{L,n}$	*interfacial energy between the nucleant and the liquid phase*	*[J/m²]*

1 Introduction

In alloy castings a fine and equiaxed grain structure is desirable [1], resulting in higher mechanical properties, a more uniform distribution of intermetallic phases and microporosity and therefore in an improved machinability, surface finish and resistance to hot tearing. The grain size is dependent on the cooling rate, the solute level of alloying elements and the total number of potent nucleants. As a result, a fine-grained microstructure can be obtained by either fast cooling, resulting in a higher degree of undercooling, or by increasing the number of potent nucleants, considering growth restriction. Grain refinement by inoculation involves the introduction of particles that can act as possible nucleants. The addition can be conducted either externally in the form of a fine powder or by chemical reactions, resulting in the formation of solid reaction products. Grain refinement by inoculation is widely used for aluminium alloys and several models have been developed to understand its mechanism [2,3,4]. For aluminium alloys, the most widely used inoculants are aluminium-titanium-boron master alloys. TiB_2 particles are present in the master alloy, remaining stable in the melt and act as nucleants for aluminium, whereas the aluminium matrix and the Al_3Ti particles dissolve into the melt, increasing the amount of solute titanium. Solute titanium is responsible for growth restriction of aluminium grains after they are nucleated [1].

Grain refinement in copper alloys is less popular as compared to other systems, especially as compared to aluminium alloys and even though there has been much practical work, the mechanism of grain refinement in copper alloys is still not well understood [5]. A complex mechanism is supposed for copper alloys, concerning a great influence of the alloy system, the range of the alloying elements, the impurities and the casting conditions on the grain size [6]. Therefore, the purpose of this work is to investigate the grain refinement mechanism in copper alloys. The literature review gives an overview of the fundamentals of grain refinement based on the several models that have been developed for aluminium alloys. Furthermore, an overview of the grain refinement of copper and copper alloys is given, with a focus on the copper-tin system. The first part of the work deals with the growth restriction factor of the alloying elements in copper alloys and its calculation by the use of binary alloy phase diagrams. In addition to the growth restriction factor, suitable compounds are examined with regard to their lattice disregistry to the copper lattice and their melting points. Based on the calculation of the growth restriction factors melting experiments were carried out to validate the influence of several alloying elements on the grain size of high purity copper.

2 Literature review

The following chapters deal with the fundamentals of nucleation processes referring to the classical homogeneous and heterogeneous nucleation theory and furthermore to the several models that have been developed for aluminium alloys to understand the grain refinement mechanism. An overview is given for the grain refinement of copper and copper alloys, with a focus on the copper-tin system.

2.1 Nucleation

Nucleation processes play a key role in the solidification of melts, taking influence on the morphology, grain size and the compositional homogeneity [2]. The fundamentals of homogeneous and heterogeneous nucleation are specified in the following chapters.

2.1.1 Homogeneous nucleation

Solidification requires an undercooling of the melt, changing the free energies of the phases and therefore their thermodynamic stability. As a first-order phase transition, solidification requires a short-range rearrangement of the atoms to form a crystal structure, in addition to an atomic movement over larger distances. Because of these atomic movements, there is always a necessity of leaving the equilibrium condition in order to initiate the solidification process. Phase transitions are driven by undercooling, creating crystalline regions at temperatures above the melting point. These crystalline regions or clusters are not stable and dissolve in the melt. [7,8].

At a given temperature, the phases with the lowest free energy are more stable. At a temperature below the melting point, the solid phase is more stable due to the lower free energy in comparison to the melt and vice versa at a temperature above the melting point. At a certain temperature, known as the melting point, the free energies of both the melt and the solid phase have to be equal and therefore the melt and the solid phase are in equilibrium condition [9], shown in **Fig. 2-1** [10].

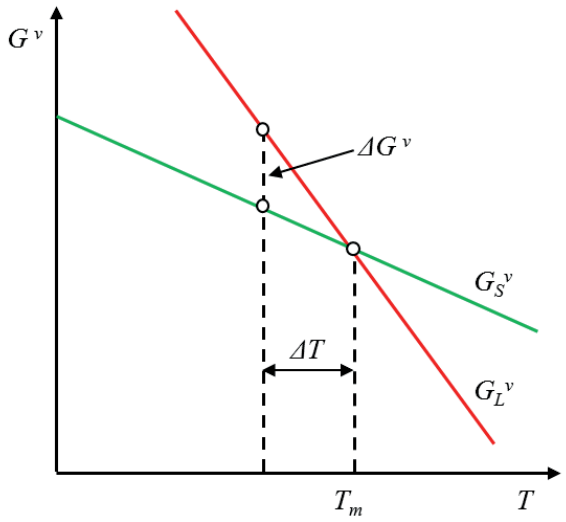

Fig. 2-1: Gibbs free energy of the liquid and the solid phase as a function of temperature after [10].

However, in full equilibrium condition, solidification is not possible. Only a departure from equilibrium will enable solidification processes, bringing the melt into an undercooled metastable condition. The driving force for the phase transition from liquid to solid can be expressed by equation (Eq.) (**2-1**) [7,9]:

$$\Delta G^v = {G_L}^v - {G_S}^v \tag{2-1}$$

where ΔG^v is the change in the Gibbs free energy per volume unit, ${G_L}^v$ and ${G_S}^v$ are the Gibbs free energies for the liquid and the solid phase per volume unit. The direct relationship between ΔG^v and the undercooling is given by Eq. (**2-2**) [2]:

$$\Delta G^v(T) = \frac{{\Delta H_m}^v \Delta T}{T_m} \tag{2-2}$$

where ${\Delta H_m}^v$ is the change in enthalpy, ΔT is the undercooling and T_m is the melting point. Due to the fact that first of all a cluster has to be formed as a result of random fluctuations, the solid condition is not always spontaneously in an undercooled melt. Above the melting point a cluster is potentially unstable. Below the melting point, the stability of a cluster depends on its size. At small cluster sizes the interfacial energy due to the curvature is the main contribution to the activation barrier for solid nucleation. As a result, small clusters tend to dissolve in the melt [2,7,8,9].

In the case of homogeneous nucleation, where nucleation occurs within the melt without the help of impurities or other surface sites, the work of formation of a spherical nucleus with its radius r can be expressed in terms of a surface and a volume contribution to the work, required to form a nucleus. The obtained volume energy can be expressed by Eq. (**2-3**) [7,9]:

$$\Delta G_V = -\frac{4}{3}\pi r^3 \Delta G^v \tag{2-3}$$

where ΔG_V is the term of volume contribution. The term of the surface contribution, which has to be expended, can be given by Eq. (**2-4**) [2,7,9]:

$$\Delta G_I = 4\pi r^2 \gamma \tag{2-4}$$

where ΔG_I is the contribution of the surface on the free energy change to form a cluster and γ is the interfacial energy. The free energy change for building a cluster of radius r is expressed by Eq. (**2-5**) [2,7,9]:

$$\Delta G(r) = -\frac{4}{3}\pi r^3 \Delta G^v + 4\pi r^2 \gamma \tag{2-5}$$

where $\Delta G(r)$ is the free energy change for building a cluster of radius r. Volume and surface energy contribution have opposite signs. The formation of surface results in a decrease of the thermodynamic stability of the cluster, the formation of volume in an increase of the thermodynamic stability. At a temperature above the melting point $\Delta G^v \leq 0$ and therefore $\Delta G(r)$ is always positive. As a result, a nucleus dissolves by a gain of energy. At a temperature below the melting point, $\Delta G(r)$ decreases after reaching the activation barrier for nucleation ΔG_{cr} at a critical size r_{cr}. The calculation of r_{cr} is shown in Eq. (**2-6**) to (**2-9**) [2,9]:

$$\frac{d\Delta G(r)}{dr} = 0 \tag{2-6}$$

$$-4\pi r^2 \Delta G^v + 8\pi r\gamma = 0 \tag{2-7}$$

$$r_{cr} = \frac{2\gamma}{\Delta G^v} \tag{2-8}$$

$$\Delta G_{cr,hom} = \frac{16}{3}\pi \frac{\gamma^3}{(\Delta G^v)^2} \tag{2-9}$$

where $\Delta G_{cr,hom}$ is the activation barrier for homogeneous nucleation. The free energy change for cluster formation as a function of the cluster size is shown in **Fig. 2-2**. At increasing values of undercooling, r_{cr} is reduced.

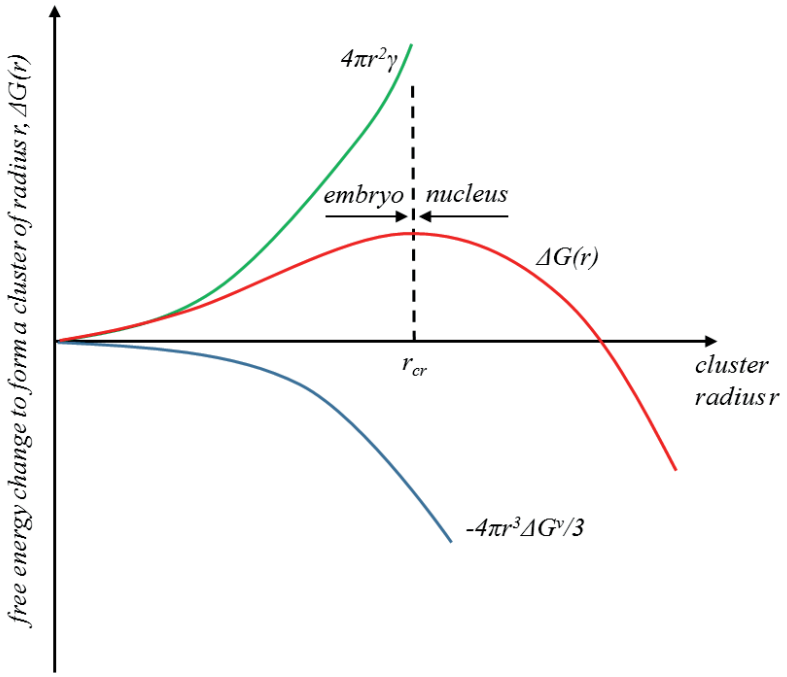

Fig. 2-2: Free energy change for cluster formation as a function of cluster size for homogeneous nucleation after [2].

2.1.2 Heterogeneous nucleation

As an intrinsic process, homogeneous nucleation is only dependent on the properties of the melt. Because of a large activation barrier for nucleation, the likelihood for homogenous nucleation is low and large undercooling values are required to overcome this barrier. An undercooling of only a few degrees, as it is common in most castings, is not sufficient to enable homogeneous nucleation. To promote solidification, crucible walls, impurity inclusions, particles can act as substrates by lowering the activation barrier for nucleation. This phenomenon is known as heterogeneous nucleation, schematically shown in **Fig. 2-3** [2,7].

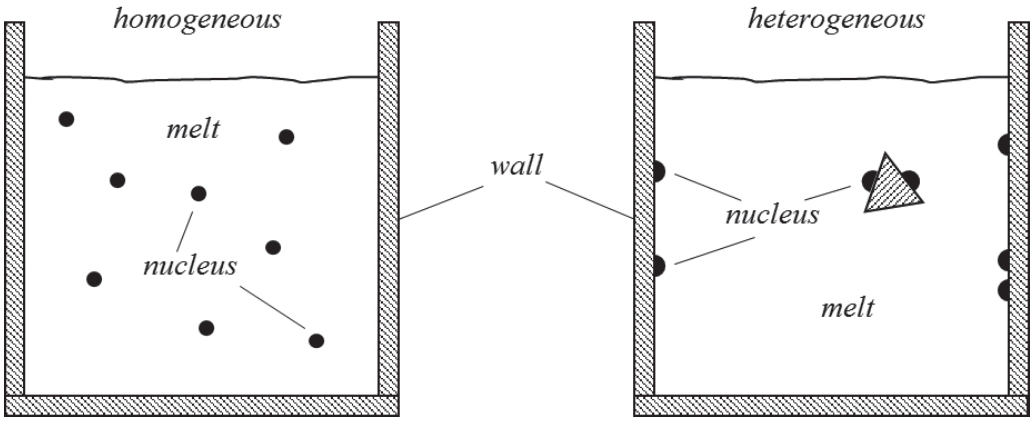

Fig. 2-3: Schematic representation of homogenous and heterogeneous nucleation after [9].

For the solidification of a melt, only a single nucleation event is required. Due to the fact that the nucleant particle concentration is of the order of about 10^{12} [m^{-3}], even in high-purity melts, the likelihood of finding a nucleus, standing in contact with the liquid, is great. The nucleation of a nucleus on a substrate, that has a sufficient crystallographic structure and chemistry, is schematically shown in **Fig. 2-4**. In addition to the interfacial energy between the nucleus and the liquid phase $\sigma_{S,L}$, the interfacial energy between the nucleus and the nucleant $\sigma_{S,n}$ and the interfacial energy between the nucleant and the liquid phase $\sigma_{L,n}$ have to be considered. The wetting angle θ can be expressed by Eq. (**2-10**) [2,7,9]:

$$\cos(\theta) = \frac{\sigma_{L,n} - \sigma_{S,n}}{\sigma_{S,L}} \tag{2-10}$$

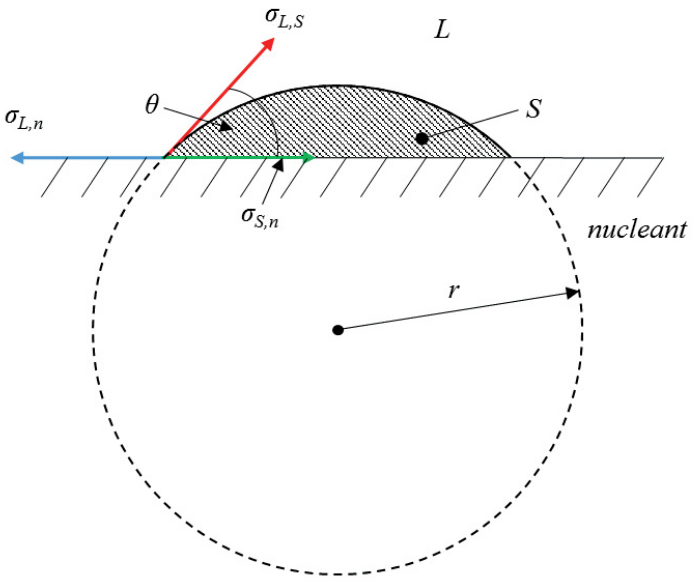

Fig. 2-4: Schematic illustration of heterogeneous nucleation on a nucleant after [2].

The consideration of the interface between the nucleus and the nucleant leads to the activation barrier for homogeneous nucleation $\Delta G_{cr,het}$ (expressed by Eq. (**2-11**)), which is the nucleation barrier for homogeneous nucleation, modified by the shape factor $f(\theta)$, given by Eq. (**2-12**) [2,7,9]:

$$\Delta G_{cr,het} = \frac{16}{3}\pi \frac{\gamma^3}{(\Delta G^v)^2} f(\theta) \tag{2-11}$$

$$f(\theta) = \frac{1}{4}(2 + \cos(\theta))(1 - \cos(\theta))^2 \tag{2-12}$$

The value of the shape factor varies from 0, signifies complete wetting (θ = 0°), to 1, signifies no wetting (θ = 180°). The variation of the shape factor, the ratio of $\Delta G_{cr,het}/\Delta G_{cr,hom}$, and the spherical cap size as a function of θ are shown in **Fig. 2-5** [2,7,9].

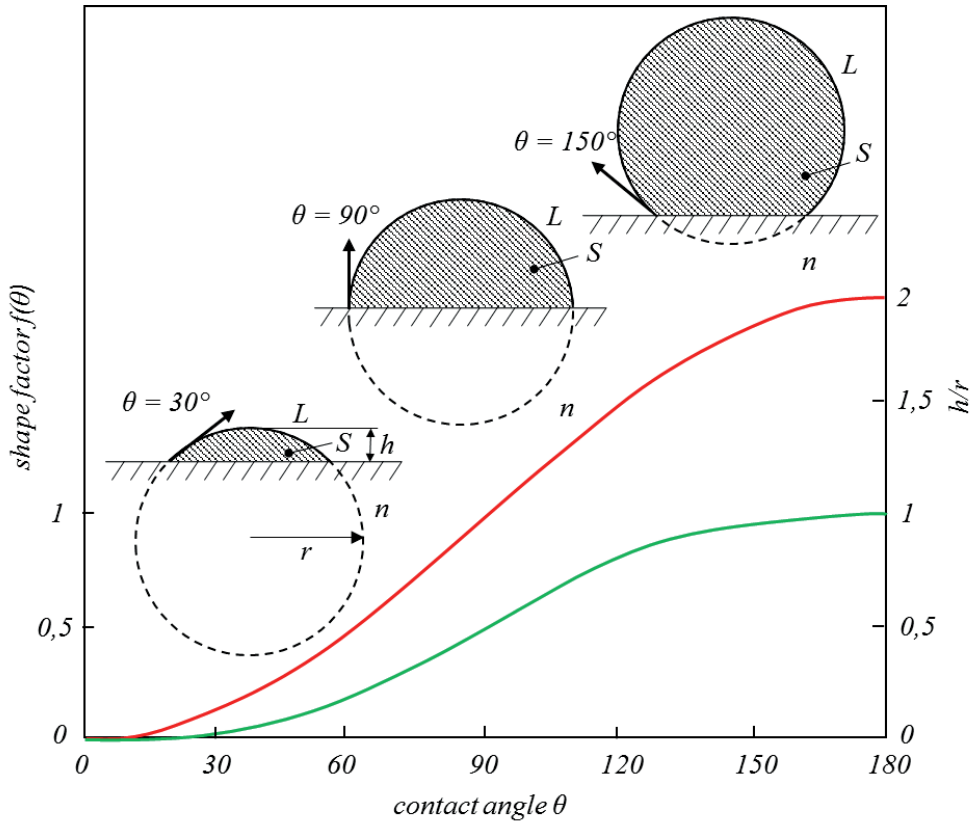

Fig. 2-5: The variation of the shape factor $f(\theta)$ and the spherical cap size h/r, as function of the contact angle θ after [2].

2.1.3 Nucleation rate

The kinetic of the phase transition is driven by the nucleation rate of nuclei with critical size. Based on the equilibrium distribution of an ensemble of crystalline clusters, the nucleation rate, the number of grains nucleated within a certain melt volume and time, can be expressed. The distribution of crystalline clusters $N(n)$, which contain n atoms, is related to the total number of atoms in the liquid N_0 , the temperature T and Gibbs free energy $\Delta G(r)$ for building a cluster with radius r and is given by Eq. (**2-13**) [7,8]:

$$N(n) = N_0 e^{-\left(\frac{\Delta G(r)}{k_B * T}\right)} \tag{2-13}$$

where k_B is the Boltzmann constant. The number of crystal clusters increases with decreasing activation barrier to form a cluster and has its minimum at $r = r_{cr}$, due to the maximum of the work, required to form a cluster, shown in **Fig. 2-6**.

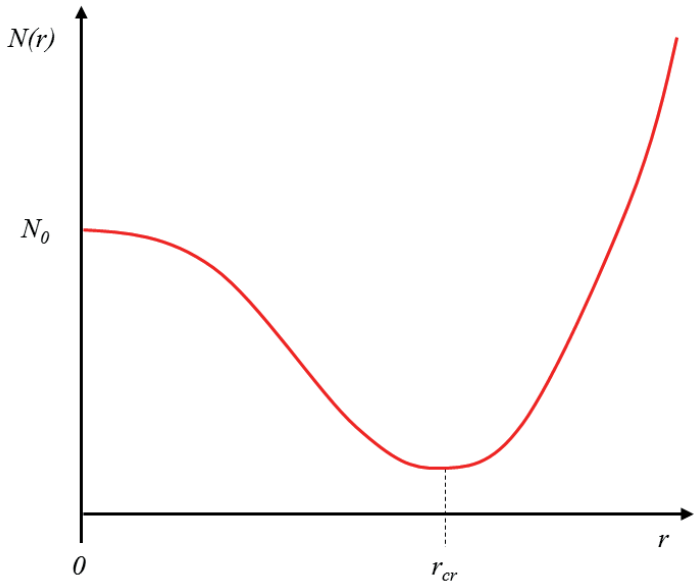

Fig. 2-6: Schematic illustration of the number of clusters as a function of the radius r with its minimum at r_{cr} after [7].

In addition to the cluster formation with critical size, the transfer of atoms from the liquid to the nuclei through the solid/liquid interface has to be considered by an activation energy ΔG_d and therefore the nucleation rate can be given by Eq. (**2-14**) [7,8]:

$$I = I_0 e^{-\left(\frac{\Delta G_{cr,het}+\Delta G_d}{k_B T}\right)} \tag{2-14}$$

where I_0 is a pre-exponential factor approximately equal to 10^{41} [m^{-3} s^{-1}] [8]. The nucleation rate is therefore dependent on the rate of atom transport to the nuclei and the rate of cluster formation with critical size, which is dependent on the total number of crystalline clusters $N(n)$. Due to the high activation barrier at low undercooling, the nucleation rate is low. With increasing undercooling the nucleation rate increases up to a maximum before decreasing again due a diffusion limitation at low temperatures, shown in **Fig. 2-7**.

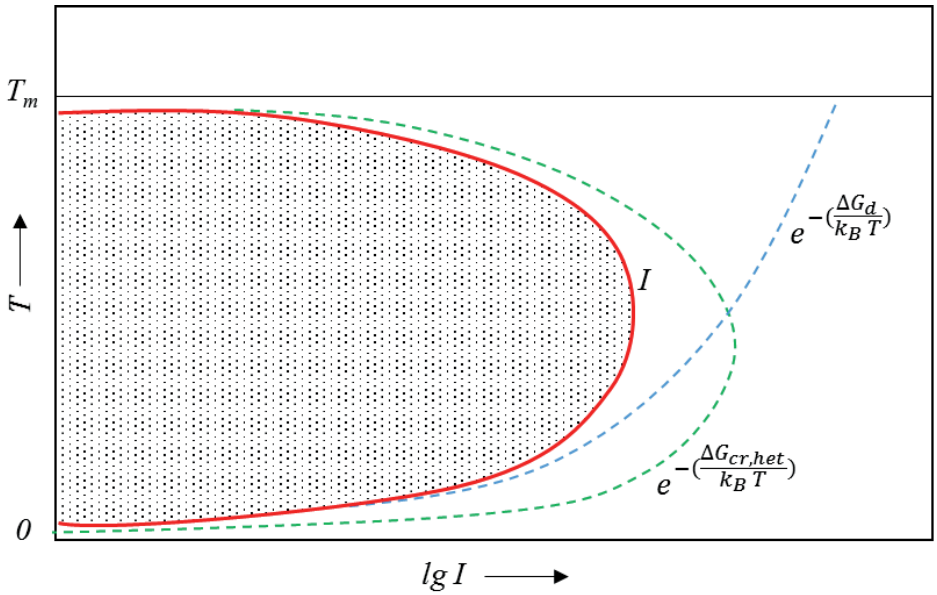

Fig. 2-7: Nucleation rate as a function of temperature after [8].

2.2 Mechanisms of grain refinement

As already mentioned in chapter **1**, a fine equiaxed grain structure leads to higher mechanical properties, a more uniform distribution of intermetallic phases and microporosity and therefore resulting in an improved machinability, surface finish and resistance to hot tearing. The grain size is dependent on the cooling rate, the solute level of alloying elements and the total number of potent nucleants. As a result, a fine-grained microstructure can be obtained by either fast cooling, resulting in a higher degree of undercooling, or by increasing the number of potent nucleants, considering growth restriction. Several models that have been developed to understand the complex mechanism of grain refinement, can be classified into two groups, known as nucleant paradigm and solute paradigm and are specified in the following chapters, based on the knowledge for aluminium alloys. The basic mechanisms of grain refinement in other alloy systems follow the understanding that applies for aluminium alloys [2,3,4].

2.2.1 Nucleant paradigm

The nucleant paradigm describes the heterogeneous nucleation of solid aluminium on potent nucleation sites and can be classified into five theories [3]:

- carbide/boride theory
- phase diagram/peritectic theory
- peritectic hulk theory
- hypernucleation theory
- duplex nucleation theory

2.2.1.1 Requirements of potent nucleating sites

Heterogeneous nucleation of solid aluminium on nucleants is determined by the equilibrium of interfacial energies between the nucleus and the liquid phase $\sigma_{S,L}$, between the nucleus and the nucleant $\sigma_{S,n}$ and between the nucleant and the liquid phase $\sigma_{L,n}$. The equilibrium can be expressed according to Eq. (**2-10**) by Eq. (**2-15**) [3]:

$$\sigma_{L,n} = \sigma_{S,L} + \sigma_{S,n}\cos(\theta) \tag{2-15}$$

any particle that should act as a potent nucleating site, should wet the nucleation solid. That can be achieved by a contact angle that is as low as possible and therefore $\sigma_{S,L}$ and/or $\sigma_{S,n}$ should be low and $\sigma_{L,n}$ should be high. A low $\sigma_{S,n}$ can be achieved by a low lattice disregistry, whereas $\sigma_{S,L}$ and $\sigma_{L,n}$ can be influenced by the alloying elements. A low contact angle leads to a small thermodynamic activation barrier even at low undercooling. At a contact angle below 10° the classical spherical cap model breaks down due to a spherical cap, which is below the thickness of a mono-layer. Hence, more potent particles can act as nucleating sites due to the adsorption of a mono-layer of solid on the nucleant, which was proposed by Kim and Cantor [11,12]. In addition to a low misfit in the lattice dimensions, a potent nucleating site should match following requirements [3]:

- the melting point should be higher than that of the alloy
- it should initiate freezing at a very small undercooling
- the nucleating particles should be uniformly distributed
- the nucleating particles should be larger than the critical size, which is dependent on the undercooling of the melt

2.2.1.2 Carbide/boride theory

It is suggested that compounds such as AlB_2, TiB_2 and TiC are responsible for the nucleation of aluminium, due to the epitaxy between planes of compounds and aluminium. Although Al_3Ti possesses a greater number of planes with a good lattice match with aluminium in comparison to AlB_2, TiB_2 and TiC, Al_3Ti particles are expected to dissolve rapidly in the melt at low concentrations. Possible orientation relationships between aluminium and AlB_2, TiB_2, TiC and Al_3Ti are shown in **Fig. 2-8** [2,3,13].

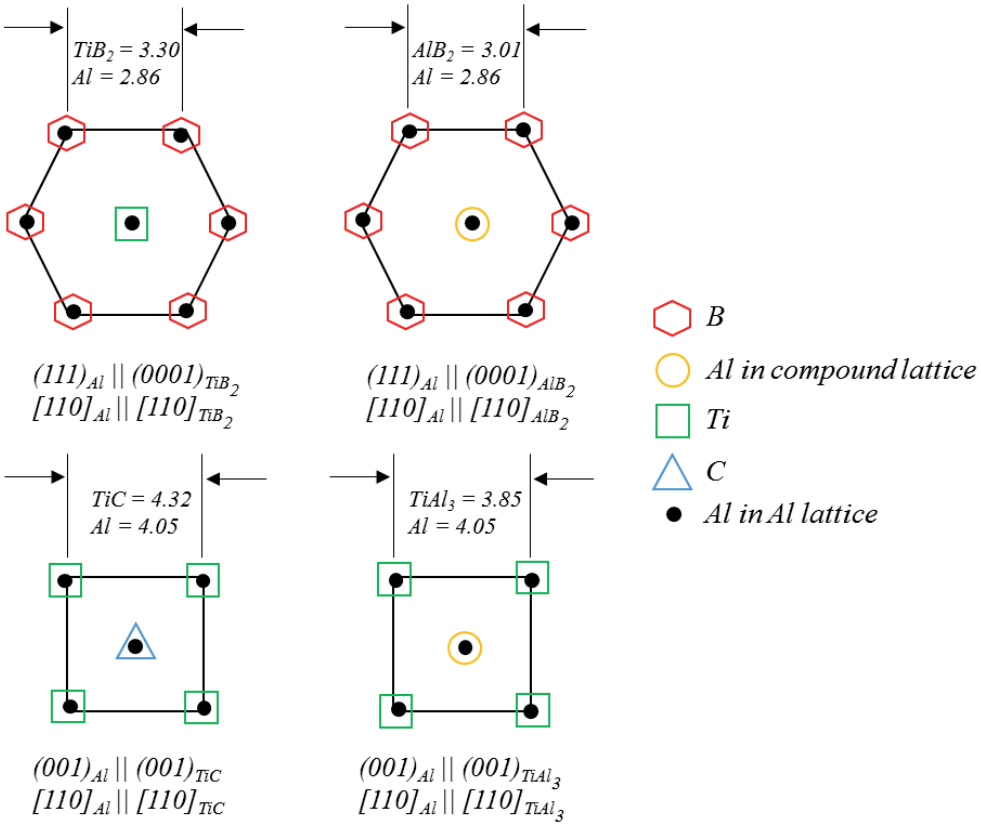

Fig. 2-8: Lattice match of Al with TiB_2, AlB_2, TiC and $TiAl_3$ after [3].

2.2.1.2.1 Orientation relationship between the copper lattice and the crystallographic structure of compounds

Related crystallographic planes of the face-centered cubic structure (fcc) and the body-centered cubic structure (bcc) are shown in **Fig. 2-9** and are given by [2,3,14,15]:

$$\{111\}_{MeX} \,||\, \{111\}_{Cu} \quad \langle 110\rangle_{MeX} \,||\, \langle 110\rangle_{Cu} \quad \text{or} \quad \{110\}_{MeX} \,||\, \{110\}_{Cu} \quad \langle 111\rangle_{MeX} \,||\, \langle 111\rangle_{Cu}$$

furthermore, the crystallographic relationship of the cubic structure can be expressed by [2,3,14]:

$$\{001\}_{MeX} \,||\, \{001\}_{Cu}$$
$$\langle 110\rangle_{MeX} || \langle 110\rangle_{Cu}$$

representing the basal planes, respectively the side planes of the cubic structure.

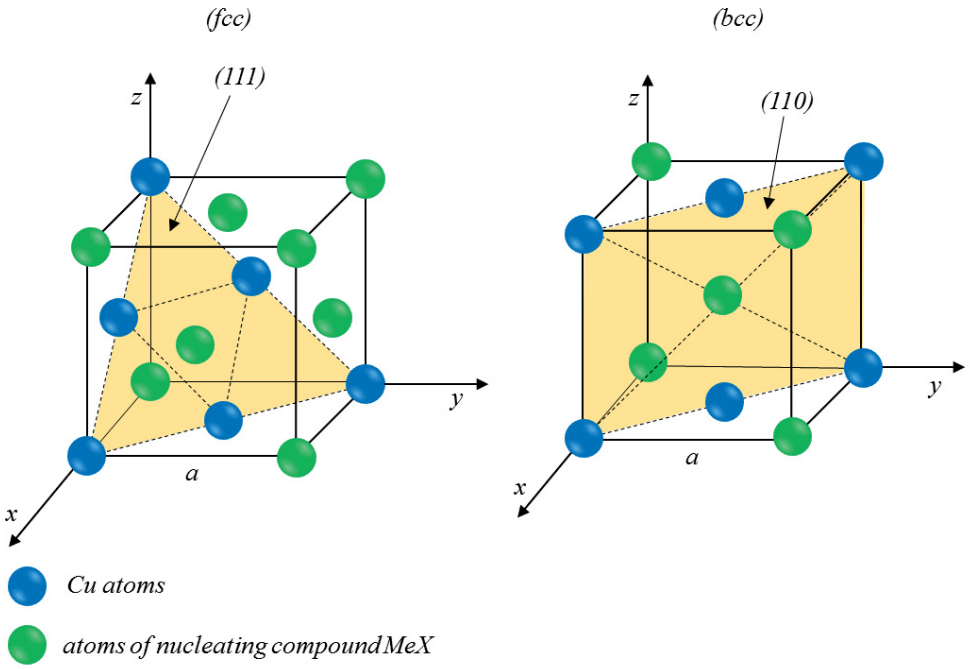

Fig. 2-9: Related crystallographic planes of the fcc structure and the bcc structure, adapted from [14,15].

Orientation relationships between the copper lattice and compounds of the tetragonal, respectively the orthorhombic type are shown in **Fig. 2-10**. Related crystallographic planes can be given by [15]:

$$\{001\}_{MeX} \,||\, \{001\}_{Cu}$$
$$\langle 110\rangle_{MeX} || \langle 110\rangle_{Cu}$$

representing the basal planes of the tetragonal structure, respectively the side planes in dependence on the c/a ratio and furthermore the basal planes and side planes of the orthorhombic structure in dependence on the a/b ratio, respectively the a/c and b/c ratio.

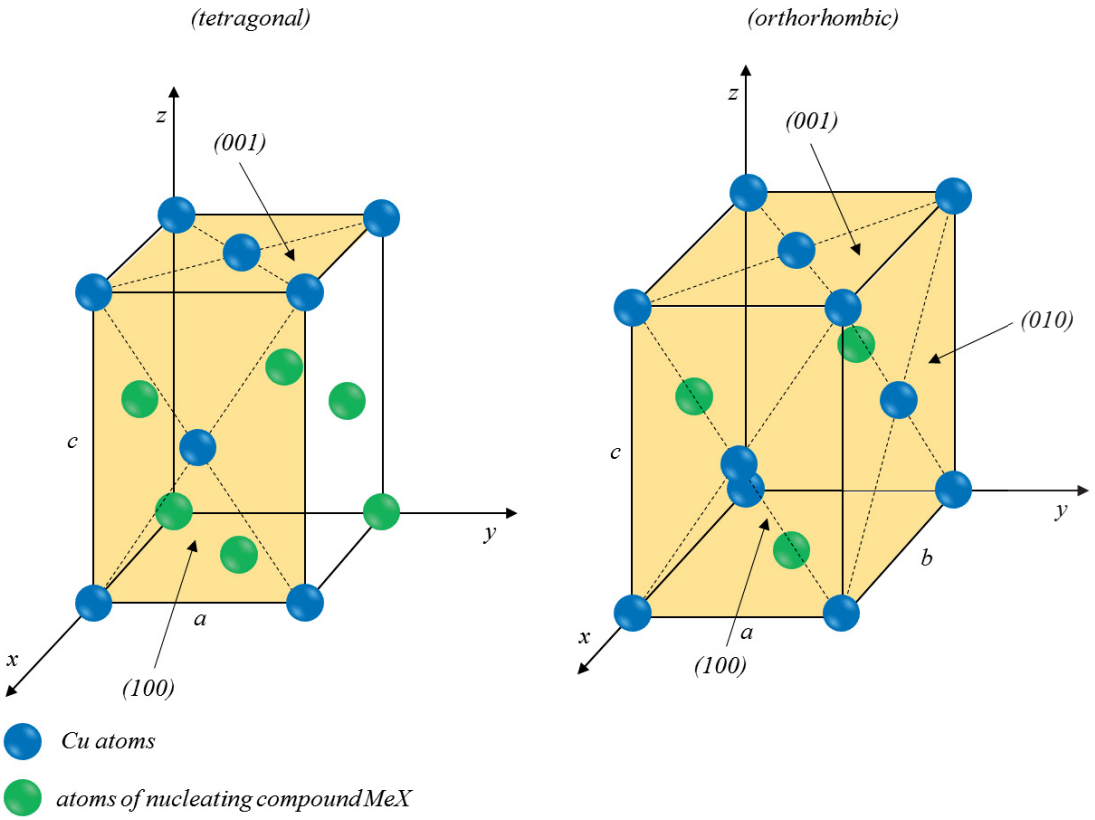

Fig. 2-10: Related crystallographic planes of the copper lattice with the tetragonal structure and the orthorhombic structure, adapted from [14,15].

Fig. 2-11 and **Fig. 2-12** show possible lattice matching of the copper lattice with the hexagonal closed packed structure (hcp). Both the hcp structure and the fcc structure are close packed structures. The {111} plane of the fcc structure shows similar atom distribution with the {0001} plane of the hcp structure, differing in the stacking order. The orientation relationship can be given by [14,15]:

$$\{0001\}_{MeX} \| \{111\}_{Cu}$$
$$\langle 11\bar{2}0\rangle_{MeX} \| \langle 110\rangle_{Cu}$$

furthermore, the orientation relationship between the side planes, respectively the basal planes of the copper lattice and the side planes of the hcp structure can be given by:

$$\{10\bar{1}0\}_{MeX} \| \{001\}_{Cu}$$
$$\langle 11\bar{2}0\rangle_{MeX} \| \langle 110\rangle_{Cu}$$

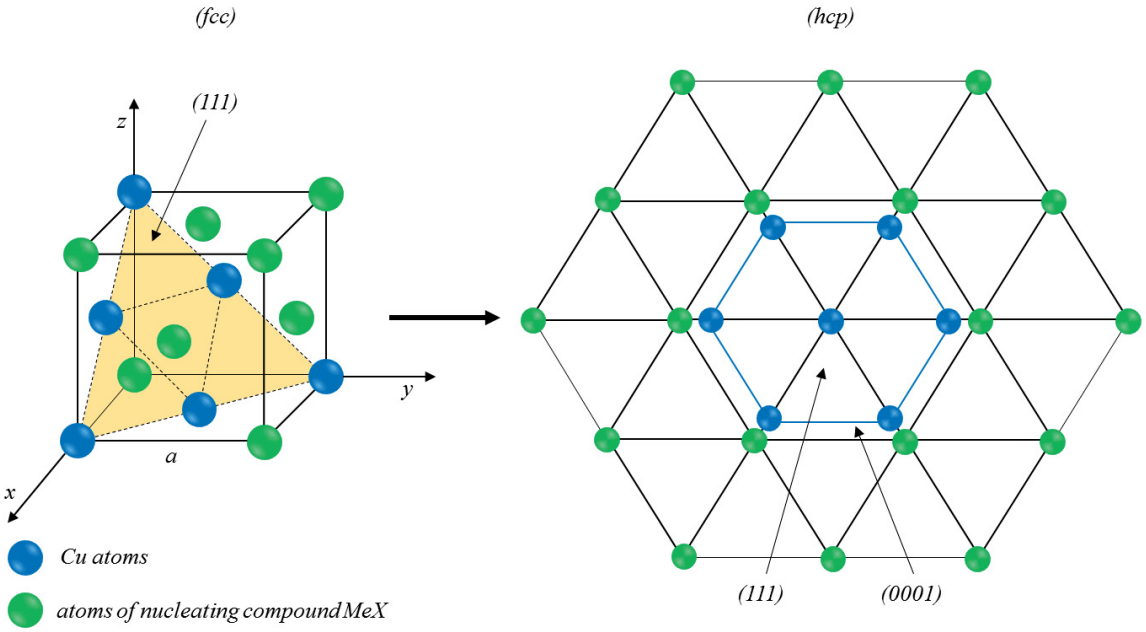

Fig. 2-11: Orientation relationship of the {111} crystallographic planes of the fcc structure with the {0001} planes of the hcp structure, adapted from [15].

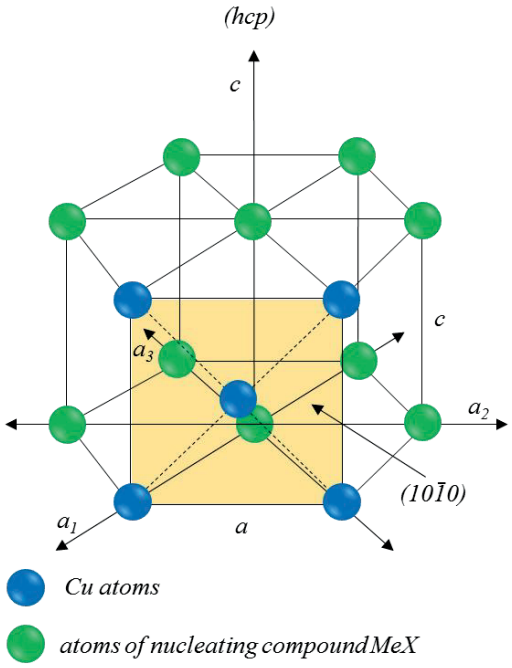

Fig. 2-12: Orientation relationship of the {001} crystallographic planes of the fcc structure with the $\{10\bar{1}0\}$ planes of the hcp structure, adapted from [15].

2.2.1.3 Phase diagram/peritectic theory

The peritectic theory co-existed with the carbide/boride theory for many years. Due to a smaller disregistry between Al_3Ti and aluminium and the potential of a peritectic transformation, it was suggested that Al_3Ti is more potent in comparison to AlB_2, TiB_2 and TiC and therefore requires less undercooling to become active. However, Al_3Ti is expected to dissolve rapidly in the melt, equivalent to a less thermodynamic stability in hypoperitectic melts with a titanium level below 0,15 wt%. The aluminium-rich end of the aluminium-titanium phase diagram is shown in **Fig. 2-13** [3,13].

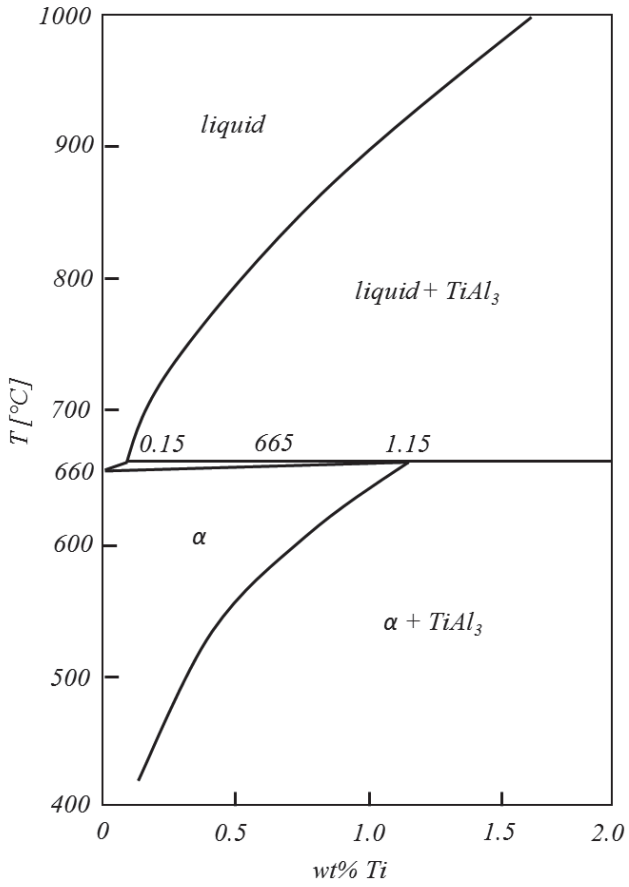

Fig. 2-13: Phase diagram of Al rich end of the Al-Ti system after [13].

It is suggested that Al_3Ti is able to nucleate aluminium by the peritectic reaction that is given by Eq. (**2-16**) [3]:

$$liquid + Al_3Ti \rightarrow \alpha - Al \tag{2-16}$$

according to **Fig. 2-13** the peritectic reaction can only occur at titanium levels of above 0,15 wt%. The amount of titanium, added in the form of Al-Ti master alloys during conventional direct chill casting of aluminium, is about 0,01 wt%, which is much lower than 0,15 wt%, required for the peritectic reaction, which is the main problem of the peritectic theory. Furthermore, it is supposed that the addition of boron in Al-Ti master alloys might shift the peritectic composition to a lower level of the titanium content [3].

2.2.1.4 Duplex nucleation theory

According to the duplex nucleation theory, it is shown that TiB_2 does not act as a nucleating site on its own and is pushed to the grain boundaries in the absence of excess titanium. At hyperperitectic concentrations of titanium, TiB_2 particles were found in the centre of aluminium grains, coated by an Al_3Ti layer. The same layer was found as well at hypoperitectic concentrations of titanium [3].

A melt spinning technique was developed by Schumacher and Greer [16], to quench an aluminium-based alloy ($Al_{85}Y_8Ni_5Co_2$ – contents in atomic percentage (at%)) soon after the nucleation of α-Al, achieving high cooling rates of ~10^6 [K/s]. Transmission electron microscopy analysis (TEM) showed TiB_2 particles that were surrounded by an Al_3Ti layer with a thickness of about 3 [nm] on which the aluminium could nucleate. It was found that 0,01 wt% excess titanium was sufficient for the formation of the Al_3Ti layer. Furthermore, it was found that no nucleation of aluminium occurred on other planes than on the {0001} TiB_2 plane. The most common orientation relationship that was found between the three phases can be given by [13]:

$$\{0001\}_{TiB_2} || \{112\}_{Al_3Ti} || \{111\}_{Al}$$
$$\langle 11\bar{2}0\rangle_{TiB_2} || \langle 201\rangle_{Al_3Ti} || \langle 110\rangle_{Al}$$

representing the close-packed directions within the close-packed planes, on which the lattice mismatch is small. The steps of nucleation-growth of aluminium on a TiB_2 particle is schematically shown in **Fig. 2-14** [14].

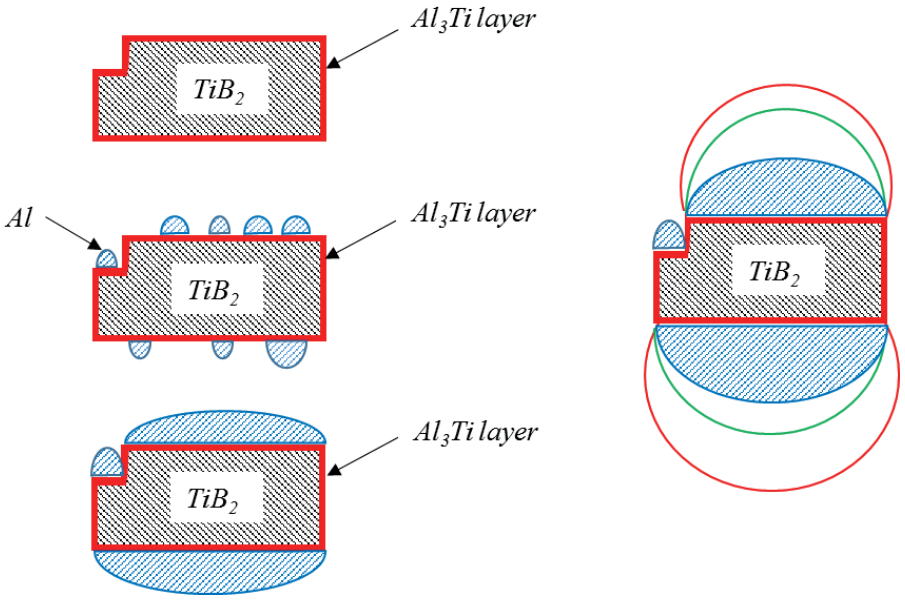

Fig. 2-14: Schematic illustration of the growth of aluminium on an Al_3Ti layered TiB_2 according to the free-growth model after [14].

2.2.2 Solute paradigm

As already mentioned in **2.2**, grain refinement of alloys is influenced by the total number of potent particles, the solute level of the alloying elements and the cooling rate, resulting in a higher degree of undercooling. The solute paradigm proves that efficient grain refinement is not only achieved by inoculation, but also by the influence of segregating solutes [3,4].

Within a grain refined casting there can be two mechanisms of grain initiation [12,16]: on the one hand grain initiation occurs on the wall of the casting as a result of thermal undercooling, on the other hand in the bulk of the melt due to constitutional undercooling. The constitutionally undercooled zone, which is build up by solutes, shows a significant influence on nucleation. In addition to the influence of solutes on the formation of the constitutionally undercooled zone, segregation solutes influence grain refinement by growth restriction, which is measured in terms of a growth restriction factor Q (GRF). The combination of the nucleant paradigm and the solute paradigm results in the “free growth model”, which was first proposed by Bunn et al. [17]. The following chapters deal with the fundamentals of the constitutional undercooling and the growth restriction factor related to the “free growth model”.

2.2.2.1 Constitutional undercooling

In a pure metal, the stability of the solid/liquid interface is dependent on the direction of the heat flux, respectively the temperature gradient. In the case that the melt is cast into a cold mold, solidification will start at the mold. As a result, there will be a heat flux from the hot melt to the mould, in the opposite direction to the growth direction of the planar solid/liquid interface. As the melt is the hottest part, the liquid temperature always increases ahead of the interface and therefore the temperature gradient is positive. When a perturbation is formed, the temperature gradient in the liquid increases, while the temperature gradient in the solid decreases and therefore more heat flows into the tip of the perturbation and melts back. For this reason, the planar interface is stabilised. The opposite is found during equiaxed solidification. The random growth of a free crystal in an undercooled melt leads to a heat flux from the crystal down the negative temperature gradient to the undercooled melt. When a perturbation is formed, the slope of the negative temperature gradient increases and more latent heat is rejected by the perturbation, resulting in a more unstable solid/liquid interface [18,19].

In the case of an alloy, not only the heat flow effects have to be considered, but also the influence of solute diffusion. During the solidification of an alloy, a lower solubility of the solid leads to a solute build-up in front of a planar solid/liquid interface, resulting in a boundary layer. As the composition of the solid is equal to the composition of the alloy far ahead of the interface, the exponentially decrease of the solute concentration within the boundary layer can be given by Eq. (**2-17**) [18]:

$$c_l = c_0 + \Delta c_0 e^{-(\frac{V}{D}z)} \tag{2-17}$$

where c_l is the liquid concentration within the boundary layer, c_0 is the concentration of the solid, equal to that of the liquid far ahead of the interface, Δc_0 is the concentration difference, V is the growth rate, z is the distance of the interface and D is the diffusion coefficient. The change of the solute concentration takes influence on the local equilibrium temperature T_l. The difference in temperature ΔT between the local equilibrium temperature and the liquidus temperature corresponding to the initial alloy composition can be expressed by Eq. (**2-18**) [18]:

$$\Delta T = T_l(c_0) - T_l = m(c_0 - c_l) \tag{2-18}$$

where m is the slope of the liquidus line. The relationship between the phase diagram, the diffusion boundary layer and the temperature is shown in **Fig. 2-15**. As c_l decreases with distance of the interface, T_l increases. Each volume element of the liquid, dependent on its distance of the solid/liquid interface, possesses its temperature T_q. If the gradient of T_q is less than the gradient of T_l, the volume element of liquid is constitutionally undercooled. The existence of a constitutionally undercooled zone ahead of the solid/liquid interface during the solidification of an alloy is dependent on the temperature gradient G. The limiting condition for the occurrence of an undercooled zone is given by Eq. (**2-19**) [18]:

$$G = \left(\frac{dT_q}{dz}\right)_{z=0} \tag{2-19}$$

according to Eq. (**2-20**), the interface is constitutionally undercooled when [18]:

$$\frac{G}{V} < -m\frac{\Delta c_0}{D} \tag{2-20}$$

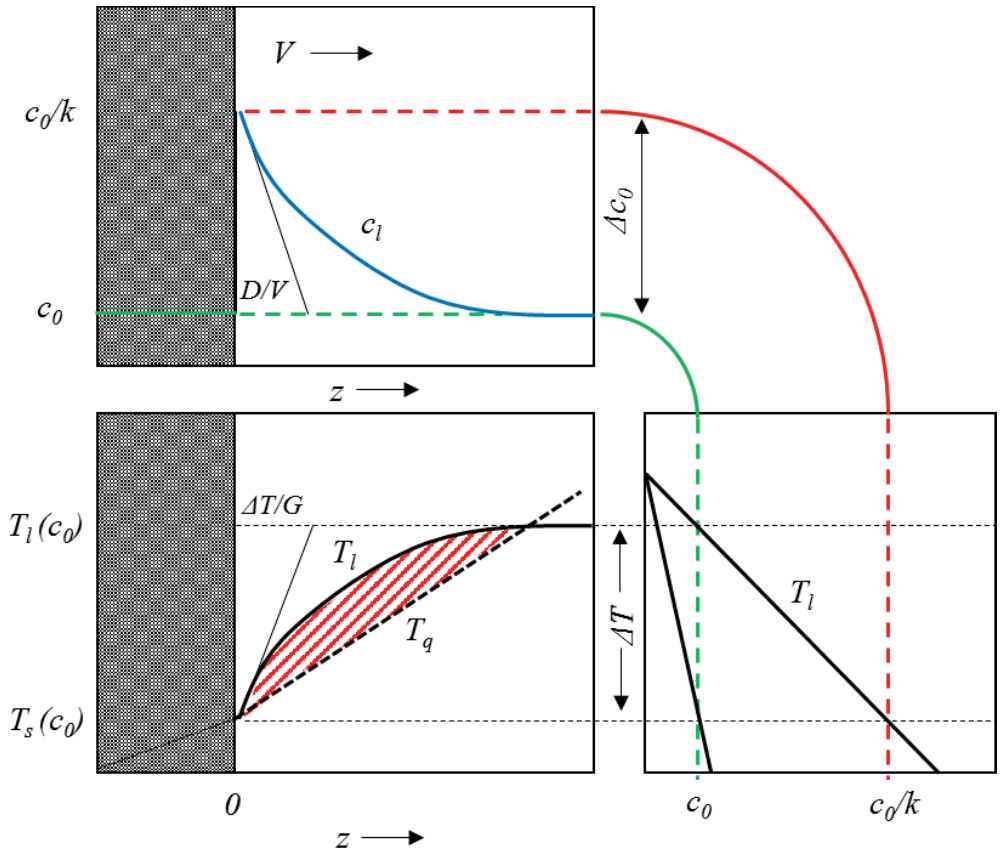

Fig. 2-15: Constitutional undercooling in alloys after [18].

The difference between the growth of an equiaxed dendrite in a pure metal and in an alloy is shown in **Fig. 2-16**. In a pure metal, the growth of a dendrite only occurs under heat extraction from the interface of the dendrite to the surrounding liquid. As a result, the temperature gradient is negative and only a thermal undercooling (ΔT_t) exists. During the equiaxed alloy growth, a solute build-up ahead of the dendritic tip results in a solute undercooling, respectively a constitutional undercooling and therefore the total undercooling ΔT is the sum of the thermal undercooling (ΔT_t) and the constitutional undercooling (ΔT_c). After adding the undercooling due to the curvature of the tip (ΔT_r) and the kinetic undercooling (ΔT_k), the total undercooling can be given by Eq. (**2-21**) [18,20,21]:

$$\Delta T = \Delta T_c + \Delta T_t + \Delta T_r + \Delta T_k \tag{2-21}$$

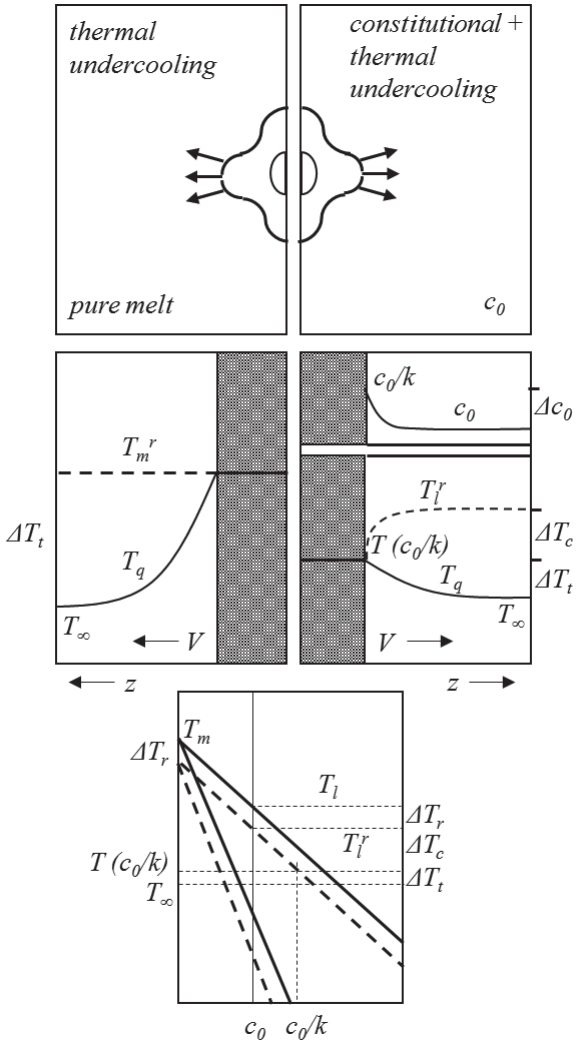

Fig. 2-16: Growth of an equiaxed dendrite in a pure metal and in an alloy after [20].

2.2.2.2 Growth restriction factor

For initiating grain growth, there is a necessity of small undercoolings that allow nucleants to become active. In an alloy, the presence of solute elements leads to a constitutionally undercooled zone at the solid/liquid interface, as mentioned in **2.2.2.1**. To quantify the generation of the constitutional undercooling, respectively the effect of solute elements on the grain size, two parameters have been used, expressed by Eq. (**2-22**) and Eq. (**2-23**) [12,21]:

$$P = \frac{mc_0(k-1)}{k} \tag{2-22}$$

$$Q = mc_0(k-1) \tag{2-23}$$

where P is the supercooling parameter, m is the liquidus slope, k is the partition coefficient and c_0 is the solute content in the alloy. The degree of undercooling ahead of a planar interface induced by growth restriction is reflected by the supercooling parameter P. The use of P, to quantify the effect of constitutional undercooling on the grain size, is limited by the fact that P is equal to the freezing range of the alloys, assuming that the liquidus and solidus lines are straight [22]. To specify the correlation between grain size and undercooling Q is used for dendrite solidification.

2.2.2.2.1 Definition of Q

In the case of solidification under non-equilibrium conditions, respectively Scheil conditions, it is assumed that there is zero diffusion in the solid and unlimited diffusion in the liquid. Under the circumstances that a bar is solidifying from a melt of concentration c_0 and a partition coefficient k, the concentration of the solid, given by kc_0, increases as solute is partitioned into the liquid due to the formation of new solid phase from a more concentrated liquid, as shown in **Fig. 2-17**. The advance of the interface by a small fraction df leads to the conditions to derive Scheil equation to describe the composition of the solid and the liquid during solidification, which is expressed by Eq. (**2-24**) to Eq. (**2-28**) [23]:

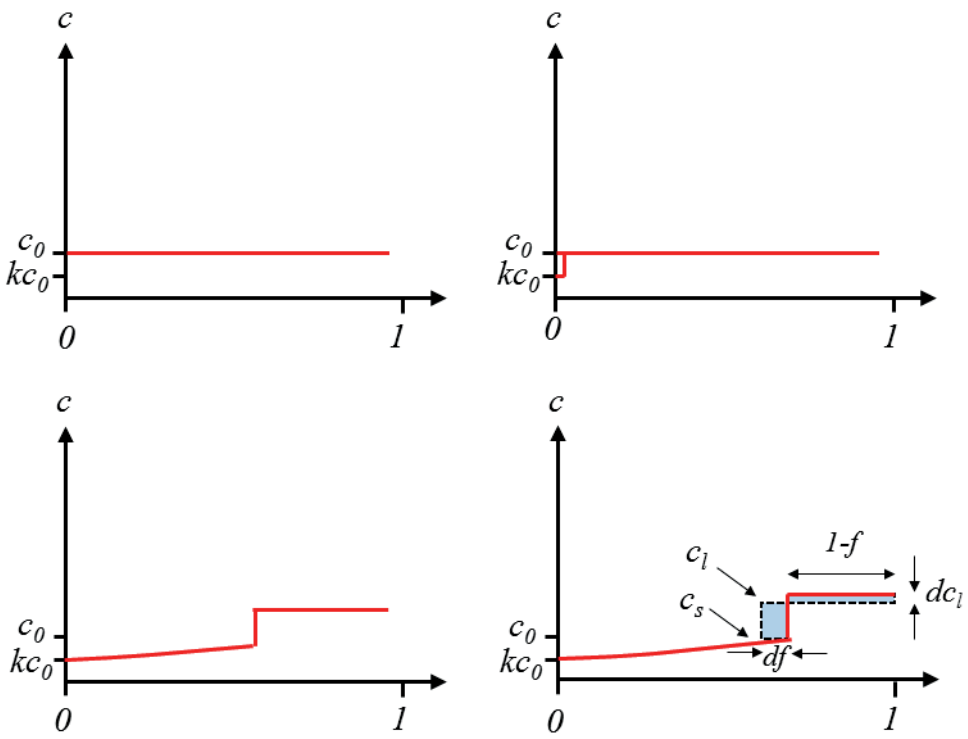

Fig. 2-17: Composition profile according to Scheil after [23].

the equalization of the amount of solute in the shaded areas leads to [23]:

$$(c_l - c_s)df = (1 - f)dc_l \tag{2-24}$$

the substitution of c_s using Eq. (**2-25**) gives Eq. (**2-26**) [23]:

$$c_s = kc_0 \tag{2-25}$$

$$(c_l(1 - k))df = (1 - f)dc_l \tag{2-26}$$

the integration of Eq. (**2-27**) from 0 to fs (fraction solid) and c_0 to c_l leads to Eq. (**2-28**) [23]:

$$\int_0^{f_s} \frac{df}{(1 - f)} = \int_{c_0}^{c_l} \frac{dc_l}{c_l(1 - k)} \tag{2-27}$$

$$-\ln(1-f_s) = \frac{1}{1-k} ln \frac{c_l}{c_0} \tag{2-28}$$

taking exponentials and rearranging results in Eq. (**2-28**), which is known as Scheil equation [23]:

$$c_l = c_0(1-f_s)^{(k-1)} \tag{2-29}$$

the constitutional undercooling, assuming that there is no thermal undercooling, can be given by Eq. (**2-30**) [12]:

$$\Delta T_c = m(c_l - c_0) \tag{2-30}$$

the substitution of Scheil equation into Eq. (**2-30**) leads to [12]:

$$\Delta T_c = mc_0[(1-f_s)^{(k-1)} - 1] \tag{2-31}$$

the differentiation of Eq. (**2-31**) is given by Eq. (**2-32**) [12]:

$$\frac{d\Delta T_c}{df_s} = mc_0(k-1)(1-f_s)^{(k-2)} \tag{2-32}$$

at f_s = 0 [12]:

$$\frac{d\Delta T_c}{df_s} = mc_0(k-1) = Q \tag{2-33}$$

which is Q, given by Eq. (**2-33**) . The same results can be obtained by using the lever rule, expressed by Eq. (**2-34**), instead of the Scheil equation, assuming that solidification occurs under equilibrium conditions [24]:

$$\frac{c_l}{c_0} = \frac{1}{1-(1-k)f_s} \tag{2-34}$$

the substitution of the lever rule into Eq. (**2-30**) leads to Eq. (**2-35**) [12]:

$$\Delta T_c = mc_0[\frac{1}{1-(1-k)f_s} - 1] \quad (2\text{-}35)$$

at f_s = 1:

$$\Delta T_c = mc_0\left[\frac{1-k}{k}\right] = P \quad (2\text{-}36)$$

which is the supercooling parameter P, given by Eq. (**2-36**). The differentiation of Eq. (**2-35**) is given by Eq. (**2-37**) and leads to Eq. (**2-38**) [12]:

$$\frac{d\Delta T_c}{df_s} = -mc_0\frac{(k-1)}{(1-(1-k)f_s)^2} \quad (2\text{-}37)$$

at f_s = 0:

$$\frac{d\Delta T_c}{df_s} = mc_0(1-k) = Q \quad (2\text{-}38)$$

which is Q. As a result, StJohn et al. [12] suggested that Q is a calculation of the rate of development of the constitutional zone in matters of the fraction solid at zero fraction solid and therefore at the beginning of solidification. It is shown that Q is independent on whether the solidification occurs under equilibrium conditions or not [12]. The relation, given by Eq. (**2-33**) and Eq. (**2-38**) represents the best way of calculating Q from thermodynamic models [21].

2.2.2.2.2 Calculation of Q

In binary systems Q can be calculated, either by the use of printed phase diagrams, or according to Eq. (**2-38**) using computer software, eliminating errors in obtaining data from printed phase diagrams. Assuming an idealized binary system with straight solidus and liquidus lines, m and k are independent of c_0 and can be obtained by the use of a printed phase diagrams, shown in **Fig. 2-18**. Q can be attained, either by calculation according to Eq. (**2-23**), or can be read out directly from the phase diagram [21,22].

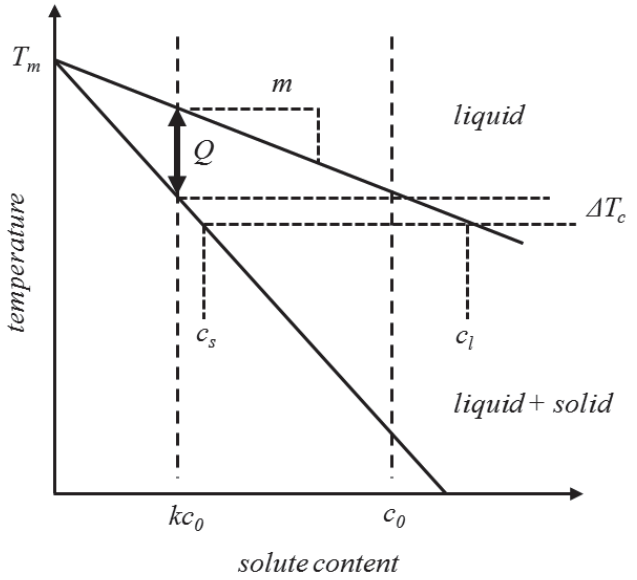

Fig. 2-18: Idealized binary phase diagram after [21].

Q in a multicomponent system can be calculated by means of Eq. (**2-39**) [25]:

$$Q_{\sum bin} = \sum Q_{bin,i} = \sum m_{bin,i}\left(k_{bin,i} - 1\right)c_{0,i} \tag{2-39}$$

where $m_{bin,i}$, $k_{bin,i}$ and $c_{0,i}$ are the liquidus slope, the partition coefficient and the concentration of each solute. The overall $Q_{\sum bin}$ is the summation of the individual $Q_{bin,i}$, of all the solutes. It is assumed that each solute acts as in a binary system and that $m_{bin,i}$ and $k_{bin,i}$ are independent of the amounts of the other solutes. However, the calculation of Q based on Eq. (**2-39**) is only reliable, if there is no interaction between the solutes, which is a gross simplification for higher compositions or strong interacting solutes [21,25].

Under the assumption that there is an interaction between the solutes of an alloy, the slope m_i of the liquidus surface T_L can be calculated at the multicomponent composition point vector $\overrightarrow{c_0}$ from partial derivation with regard to each solute i, keeping the other solutes j constant and disregarding the solvent composition, which is expressed by Eq. (**2-40**) [25]:

$$m_i = \left(\frac{\partial T_L}{\partial c_{0,i}}\right) \tag{2-40}$$

the equilibrium partition coefficient of each solute k_i is calculated at the multicomponent liquidus point (T_L, $\overrightarrow{c_0}$) from the tie line joining the solid ($c^*_{s,i}$) and the liquid ($c^*_{l,i}$) composition at the interface, which can be given by Eq. (**2-41**) [25]:

$$k_i = \left(\frac{c^*_{s,i}}{c^*_{l,i}}\right) \tag{2-41}$$

the GRF Q_{multi} of a multicomponent system with n solutes can be calculated according to Eq. (**2-42**) [25]:

$$Q_{multi} = \sum_{i=1}^{n} m_i(k_i - 1)c_{0,i} \tag{2-42}$$

2.2.3 Free-growth model

The free-growth model was first proposed by Bunn et al. [17] and is applied within an isothermal-melt model. The isothermal-melt model suggests that the growth of grains impedes further nucleation and therefore decreases the efficiency of the grain refiner. The impediment of further nucleation can be caused, either by impingement of the growing grains, by the solute diffusion fields around the growing grains, or by the thermal diffusion fields. Due to the fact that the solute diffusion length is less than the average distance between two active growth centres and that the thermal diffusion length is two to three times of magnitude greater than that range, a small volume of the melt can be assumed to be isothermal. Therefore, impingement of further nucleation by the thermal diffusion field is the dominant factor in decreasing the grain refinement efficiency [4,13].

As the melt is cooled below the liquidus temperature, potent nucleants can become active, acting as nucleating sites. At the beginning, larger particles become active first, and then smaller particles, as undercooling increases. Due to the latent heat release, caused by crystal growth, the rate of cooling slows down, leading to an increase in temperature, which is known as recalescence. As recalescence occurs, not further activation of smaller particles is possible. Due to the fact that recalescence limits further undercooling of the melt, it can be explained why only 1 wt% of added particles can act as nucleating sites. Within the isothermal-melt model two behaviours of particles can be identified. A low level of possible nucleating sites results in a high undercooling and therefore all particles are activated. At a high particle level, the fraction of potent nucleating sites is reduced due to recalescence, explaining the low particle efficiency [4,16].

The modification of the isothermal-melt model led to the free-growth model. If a nucleus is formed on the face of a particle (e.g. {0001} face of TiB_2) at a low undercooling, either by adsorption or as a spherical cap, the nucleus can grow across the face of the particle until it is extended over the whole face, but then further growth has to occur outwards by reducing the radius of curvature r of its interface with the melt. This radius cannot go below the critical

radius r_{cr}, dependent on the local temperature. If $d < 2r_{cr}$, free growth of the nucleus is not possible, where d is the diameter of the particle. It becomes possible only, if r_{cr} is reduced due to a higher undercooling. The undercooling ΔT_{fg} that is required to enable free growth of the nucleus is given by Eq. (**2-43**) [16]:

$$\Delta T_{fg} = \frac{4\gamma}{\Delta S_v d} \tag{2-43}$$

where ΔS_v is the entropy of fusion per unit volume. According to the isothermal-melt model a low inoculation level results in large undercoolings, activating all particles. The free growth model proposes that free growth can take place only on those particles, which are large enough to exceed the critical size in matters of ΔT_{fg}. According to the free-growth model, free growth takes place first on the biggest particles and then on finer particles as the undercooling increases, up to the point where recalescence occurs. The benefit of the free growth model is that the required undercooling for free growth is related to the particle size, as shown in **Fig. 2-19.** As the actual nucleation is not the limiting transformation step but the size distribution of the particles, the fraction of active particles can be increased by decreasing the spread of particle size [4,13,16].

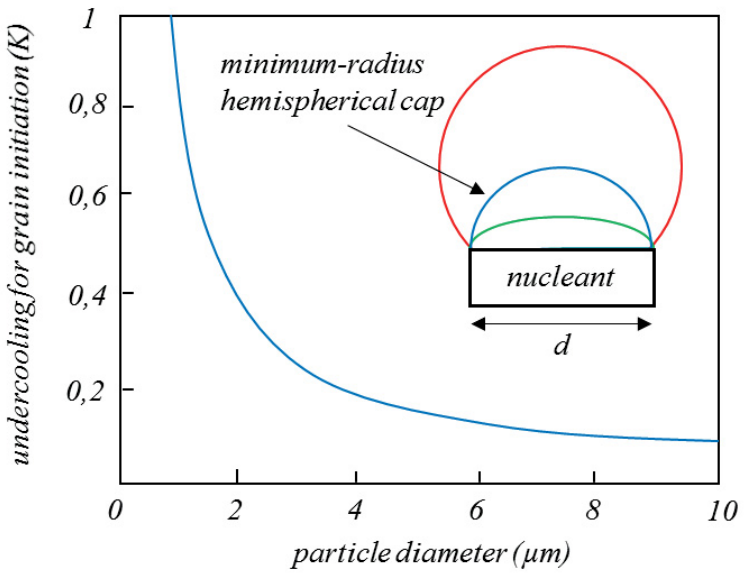

Fig. 2-19: The undercooling required for nucleation according to the free-growth model as a function of the particle diameter after [16].

Furthermore, the free growth model shows good compliance with experiments, describing the variation of the grain size as a function of the cooling rate and the solute level in the melt, respectively the constitutional undercooling, which is expressed by Q. As the grain size decreases with increasing cooling rate and increasing Q, the efficiency of grain refinement is dependent on the balance between latent heat production and heat extraction. Since the latent heat production is limited by the solute partitioning at the solid-liquid interface and the diffusion in the melt Q is a good parameter to describe the influence of the solutes on grain refinement, shown in **Fig. 2-20** [16,26].

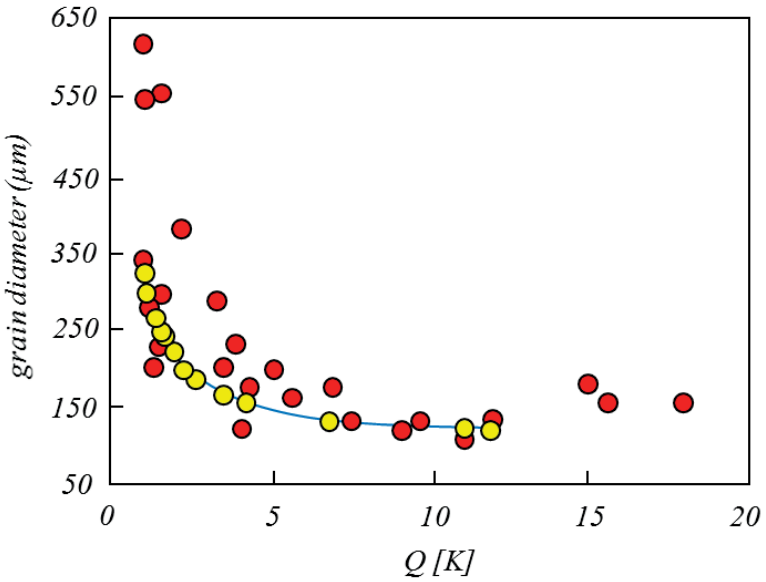

Fig. 2-20: Grain size as a function of Q for a standard TP-1 test with 2 ppt addition of Al-5Ti-1B refiner. Data from Spittle and Sadli [26] (●), predictions from the free growth model (●) after [16].

2.3 Grain refinement of copper and copper alloys

Most of the work concerning grain refinement has been carried out on the grain refinement of aluminium alloys, even though there has been much practical work on the grain refinement on copper and copper alloys, induced by Cibula [27], Dennison and Tull [28] in the 1950s. Further investigations were carried out in the 1960s by Henke [29] and Röhrig [30], in the 1970s by Couture and Edwards [31], in the 1980s by Romankiewicz and co-workers [32] and furthermore by Reif, Weber and Mannheim [6,33]. Later work has been carried out by Romankiewicz and co-workers [34] in the 1990s and by Sadayappan and co-workers [35] at the Materials Technology Laboratory (MTL) from 1991 to 2004. Despite the numerous works that have been carried out since the early 1950s, grain refinement in copper alloys is less popular as compared to other systems, especially as compared to aluminium alloys and the mechanism of grain refinement in copper alloys is still not well understood [5,34,35].

The literature review shows that the grain refinement of copper and copper alloys seems to be of a more complex mechanism that is strongly dependent on the alloy system, the range of the alloying elements, the impurities and the casting conditions and therefore the different copper alloys have to be considered separately [6]. The following chapters give an overview of the grain refinement of copper alloys with a focus on the copper-tin system.

2.3.1 General grain refinement possibilities of copper and copper alloys

A general possibility of grain refinement in copper and copper alloys is achieved by a decrease in the casting temperature and holding time. The grain refinement mechanism of this method is supposed to be of a primarily crystallisation in the pouring stream. Therefore, the primary crystals are well dispersed in the melt and can act as nucleants. However, this method is of small importance because of technical reasons [6,29].

Grain refinement of copper and copper alloys can be obtained in general by the addition of iron and cobalt because of a primarily solidification of iron and cobalt crystals due to peritectic systems, which are shown in **Fig. 2-21**. However, the required concentrations of iron and cobalt of about 3 to 4 wt% are not acceptable in commercial alloys as they would affect the mechanical properties [6,29].

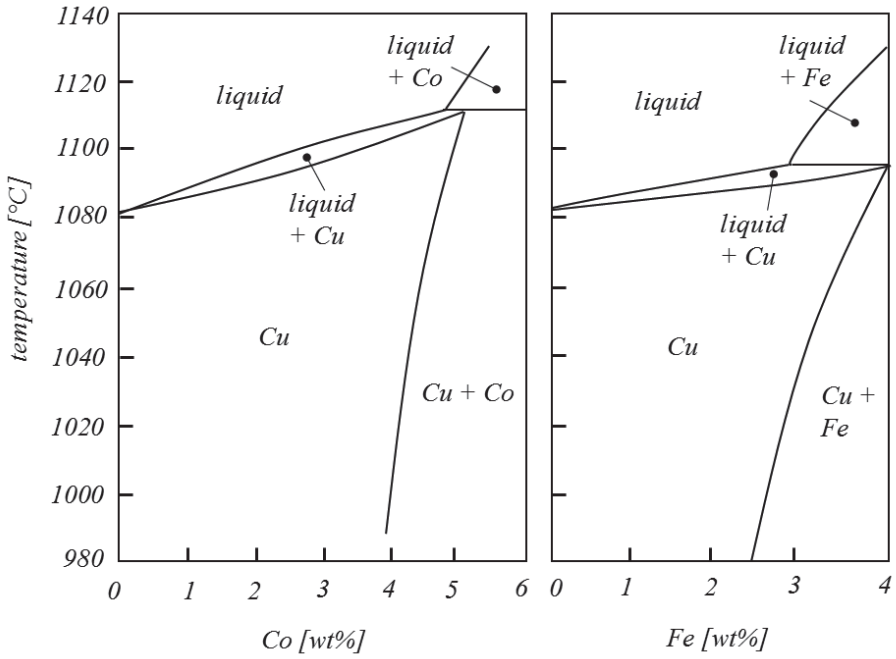

Fig. 2-21: Phase diagrams of the Cu-Co and Cu-Fe system after [29].

Grain refinement of pure copper can be obtained by the addition of iron in amounts of ≤ 2,5 wt%, by the addition of lithium and/or bismuth in amounts of 0,05 wt%, respectively 0,05 to 0,5 wt%, potentially in combination with antimony in concentrations of 0,5 wt%. Furthermore, grain refinement can be achieved by a combination of 0,5 wt% antimony with 0,01 wt% tungsten, 0,02 wt% iron or 0,02 wt% cobalt. The addition of lithium, as a strong deoxidising reagent, should be carried out after a deoxidation with phosphorus [6,29].

As grain refinement of copper requires both growth restriction and inoculation [16,36], Romankiewicz and co-workers [34] proposed possible compounds with a good lattice match with copper. An abstract is shown in **Tab. 2-1**. As the misfit of all compounds is in excess of 15 wt%, a model is proposed to describe the grain refinement efficiency of the compounds in spite of such a high lattice disregistry, shown in **Fig. 2-22**. It is suggested that the rotation of crystallographic planes leads to a decrease in the lattice disregistry (e.g. Fe_2B from 41,60 wt% to 0,44 wt%), which enables heterogeneous nucleation according to the carbide/boride model [34].

Furthermore, Romankiewicz and co-workers [34] showed the influence of the alloying elements on the lattice dimension of copper, shown in **Fig. 2-23**, leading to a decrease in the lattice disregistry.

Tab. 2-1: Structure, lattice dimension and lattice disregistry of compounds before and after the rotation of crystallographic planes supposed by Romankiewicz et al. [34].

compound	structure	lattice dimension [Å]		lattice disregistry [%]	lattice disregistry after rotation of planes [%]
		a	b/c		
ZrB_2	hcp	3,170	3,530	23,44	-
TiB_2	hcp	3,030	3,230	18,45	-
VB_2	hcp	2,998	3,057	17,20	-
WC	hcp	2,900	2,880	13,37	-
ZrC	fcc	4,700	-	29,78	-
TiC	fcc	4,324	-	19,23	-
TiN	fcc	4,243	-	17,78	-
Fe_2B	tetragonal	5,109	4,250	41,60	+0,44
Co_2B	tetragonal	5,016	4,220	39,06	-1,38
Ni_2B	tetragonal	4,993	4,249	38,42	-1,83

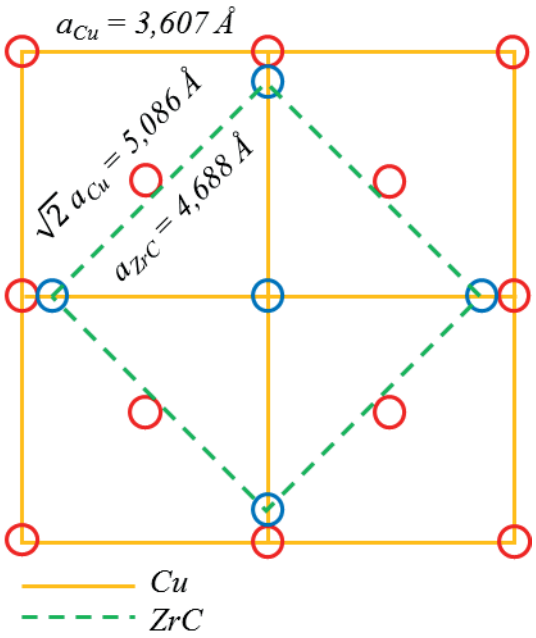

Fig. 2-22: Rotation of crystallographic planes by means of ZrC after [34].

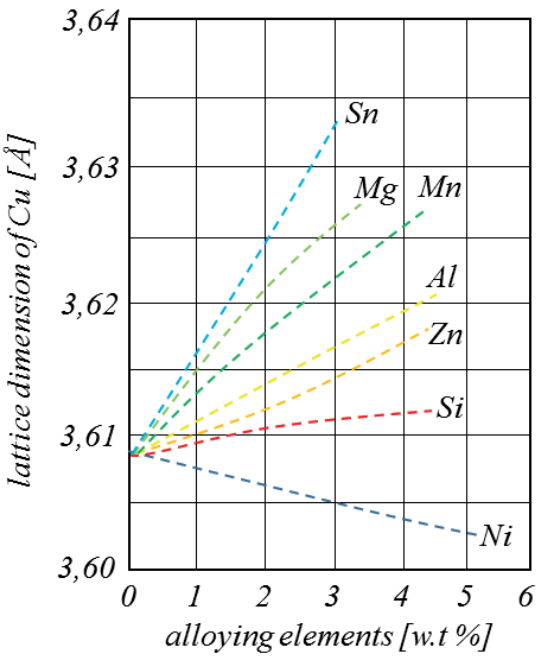

Fig. 2-23: Influence of the alloying elements on the lattice dimension of copper after [34].

A grain refinement method, generally applicable to a range of different types of copper alloys, was developed by Reif and Weber [37,38]. The grain refiner is of the type:

A (Zr) + B (Mg) + C (Fe) + D (P)

where element (A) can be substituted by titanium, element (B) by lithium, sodium, potassium, beryllium, calcium, strontium and barium, element (C) by scandium, yttrium, titanium, zirconium, hafnium, vanadium, niobium, tantalum, chromium, molybdenum, tungsten, manganese, technetium, rhenium, ruthenium, osmium, cobalt, rhodium, iridium, nickel, palladium, platinum, silver, gold, zinc, cadmium, mercury and the rare earth elements, element (D) by aluminium, gallium, indium, silicon, germanium, tin, lead, arsenic, antimony, bismuth, sulphur, selenium and tellurium. The diversity of assumed types of grain refiners by Reif and Weber [37,38] shows the lack in understanding the grain refinement mechanism of copper at this time.

2.3.2 Grain refinement of copper-tin alloys

As there has been not much practical work on the grain refinement of copper-tin alloys and therefore the mechanism is not well understood. The following chapter gives an overview of the grain refinement of copper-tin alloys and focuses on the results of Cibula [27] and Mannheim, Reif, Weber [6].

2.3.2.1 Overview

Grain refinement of copper-tin alloys can be achieved by the addition of zirconium, titanium, vanadium and niobium. The grain refinement effect of titanium can be increased by the addition of boron, whereas the effect of zirconium is decreased. The single addition of boron has no effect on the grain refinement of copper-tin alloys.

If zirconium and sulphur are present in the melt at the same time, the effect of zirconium is decreased. It is supposed that the formation of ZrS_2 disables the grain refinement effect of zirconium. Therefore, the maximum sulphur content should be ≤ 0,01 wt%. The negative influence of sulphur can be compensated by the addition of magnesium.

Furthermore, grain refinement can be achieved be the addition of iron, cobalt and titanium in combination with boron. It is supposed that TiB_2, FeB and CoB can act as nucleants.

The grain refinement effect of all additional elements is improved by an increase in the tin content, whereas zinc shows no influence.

A degassing treatment with nitrogen in addition with a charcoal covering leads to an increase in the grain refinement effect of zirconium [6].

2.3.2.2 Grain refinement of bronzes (≤ 12 wt% tin)

The work, carried out by Cibula [27] in the early 1950s, shows the influence of titanium, vanadium, niobium, zirconium, iron, manganese, nickel, chromium and boron, as well as the influence of the melting conditions and sulphur on the grain refinement effect of phosphorus deoxidized bronzes with 10 wt% tin and up to 1 wt% aluminium. With the exception of zirconium, the addition of boron results in refinement at smaller concentrations of the alloying elements. The grain diameter as a function of the concentration of the most effective grain refiners is shown in **Fig. 2-24**.

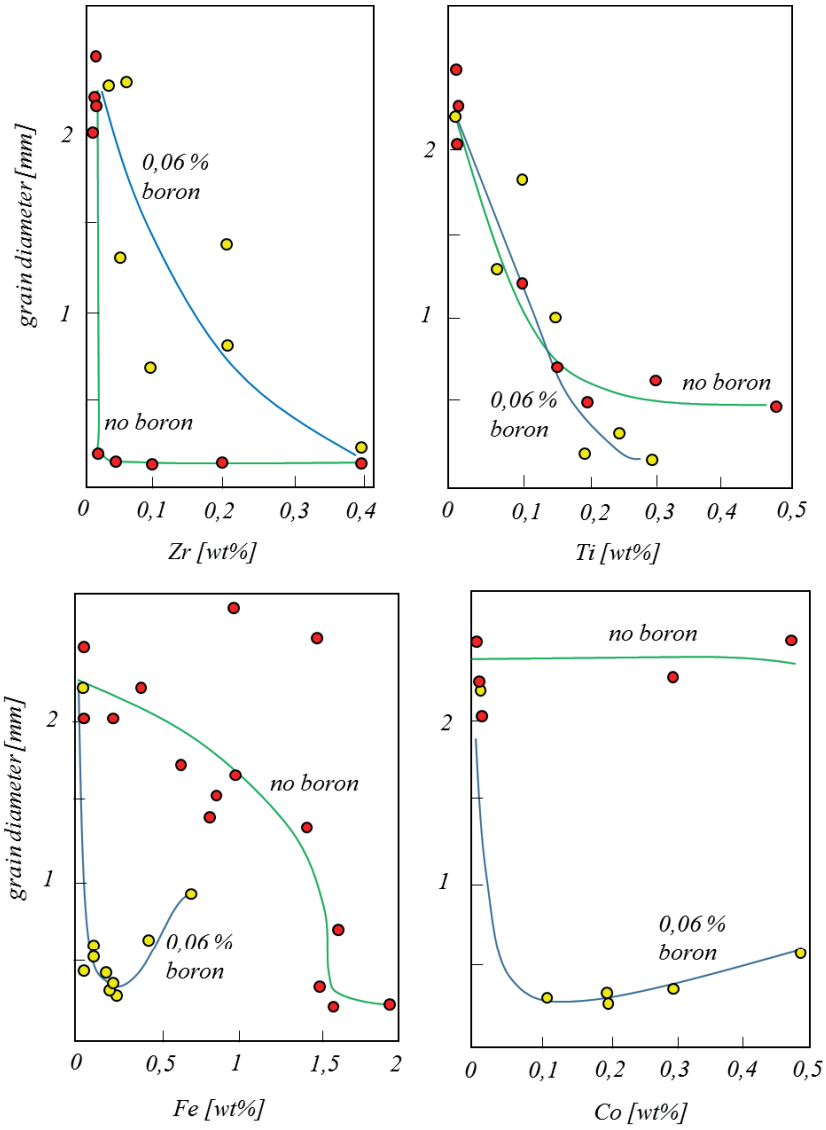

Fig. 2-24: Grain diameter as a function of the zirconium, titanium, iron and cobalt content with no boron and boron additions of 0,06 wt%, 19 mm diameter sand-cast bar, cast at 1150°C after [27].

In the absence of boron, additions of manganese up to 1 wt% and nickel up to 2 wt% have slight effects on the grain size. Additions of chromium at contents of 1 wt% show moderate effect on the grain size. The grain refinement effect of zirconium is highly influenced by the melting conditions. The maximum effect can be obtained, if carbon is in contact with the melt in the presence of nitrogen degassing [27].

Boron alone has no effect on the grain size, but increases the grain refinement effect of titanium, cobalt and iron. Furthermore, boron shows no influence on the grain refinement with chromium and manganese and only slight influence with nickel. The combination of boron with niobium effects the grain size in a similar way as with titanium [27].

The grain diameter as a function of the tin content in combination with several refining additions is shown in **Fig. 2-25** [27].

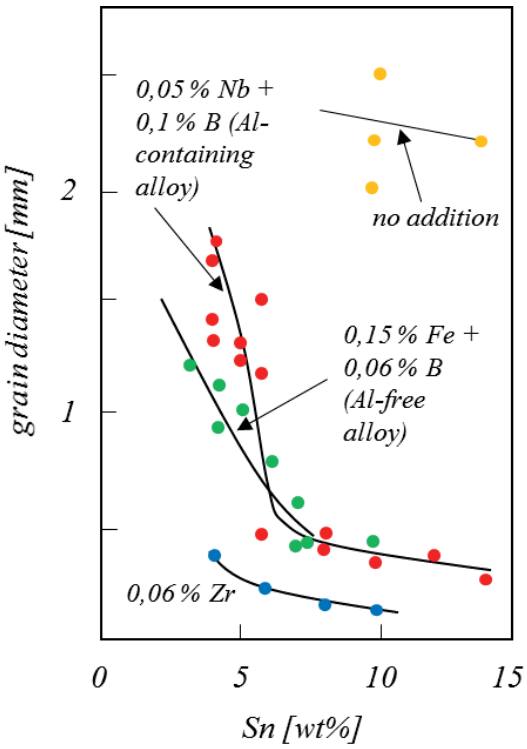

Fig. 2-25: Grain diameter as a function of the tin content in combination with several refining additions, 19 mm diameter sand-cast bar, cast at 1150°C after [27].

Later work, carried out by Mannheim, Reif and Weber [6] in 1988, shows the grain refinement efficiency of zirconium, iron and boron on copper-tin alloys with a tin content below 12 wt%. The influence of single additions of zirconium and boron on the grain size of copper-tin alloys with 4 wt%, respectively 8 wt% tin, as well as on the grain size of pure copper is shown in **Fig. 2-26**. The grain size, both of pure copper as well as of CuSn4, respectively CuSn8, is remarkably decreased by the addition of zirconium in amounts of 0,02 to 0,06 wt%. A further increase in the zirconium content results in no further decrease in the grain size. The single addition of boron leads to a strong increase in the grain size of CuSn4 and CuSn8. It is supposed that boron reacts with phosphorus and oxygen to B_2O_3-P_2O_5 that is segregated at the grain boundaries and therefore without any influence on grain refinement. In this context, a further explanation might result in the fact that boron

compounds, tend to reach the critical particle size within short times, which result in a floating of particles to the melt surface [6].

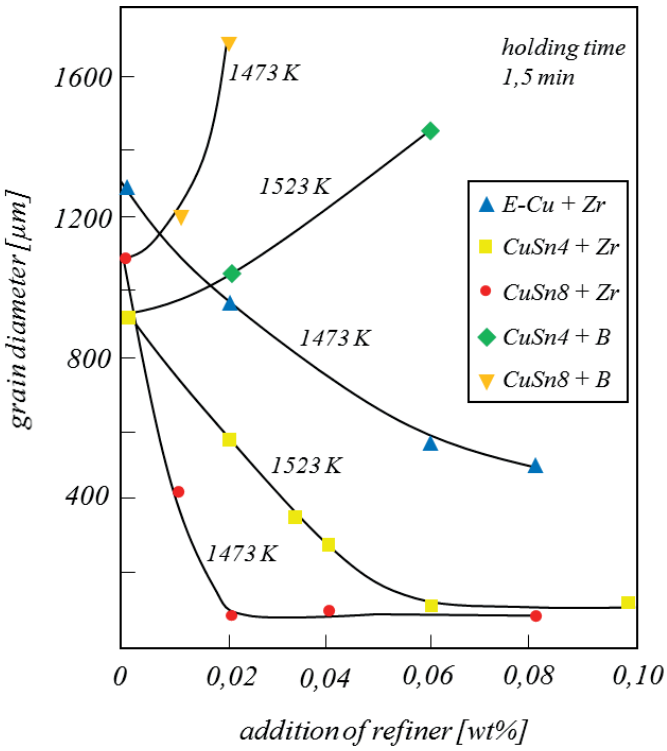

Fig. 2-26: Grain diameter as a function of the zirconium and boron content after [6].

Fig. 2-27 shows the influence of phosphorus on the grain refining effect of zirconium. It is shown that a minimum of 0,01 wt% phosphorus is required to achieve grain refining by the addition of zirconium. Scanning electron microscopy (SEM) analysis show compounds of zirconium, phosphorus, oxygen and sulphur in the centre of the grains. It is supposed that $(ZrO)_2P_2O_7$ particles with fractions of sulphur can act as nucleants [6].

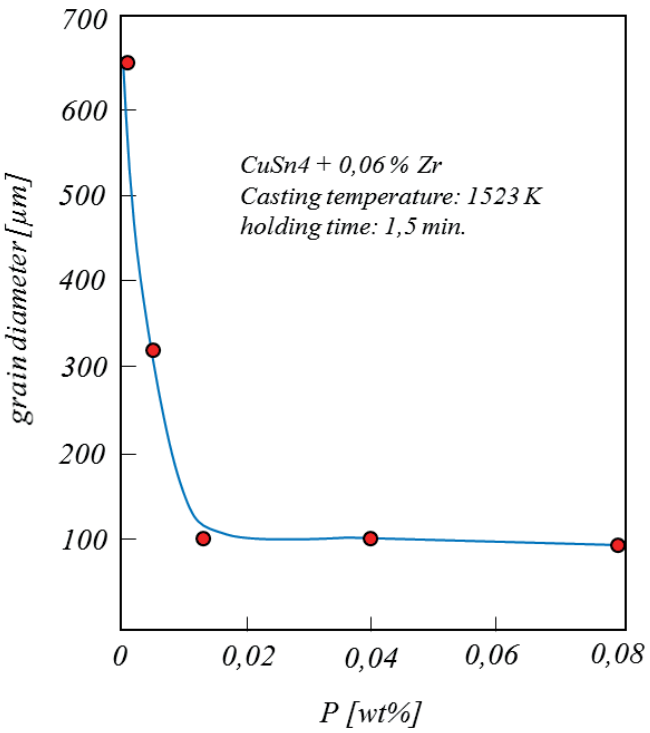

Fig. 2-27: Influence of phosphorus on the grain refinement effect of zirconium after [6].

The addition of both, zirconium and boron, leads to inconsistent results, shown in **Fig. 2-28**. If boron and zirconium are added in form of binary alloys, the grain refinement effect of zirconium is annihilated by the addition of boron and the grain size increases with increasing boron content. In the case of the addition in form of a ternary CuZrB – master alloy, boron shows no influence on the grain refinement effect of zirconium. It is assumed that boron constricts the effect of zirconium by inhibitation of the formation of Zr-P-O-(S) compounds in the case of the addition in form of binary alloys. Due to a higher stability of B_2O_3 in comparison to ZrO_2, it is supposed that rather B_2O_3-P_2O_5 is formed than $(ZrO)_2P_2O_5$. The contradictory results by the addition in form of ternary alloys is not well understood [6].

Grain refinement, achieved by the addition of ternary Cu-Zr-Fe – master alloys, shows a remarkable decrease in the grain size, shown in **Fig. 2-29**. Due to the fact that SEM analysis show Zr-P-O – compounds in the grain centres, it is supposed that zirconium plays the dominant role in the grain refinement by the addition of zirconium and iron [6].

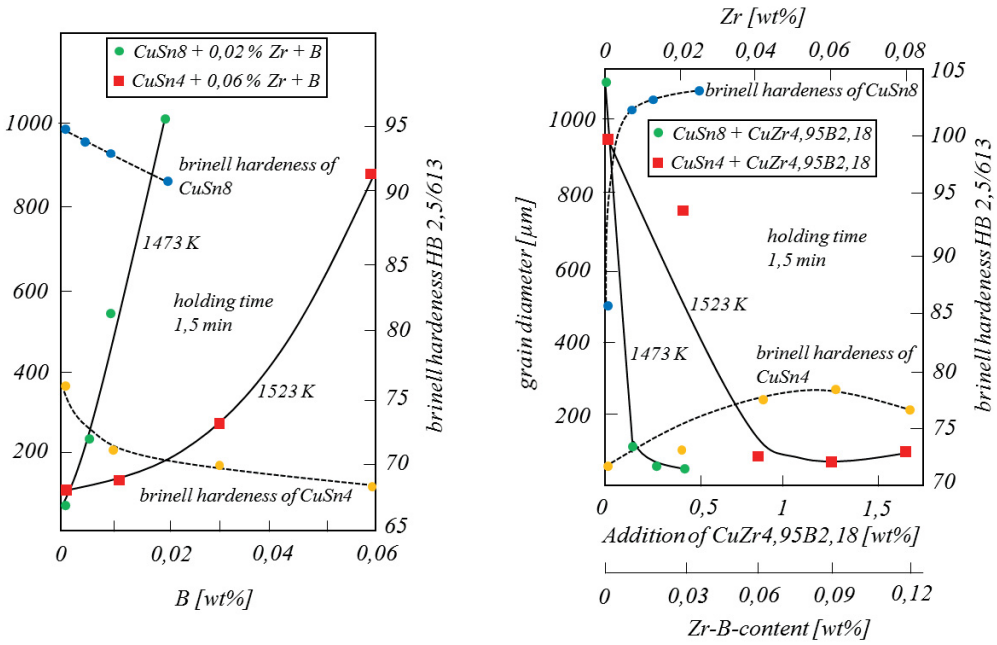

Fig. 2-28: Influence of boron on the grain diameter and the brinell hardeness of CuSn4 and CuSn8, addition in form of binary CuZr-CuB alloys (left), influence of zirconium and boron on the grain diameter and the brinell hardeness, addition in form of a Cu-Zr-B – master alloy after [6].

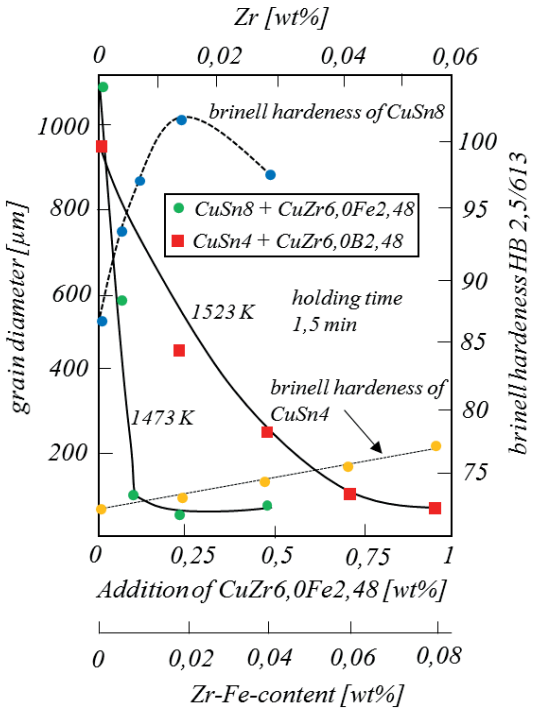

Fig. 2-29: Grain diameter and brinell hardeness as a function of the zirconium and iron content after [6].

3 Experimental procedure

3.1 Calculation of Q by the use of binary alloy phase diagrams

Q in binary alloy systems was determined by the use of binary alloy phase diagrams [39], assuming that both the liquidus line and the solidus line are straight and therefore m and k are independent of the alloy composition. The majority of the Q values of the binary systems was calculated at an alloy composition of c_0 = 1 wt%, using AutoCAD© software. The determination of Q is schematically shown in **Fig. 3-1** for the copper-tin system at a tin content of 5 wt%. The calculation of Q according to [12,21] and mentioned in **2.2.2.2.1** and **2.2.2.2.2** is given by Eq. (**3-1**) to (**3-5**).

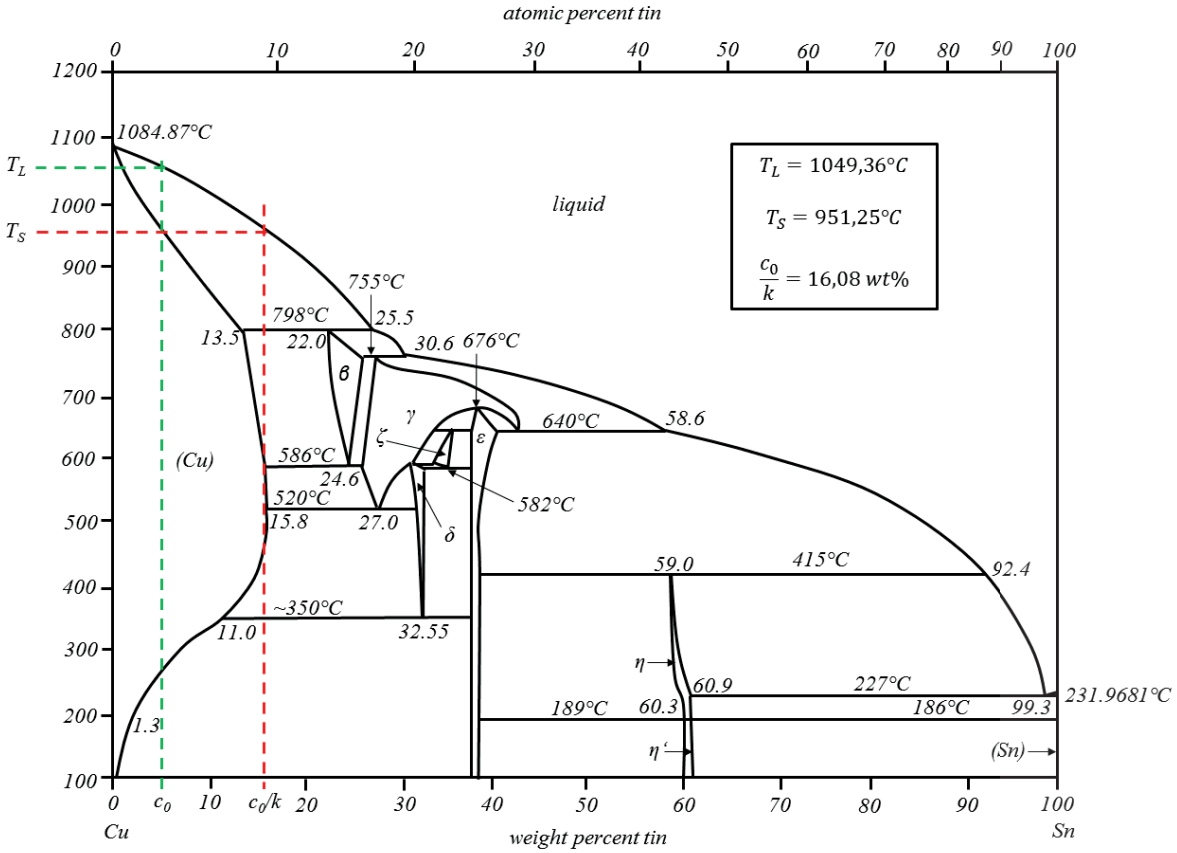

Fig. 3-1: Determination of Q of the copper-tin system at a tin content of 5 wt% after [39].

$$\Delta T = T_L - T_S = 1049{,}36 - 951{,}25 = 98{,}11\ [K] \tag{3-1}$$

$$k = \frac{c_0}{16{,}08} = 0{,}31 \tag{3-2}$$

$$m = -\frac{\Delta T}{\Delta c} = -\frac{98{,}11}{11{,}08} = -8{,}85\ [\frac{K}{wt\%}] \tag{3-3}$$

$$Q = m * (k-1)c_0 = -8{,}85(0{,}31 - 1)5 = 30{,}51\ [K] \tag{3-4}$$

$$Q/c_0 = \frac{30{,}51}{5} = 6{,}1\ [\frac{K}{wt\%}] \tag{3-5}$$

3.2 Nucleation sites for copper alloys

As already mentioned in **2.2.1.1**, a small disregistry with the copper lattice (a_{cu} = 3,61 Å) is one of the main requirements for an efficient grain refiner. Suitable nucleating compounds for pure copper and copper-base alloys were examined with regard to their lattice disregistry to the copper lattice. Suitable borides, carbides, nitrides, oxides, sulphides and phosphides [40,41] were investigated in compliance with the carbide/boride theory, mentioned in **2.2.1.2** and **2.2.1.2.1**. As several compounds show lattice dimensions in the range of 5, respectively 10 Å, the rotation of the (001) crystallographic plane of the cubic and tetragonal structure was examined, according to [34], in addition to the related crystallographic planes of the cubic, tetragonal, orthorhombic and hexagonal structure, mentioned above. **Fig. 3-2** shows two models of the rotation of the (001) plane, according to [34] (model 1, left side) and personal consideration (model 2, right side).

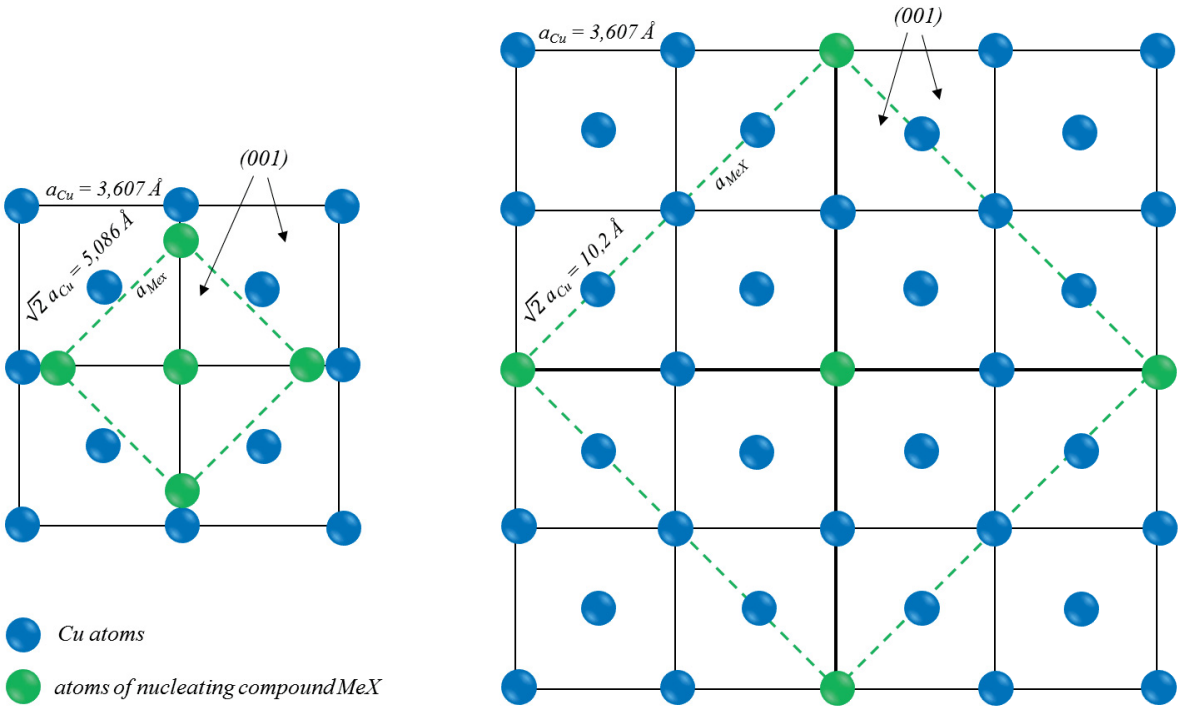

Fig. 3-2: Rotation of the (001) plane of the cubic and tetragonal structure, adapted from [34].

3.3 Melting experiments

An induction heater (Cheltenham© ISM HF20) with a maximum power of 20 kW and a frequency range of 50 to 150 kHz was used as a melting device, shown in **Fig. 3-3**. The power was regulated at 16 kW. Graphite crucibles (A5) with a zirconium silicate coating and a maximum capacity of 5 kg for copper were used to contain the alloy melt. To avoid oxidation of the melt the crucibles were covered with a refractory brick. Furthermore, the heating and holding of the alloy were carried out under argon atmosphere with an argon flow of 1-4 [l/min]. Deoxidised pure copper, 99,995 wt% Cu, was used as base material. Alloying was performed by the addition of Cu-15P, Cu-25Fe and Cu-50Mg master alloys, respectively high purity tin and zinc. 800 g was specified as the target value for the alloy calculation. **Tab. 3-1** and **Tab. 3-2** show the solute concentrations of the conducted test series on the basis of the obtained Q values of tin, zinc, phosphorus, magnesium and iron, shown in **4.1**. The charged pure copper was melted at a regulated power of 16 kW in time steps of 50 seconds at approximately 1200°C. During the break of the heating cycle alloying was performed in addition to a stirring in the order of 10 seconds with a graphite coated spoon, preheated at 320°C in a heat treatment furnace. After the alloying step the melt was reheated for 25 to 50 seconds at approximately 1200°C. The melt temperature was controlled using a thermocouple. As the melt temperature reached a temperature of 1150°C +/- 10°C, the melt was poured in the TP-1 moulds, coated with a graphite coating and preheated at 320°C. Due to a low melt volume, the melt was poured in the TP-1 moulds in air, followed by a rapid transfer to the water quench, where the moulds were left for 2 minutes. The ASTM© TP-1 test device and the TP-1 mould are shown in **Fig. 3-4** and **Fig. 3-5**.

Tab. 3-1: Solute concentration, corresponding Q-value and sample identification of the tin and zinc test series.

	0	**0,1**	**0,5**	**1,0**	**1,5**	**2,0**	**5,0**	**[wt%]**
Sn	0	0,6	2,9	5,8	8,7	11,6	28,9	Q-value
	R I	SN I	SN II	SN III	SN IV	SN V	SN VI	
Zn	**0**	**0,100**	**0,500**	**1,000**	**1,500**	**2,000**		**[wt%]**
	0	0,2	0,8	1,6	2,4	3,1		Q-value
	R II	ZN I	ZN II	ZN III	ZN IV	ZN V	ZN VI	

Tab. 3-2: Q-values, corresponding solute concentrations and sample identifications of the phosphorus, magnesium and iron test series.

	0	0,1	0,5	1	2	4	8	Q-value
P	0	0,003	0,016	0,031	0,063	0,125	0,251	[wt%]
	R III	P I	P II	P III	P IV	P V	P VI	
Mg		0,004	0,022	0,045	0,090	0,180	0,360	[wt%]
	R IV	MG I	MG II	MG III	MG IV	MG V	MG VI	
Fe		0,009	0,044	0,088	0,175	0,351	0,701	[wt%]
	R V	FE I	FE II	FE III	FE IV	FE V	FE VI	

Fig. 3-3: Induction heater Cheltenham© ISM HF20, water-cooled copper coil, graphite crucible A5.

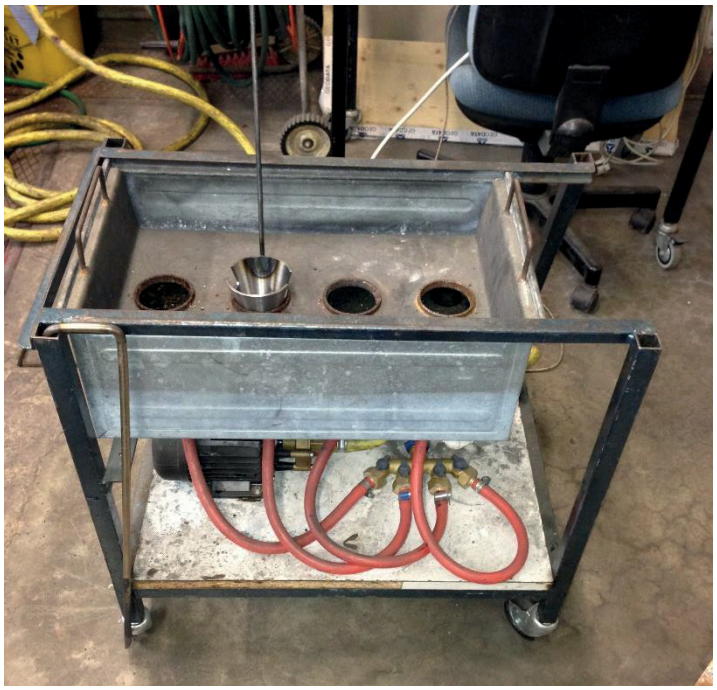

Fig. 3-4: TP-1 test device with inserted TP-1 mould.

Fig. 3-5: TP-1 mould.

3.3.1 Sample preparation

The samples, shown in **Fig. 3-6**, were sectioned horizontally using a turning machine to obtain samples with a high of 38 mm, shown in **Fig. 3-7**. An ATM© Saphir 350 E grinding machine, shown in **Fig. 3-8** was applied to grind the samples manually, starting with a 80-grit abrasive paper, followed by 320-grit, 800-grit, 1200-grit and 2500-grit abrasive paper for fine grinding, using water as cooling medium. For rough polishing 3 µm water based diamond suspensions in addition to lubricant was used. The samples were cleaned with water, sprayed with ethanol and dried after the first polishing step. Final polishing was performed using 9,6 ml OP-S suspension + 0,2 ml H_2O_2 (3 %) + 0,2 ml NH_3 (30 %). After final polishing the samples were cleaned carefully with water and ethanol.

To observe the grain size, the samples were etched immediately after the final polishing step for approximately 10 seconds, using 50 ml copper-ammonium chloride + 5 ml NH_3 (25 %). A finished prepared sample is shown in **Fig. 3-9**.

Fig. 3-6: TP-1 sample.

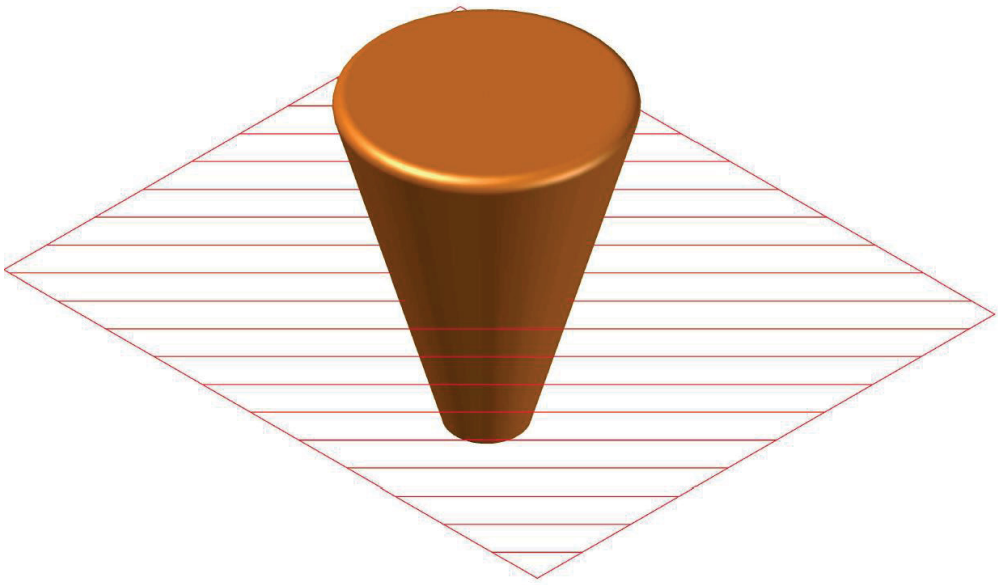

Fig. 3-7: Intersecting plane of the TP-1 samples.

Fig. 3-8: Grinding and polishing machine ATM© Saphir 350 E.

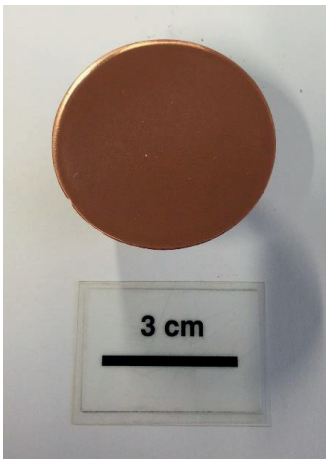

Fig. 3-9: Finished prepared sample.

3.3.2 Microscopy

To determine the grain size of the prepared samples a Zeiss© AXIO Imager.A1m optical microscopy in addition to NIKON© NIS-Elements BR 3.0 software was used, shown in **Fig. 3-10**. The determination of the grain size was carried out referring to [42]. 5 randomly chosen sections in the middle of the sample were examined at a magnification of 12,5X (intercept method [42]). In the case where no intercept method could be applied, several single detectable grains were measured.

Fig. 3-10: Optical microscopy Zeiss© AXIO Imager.A1m.

4 Results

In this section the results obtained from the calculation of Q by the use of binary phase diagrams are presented. Furthermore, possible nucleation sites for copper alloys are presented regarding to their lattice disregistry to the copper lattice and their melting points. The variation of the grain size of high purity copper (99,995 wt%) by the addition of tin, zinc, iron, magnesium and iron is shown and discussed in section **5**.

4.1 Calculation of the Q by the use of printed binary phase diagrams

The values of the partition coefficient k, the liquidus slope m and Q of 63 alloying elements, obtained by the use of binary phase diagrams [39], according to Eq. (**2-23**), are shown in **Tab. 4-1**. Missing elements, e.g. tungsten, molybdenum, are disregarded due to a low resolution of the binary phase diagrams. 9 alloying elements show a Q above a value of 20 K/wt%, primarily elements with a high affinity for oxygen, e.g. phosphorus, lithium, magnesium, calcium [43]. The majority of the alloying elements show values of Q of approximately 10 K/wt% and below.

Tab. 4-1: The values of Q, the liquidus slope m and the partition coefficient k of 63 solutes of the copper system.

element	k	m	Q/c_0	system	element	k	m	Q/c_0	system
-	-	[K/wt%]	[K/wt%]	-	-	-	[K/wt%]	[K/wt%]	-
P	0,16	-37,82	**31,88**	eutectic	Zr	0,08	-9,58	**8,80**	eutectic
Be	0,40	-51,28	**30,77**	peritectic	Er	0,05	-9,01	**8,59**	eutectic
Li	0,28	-32,21	**23,31**	eutectic	Nb	0,48	-16,32	**8,49**	eutectic
Y	0,11	-25,82	**23,04**	eutectic	Lu	0,05	-8,90	**8,44**	eutectic
Mg	0,36	-34,52	**22,23**	eutectic	Ti	0,33	-11,29	**7,58**	peritectic
Pt	5,24	5,24	**22,22**	mc	Sb	0,12	-8,57	**7,53**	eutectic
Ca	0,14	-23,83	**20,43**	eutectic	Ba	0,02	-7,50	**7,36**	peritectic
Sc	0,10	-22,40	**20,16**	eutectic	Th	0,05	-7,01	**6,70**	eutectic
Ir	3,85	6,76	**19,23**	peritectic	S	0,68	-20,79	**6,65**	eutectic
Ni	3,85	6,14	**17,46**	mc	Sn	0,19	-7,16	**5,78**	peritectic
B	0,39	-25,53	**15,48**	eutectic	Se	0,45	-10,53	**5,74**	eutectic
Pr	0,07	-14,15	**13,22**	eutectic	Ru	0,26	-7,47	**5,51**	eutectic
Te	0,50	-26,15	**13,08**	eutectic	U	0,04	-5,60	**5,37**	eutectic
Nd	0,06	-12,65	**11,94**	eutectic	Tc	0,33	-7,28	**4,86**	eutectic
La	0,06	-12,61	**11,91**	eutectic	Cd	0,16	-5,75	4,83	peritectic
Sm	0,05	-12,29	**11,64**	eutectic	Hf	0,06	-5,07	**4,79**	eutectic
Pm	0,05	-12,15	**11,49**	eutectic	Ge	0,40	-7,45	**4,48**	peritectic
Fe	5,88	2,34	**11,41**	peritectic	Co	1,86	4,40	**3,80**	peritectic
Ce	0,06	-11,86	**11,20**	eutectic	Bi	0,18	-4,39	**3,60**	eutectic
As	0,14	-12,76	**10,95**	eutectic	Pb	0,03	-3,43	**3,34**	eutectic
Tm	0,06	-11,46	**10,78**	eutectic	In	0,48	-6,12	**3,18**	peritectic
Hg	0,28	-14,85	**10,73**	eutectic	Tl	0,03	-3,27	**3,17**	eutectic
Tb	0,05	-11,25	**10,71**	eutectic	Ag	0,33	-4,59	**3,06**	eutectic
Gd	0,05	-11,11	**10,57**	eutectic	Rh	1,62	4,49	**2,79**	mc
Pd	4,77	2,79	**10,52**	mc	Cr	0,51	-5,03	**2,45**	eutectic
Sr	0,04	-10,92	**10,43**	peritectic	Ga	0,59	-5,71	**2,35**	peritectic
Dy	0,05	-10,71	**10,23**	eutectic	Mn	0,74	-8,69	**2,25**	mc
Ho	0,05	-10,08	**9,61**	eutectic	Au	0,40	-2,84	**1,70**	mc
Yb	0,04	-9,98	**9,55**	eutectic	Zn	0,31	-2,29	**1,57**	peritectic
Si	0,56	-21,47	**9,34**	peritectic	Al	0,50	-3,07	**1,53**	eutectic
Eu	0,04	-9,52	**9,15**	eutectic	V	1,28	4,55	**1,28**	peritectic
Pu	0,04	-9,42	**9,04**	eutectic					

4.2 Nucleation sites for copper alloys

The crystallographic structure, the lattice dimension and the lattice disregistry of suitable binary compounds by taking into consideration only the lattice disregistry, while disregarding the thermodynamic stability, are shown in **Tab. 4-2** to **Tab. 4-6**. A suitable boundary in the lattice disregistry was fined at 5 %, according to [44]. The majority of the compounds show a lattice disregistry greater than 5 %, seeming to be less suitable for effective nucleation. As several compounds show lattice dimensions in the range of 5, respectively 10 Å, the rotation of the (001) crystallographic plane of the cubic and tetragonal structure leads to a remarkably decrease in the lattice disregistry. A comprehensive list of the examined compounds is given in the **Appendix**.

Fig. 4-1 shows suitable binary compounds, regarding the lattice disregistry and the melting point of the compounds. Compounds, found in **Tab. 4-2** to **Tab. 4-6**, with a melting point less than 1300°C and positive energy of formation(*) [40,43,45,46,47] are disregarded in **Fig. 4-1**. In the case that values of the melting points could not be obtained, they were supposed in the case that the element forms several compounds(+). Compounds, found in the upper right area of **Fig. 4-1**, seem to be the most suitable nucleation sites.

Tab. 4-2: Crystallographic structure, lattice dimension and lattice disregistry of the most suitable borides.

compound	melting point [K]	crystallographic structure	lattice dimension [Å]		misfit [%]		rotation of planes, misfit [%]
			a	c	(001)	(100)	(001)
$YB_{x(x\sim3)}$(+)	2873[48]	tetragonal	3,78	3,55	4,71	-1,66	-
Ni_2B	1398[47]	tetragonal	4,98	4,24	37,95	17,45	-2,45
Co_2B	1553[48]	tetragonal	5,01	4,21	38,78	16,62	-1,87
Fe_2B	1662[46]	tetragonal	5,10	4,24	41,27	17,45	-0,10
MnB_2	2100[47]	tetragonal	5,15	4,21	42,60	16,57	0,83
Mn_2B	1853[47]	tetragonal	5,15	4,21	42,66	16,62	0,87
Cr_2B	1823[49]	tetragonal	5,18	4,31	43,49	19,39	1,46
AlB_{12}	2173[50]	tetragonal	10,28	14,3	184,76	296,12	0,68

Tab. 4-3: Crystallographic structure, lattice dimension and lattice disregistry of the most suitable carbides.

compound	melting point [K]	crystallographic structure	lattice dimension [Å]		misfit [%]			rotation of planes, misfit [%]
			a	c	(001)	(100)	(0001)	(001)
$Y_3C^{(+)}$	2673[48]	cubic	5,13	-	42,02	-	-	0,42
$Cr_{23}C_6$	1793[46]	cubic	10,64	-	194,74	-	-	4,21
$Mn_{23}C_6$	1793[50]	cubic	10,59	-	107,43	-	-	3,72
YC_2	2673[48]	tetragonal	3,66	6,17	1,50	70,89	-	-
$Ni_3C^{(*)}$	-	hcp	2,63	4,31	-	-	2,95	-

Tab. 4-4: Crystallographic structure, lattice dimension and lattice disregistry of the most suitable nitrides.

compound	melting point [K]	crystallographic structure	lattice dimension [Å]		misfit [%]			rotation of planes, misfit [%]
			a	c	(001)	(100)	(0001)	(001)
$Ni_4N^{(*)}$	-	cubic	3,72	-	3,05	-	-	-
$Co_4N^{(*)}$	-	cubic	3,74	-	3,55	-	-	-
YN	2843[51]	cubic	4,88	-	35,10	-	-	-4,47
Zn_3N_2	600[52]	cubic	9,76	-	170,44	-	-	-4,38
Mg_3N_2	800[53]	cubic	9,95	-	175,62	-	-	-2,55
$Ti_2N^{(+)}$	3218[47]	tetragonal	4,94	3,04	36,92	-15,91	-	-3,18
$Ni_3N^{(*)}$	-	hcp	2,67	4,31	-	-	4,31	-
$Co_3N^{(*)}$	-	hcp	2,66	4,35	-	-	4,21	-
BN	3243[46]	hcp	2,5	6,66	-	-	-2,07	-
$Fe_4N^{(*)}$	-	hcp	2,66	4,34	-	-	4,21	-

Tab. 4-5: Crystallographic structure, lattice dimension and lattice disregistry of the most suitable sulphides.

compound	melting point [K]	crystallographic structure	lattice dimension [Å]		misfit [%]		rotation of planes, misfit [%]
			a	c	(001)	(100)	(001)
MgS	2300[47]	cubic	5,19	-	43,77	-	1,66
MnS	1803[47]	cubic	5,21	-	44,32	-	2,05
Co_9S_8	-	cubic	9,91	-	174,52	-	-2,94

Tab. 4-6: Crystallographic structure, lattice dimension and lattice disregistry of the most suitable oxides.

compound	melting point [K]	crystallographic structure	lattice dimension [Å]		misfit [%]		rotation of planes, misfit [%]
			a	c	(001)	(100)	(001)
ZnO_2	423[48]	cubic	4,87	-	34,93	-	-4,59
ZrO_2	2950[47]	cubic	5,10	-	41,27	-	-0,10
SrO	2938[47]	cubic	5,14	-	42,37	-	0,67
Bi_2O_3	1098[46]	cubic	10,25	-	183,80	16,62	0,34
Y_2O_3	2270[47]	cubic	10,60	-	193,69	19,39	3,83
WO_2	1773[54]	cubic	4,87	-	34,9	-	-4,61
WO_3	1746[55]	tetragonal	5,27	3,93	46,04	8,84	3,27
SrO_2	488[48]	tetragonal	5,03	6,56	39,34	81,72	-1,48
MoO_2	1373[48]	tetragonal	4,87	2,80	34,90	-22,55	-4,61
MnO_2	803[47]	tetragonal	9,82	2,85	171,88	-21,14	-3,87
TiO_2	2130[47]	tetragonal	3,79	9,51	4,85	163,55	-

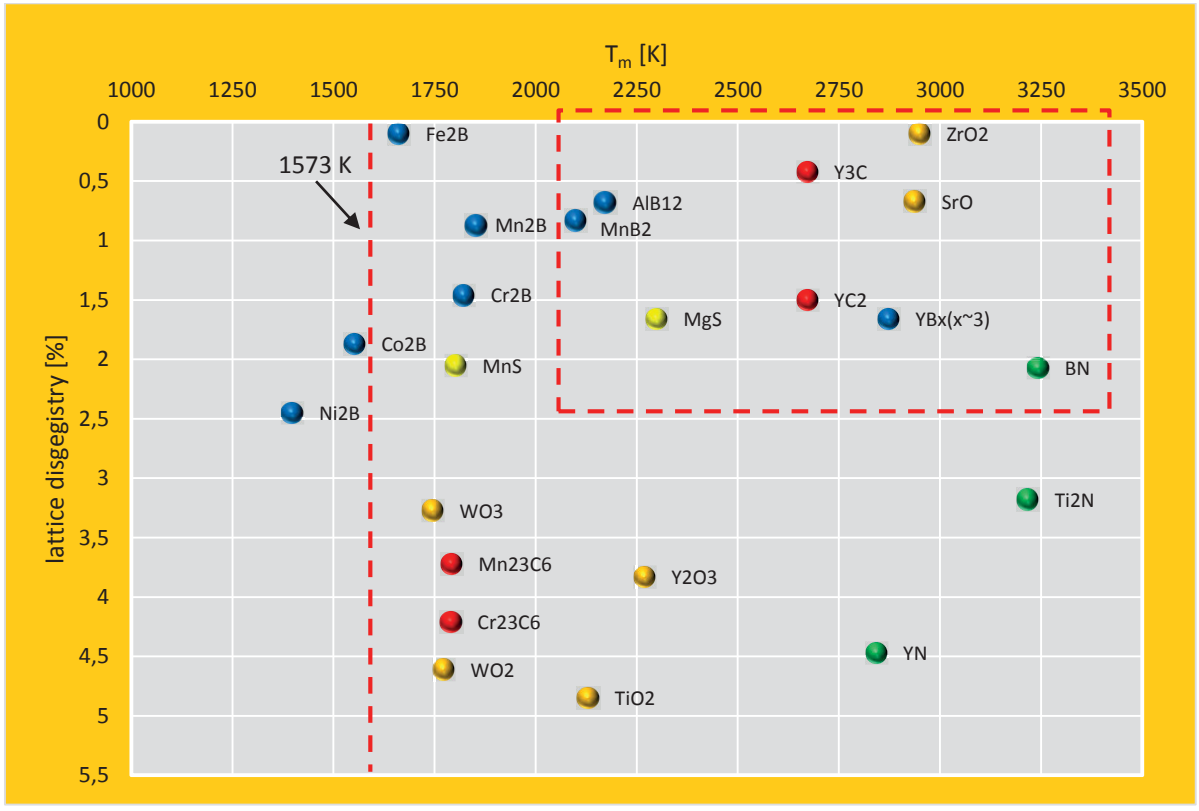

Fig. 4-1: Lattice disregistry and melting point of suitable binary compounds.

4.3 Grain refinement of pure copper with tin

The effect of tin on the grain size of high purity copper added as pure tin is shown in **Fig. 4-2**. The grain size shows a remarkably increase at addition levels of 0,5 wt% tin, respectively at a Q-value of 2,9 K. A further increase in the tin content up to 1,5 wt% tin (8,7 K) has no influence on the grain size, whereas a tin content of 2 wt% (11,6 K) and 5 wt% (28,9 K) show a slightly decrease in the grain size compared to lower additions (0,5 to 1,5 wt%). The micrographs of the copper-tin TP-1 cast samples at pouring temperatures of 1150°C +/- 10°C are shown in **Fig. 4-3**. The error bar at 28,9 K represents the sample where the grain size could not be determined by linear intercept method.

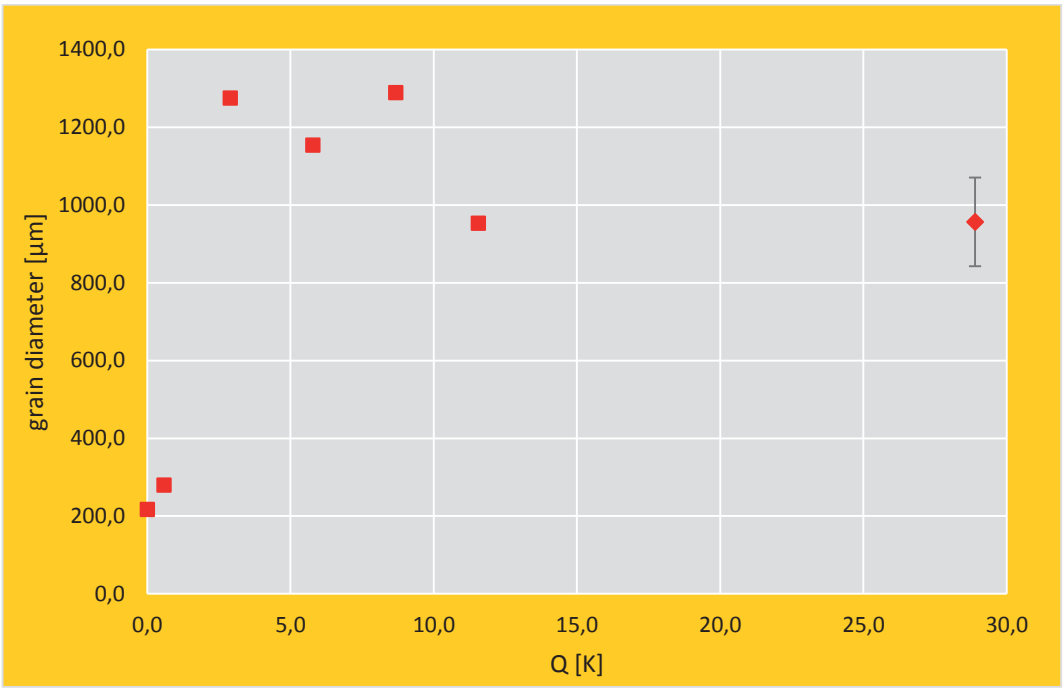

Fig. 4-2: Effect of tin on the grain size of pure copper, TP-1 cast samples, 1150°C +/- 10°C pouring temperature.

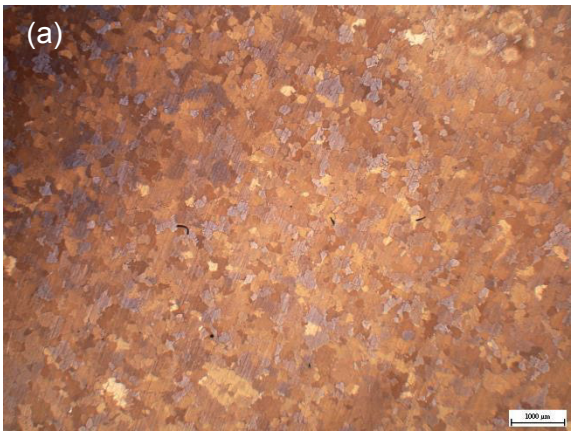

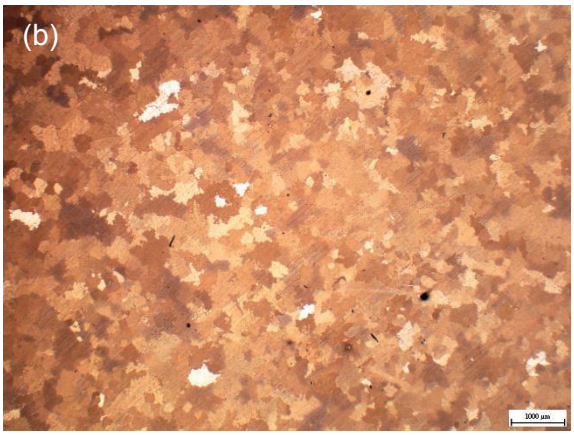

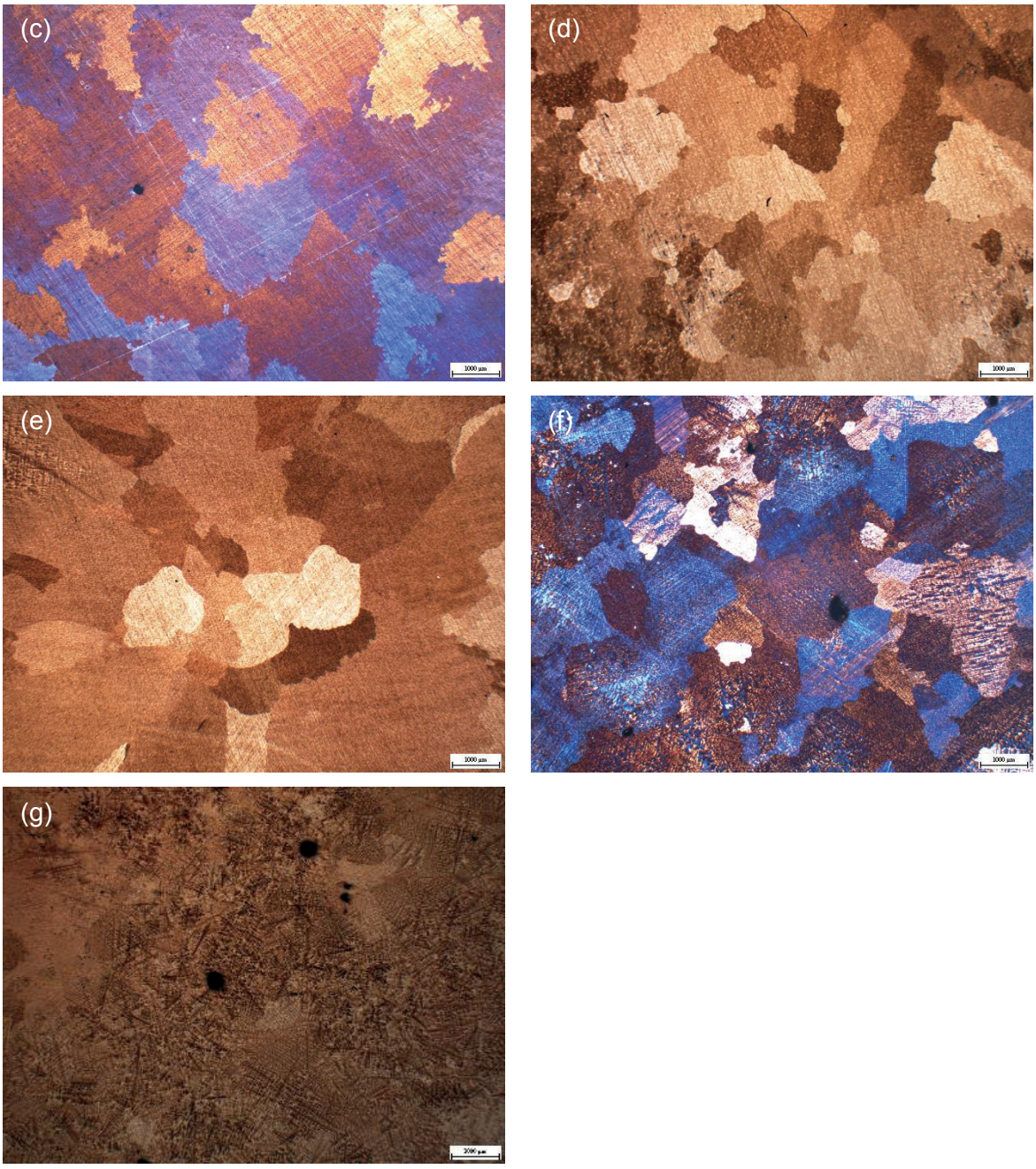

Fig. 4-3: Micrographs of the copper-tin TP-1 cast samples, poured at 1150°C +/- 10°C: (a) 0 wt% tin, (b) 0,1 wt% tin, (c) 0,5 wt% tin, (d) 1,0 wt% tin, (e) 1,5 wt% tin, (f) 2 wt% tin, (g) 5 wt% tin.

4.4 Grain refinement of pure copper with zinc

The effect of zinc on the grain size of high purity copper added as pure zinc is shown in **Fig. 4-4**. The results show a similar effect of zinc on the grain size of pure copper compared to tin. The grain size shows an increase at addition levels of 0,5 wt% zinc, respectively at a Q-value of 0,8 K. A further increase in the zinc content up to 2 wt% zinc (3,1 K) shows no influence on the grain size. The micrographs of the copper-zinc TP-1 cast samples at pouring temperatures of 1150°C +/- 10°C are shown in **Fig. 4-5**.

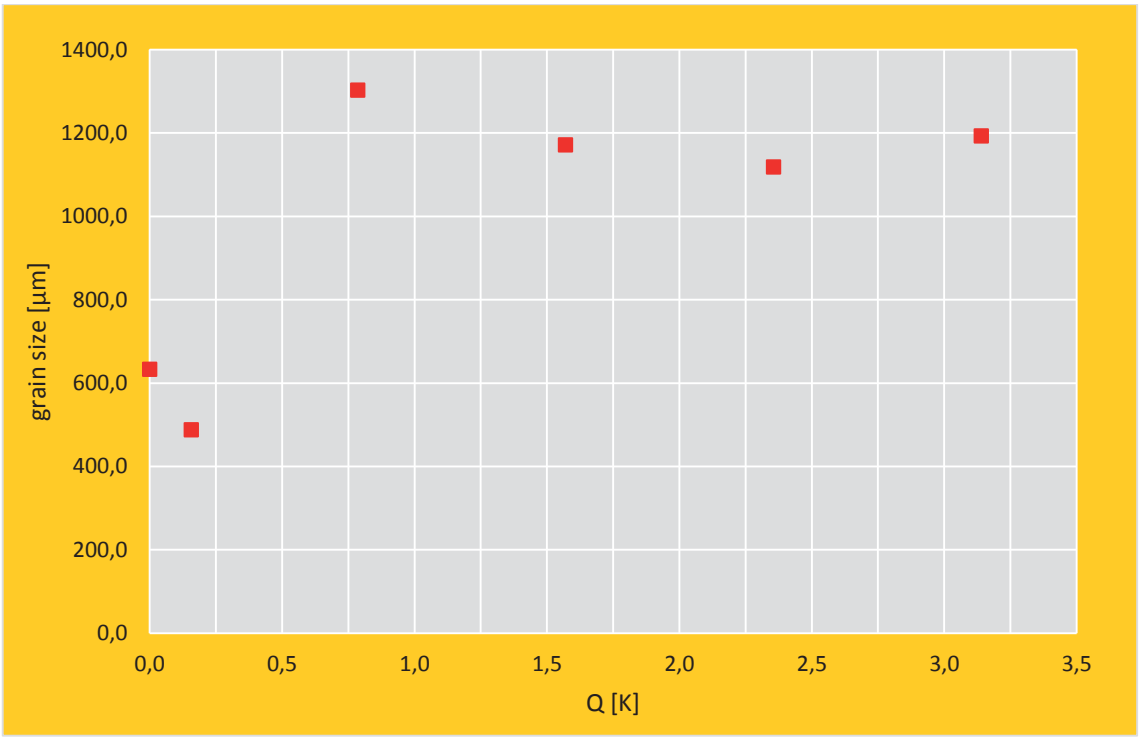

Fig. 4-4: Effect of zinc on the grain size of pure copper, TP-1 cast samples, 1150°C +/- 10°C pouring temperature.

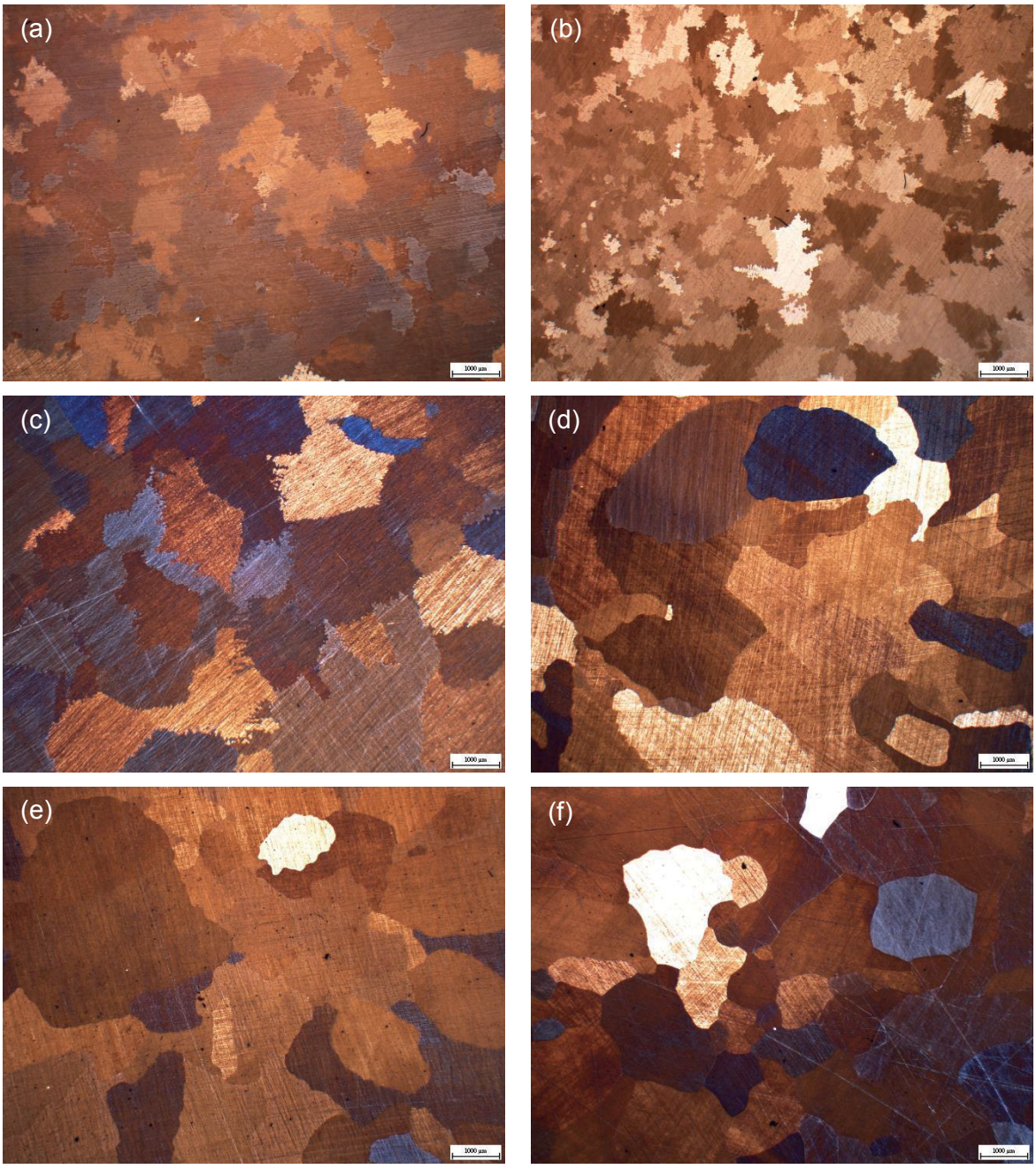

Fig. 4-5: Micrographs of the copper-zinc TP-1 cast samples, poured at 1150°C +/- 10°C: (a) 0 wt% zinc, (b) 0,1 wt% zinc, (c) 0,5 wt% zinc, (d) 1,0 wt% zinc, (e) 1,5 wt% zinc, (f) 2 wt% tin, (g) 5 wt% tin.

4.5 Grain refinement of pure copper with phosphorus

The effect of phosphorus on the grain size of high purity copper added as Cu-15P master alloy is shown in **Fig. 4-6**. The results show a slightly decrease of the grain size from 543,3 µm to 509 µm at an addition level of 630 ppm phosphorus (2 K). The micrographs of the copper-phosphorous TP-1 cast samples at pouring temperatures of 1150°C +/- 10°C are shown in **Fig. 4-7**. The error bars at 4 and 8 K represent the samples where the grain size could not be determined by linear intercept method.

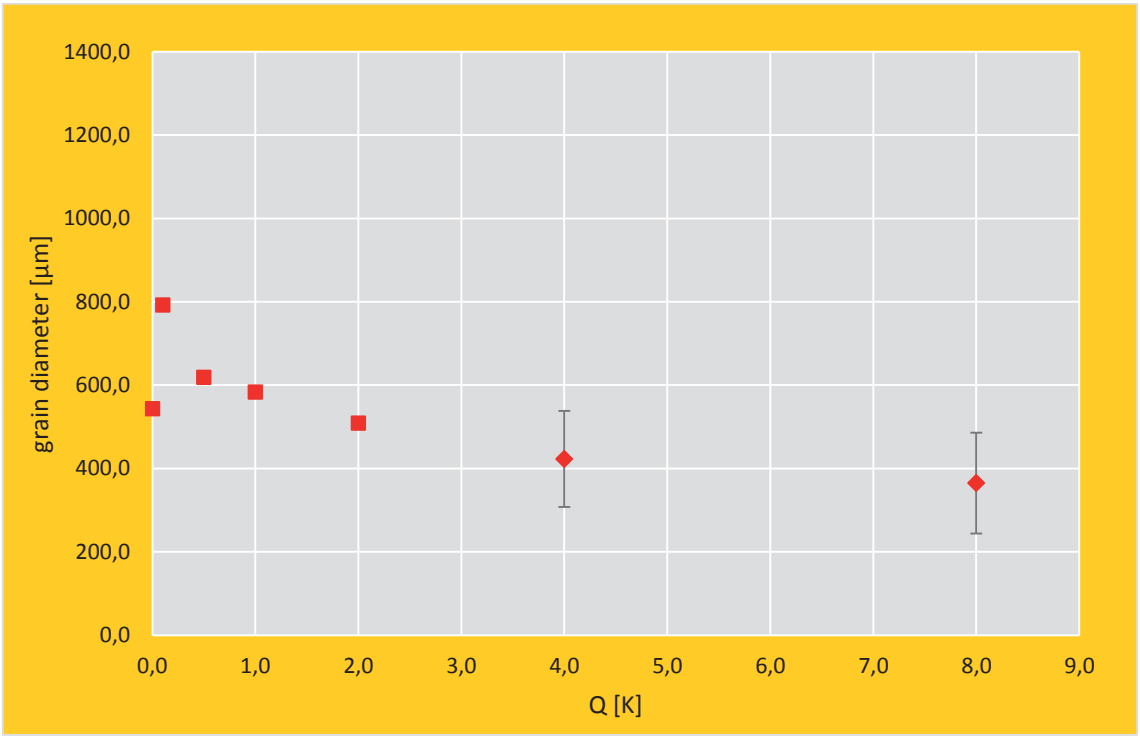

Fig. 4-6: Effect of phosphorus on the grain size of pure copper, TP-1 cast samples 1150°C +/- 10°C pouring temperature.

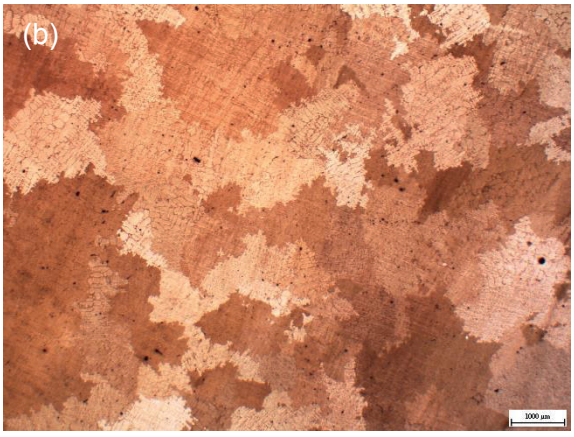

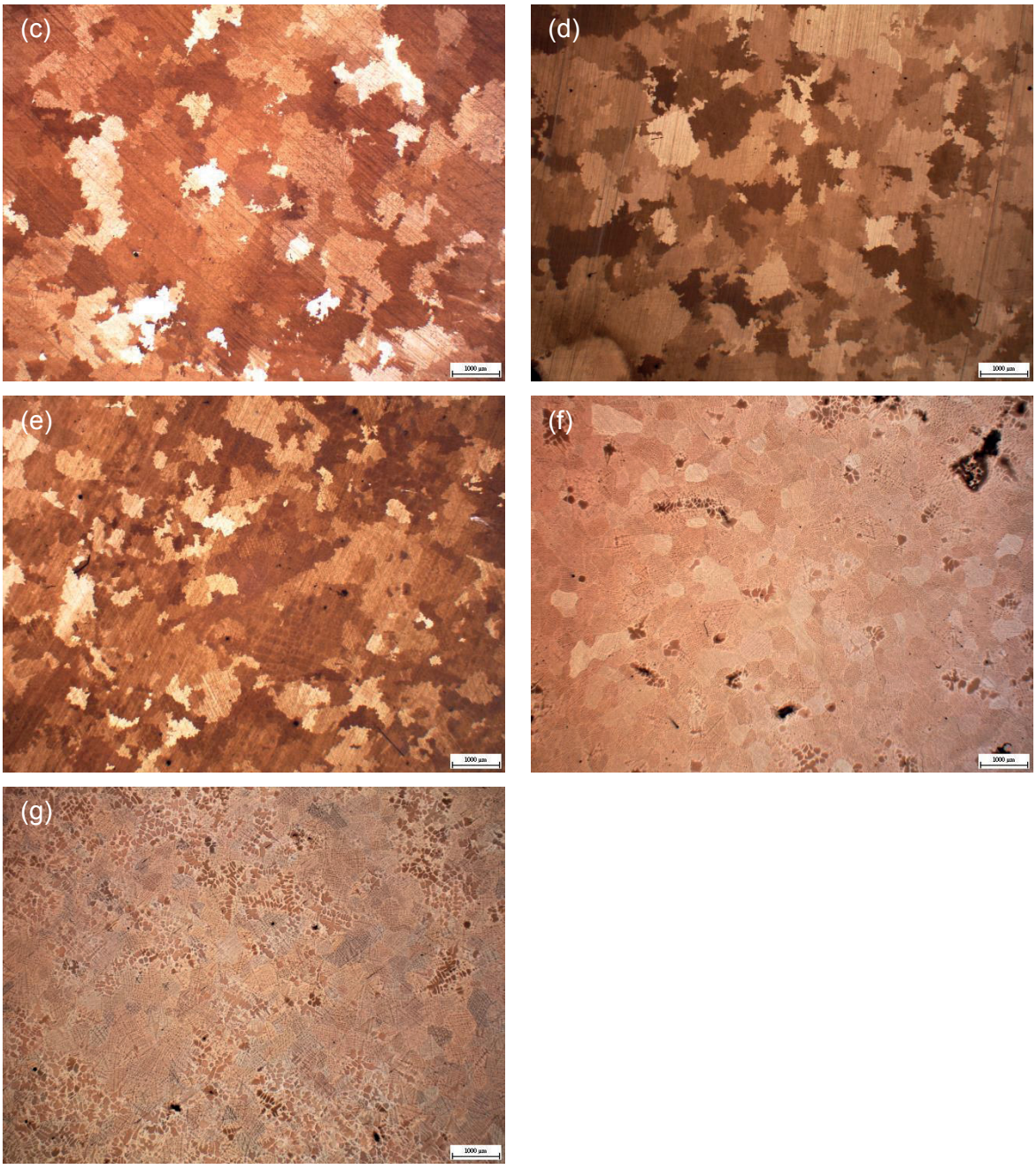

Fig. 4-7: Micrographs of the copper-phosphorus TP-1 cast samples, poured at 1150°C +/- 10°C: (a) 0 wt% phosphorus, (b) 30 ppm phosphorus, (c) 160 ppm phosphorus, (d) 310 ppm phosphorus, (e) 630 ppm phosphorus, (f) 0,125 wt% phosphorus, (g) 0,251 wt% phosphorus.

4.6 Grain refinement of pure copper with magnesium

The effect of magnesium on the grain size of high purity copper added as Cu-50Mg master alloy is shown in **Fig. 4-8**. The addition of magnesium up to contents of 0,18 wt%, respectively 4 K, shows no significant effect on the grain size, whereas the addition of 0,36 wt% (8 K) remarkably increases the grain size of approximately 400 µm. The micrographs of the copper-magnesium TP-1 cast samples at pouring temperatures of 1150°C +/- 10°C are shown in **Fig. 4-9**.

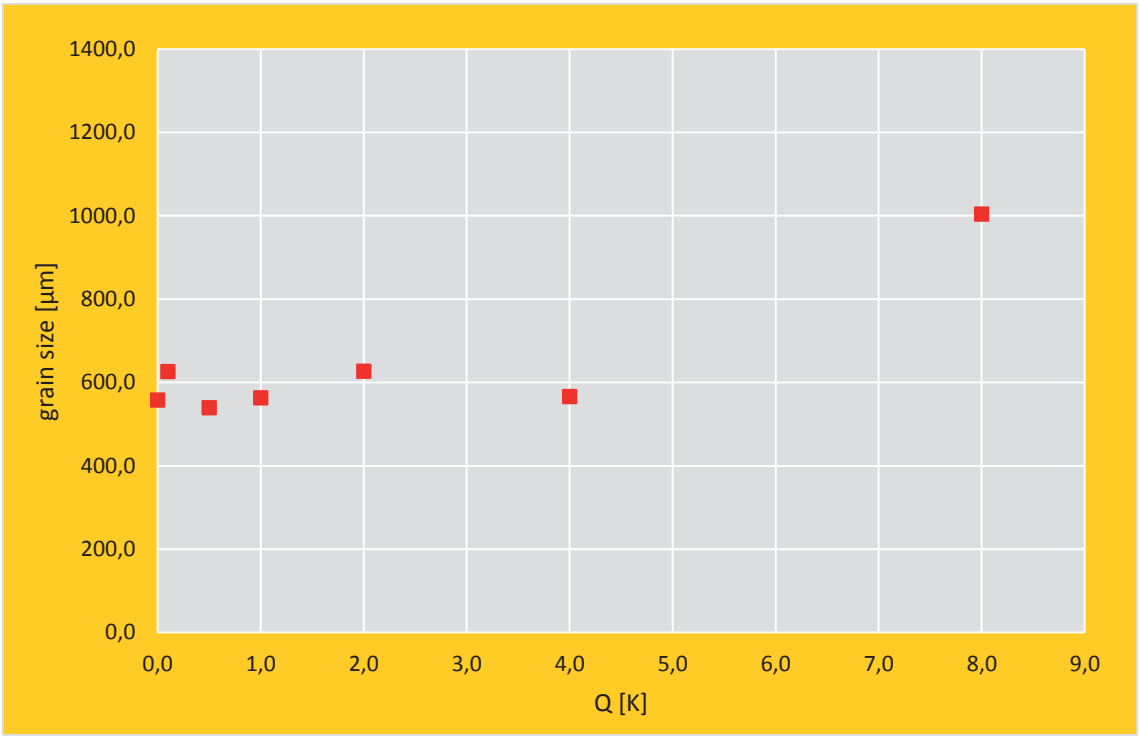

Fig. 4-8: Effect of magnesium on the grain size of pure copper, TP-1 cast samples, 1150°C +/- 10°C pouring temperature.

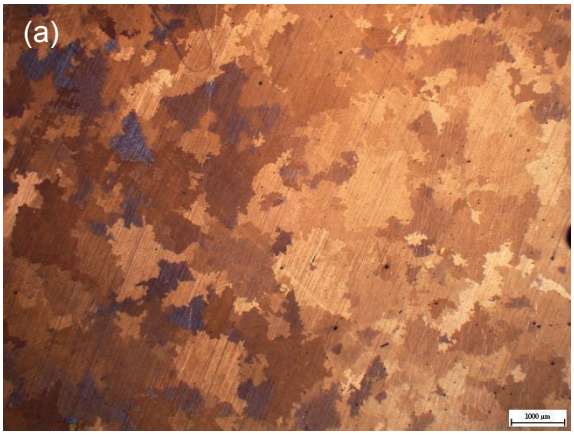

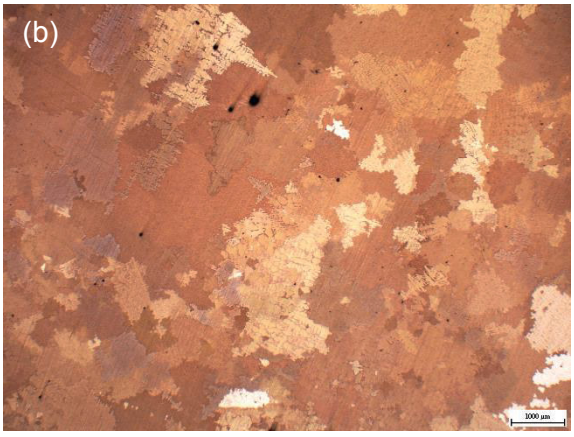

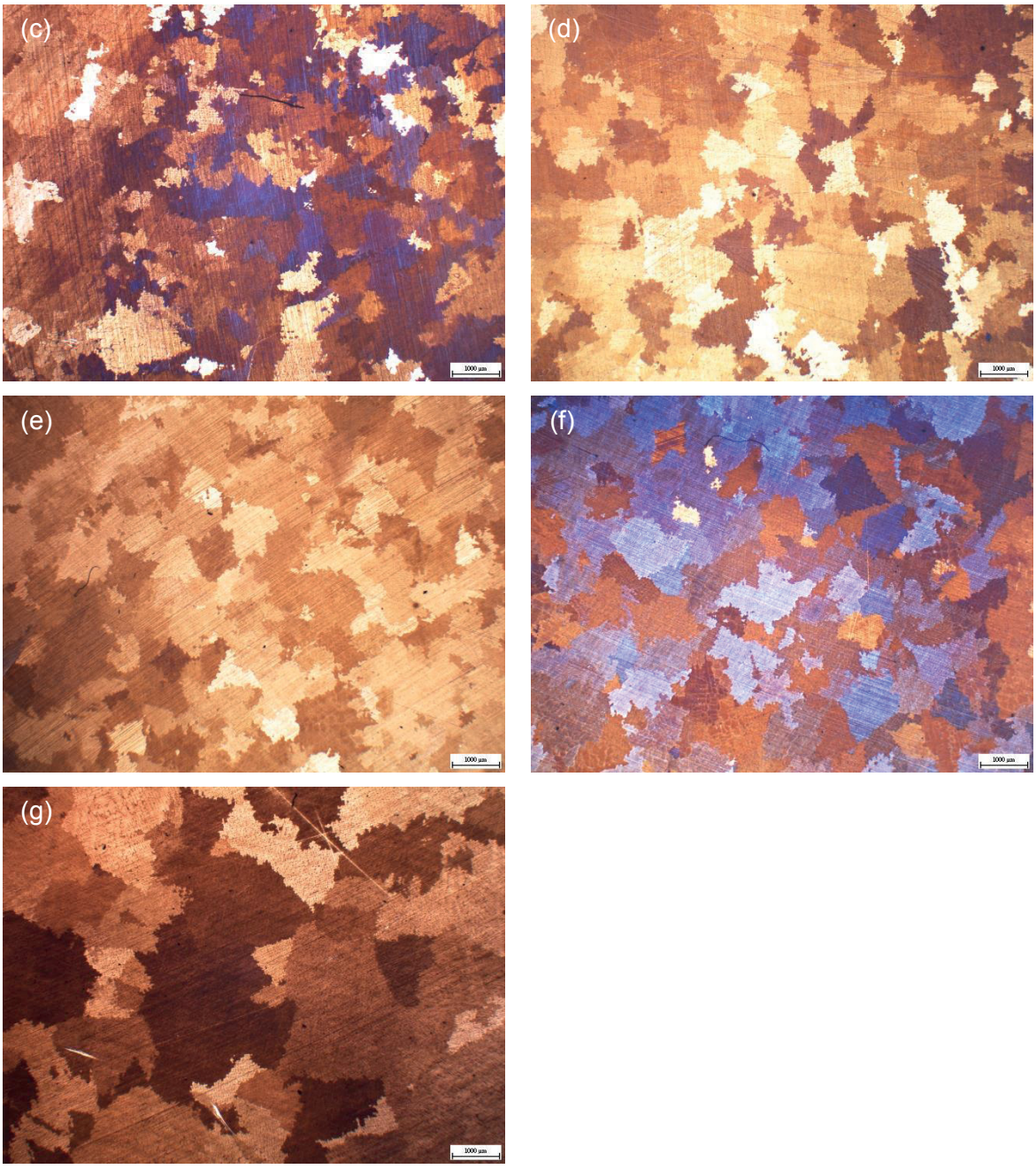

Fig. 4-9: Micrographs of the copper-magnesium TP-1 cast samples, poured at 1150°C +/- 10°C: (a) 0 wt% magnesium, (b) 40 ppm magnesium, (c) 220 ppm magnesium, (d) 450 ppm magnesium, (e) 900 ppm magnesium, (f) 0,18 wt% magnesium, (g) 0,36 wt% magnesium.

4.7 Grain refinement of pure copper with iron

The effect of iron on the grain size of high purity copper added as Cu-25Fe master alloy is shown in **Fig. 4-10**. Addition levels of iron up to 0,175 wt%, respectively 2 K, show no significant effect on the grain size of pure copper. At a content of 0,351 wt% iron the grain size remarkably increases similar to magnesium of approximately 400 µm. No further change in the grain size is shown at an addition level of 0,701 wt% (8 K). The micrographs of the copper-iron TP-1 cast samples at pouring temperatures of 1150°C +/- 10°C are shown in **Fig. 4-11**.

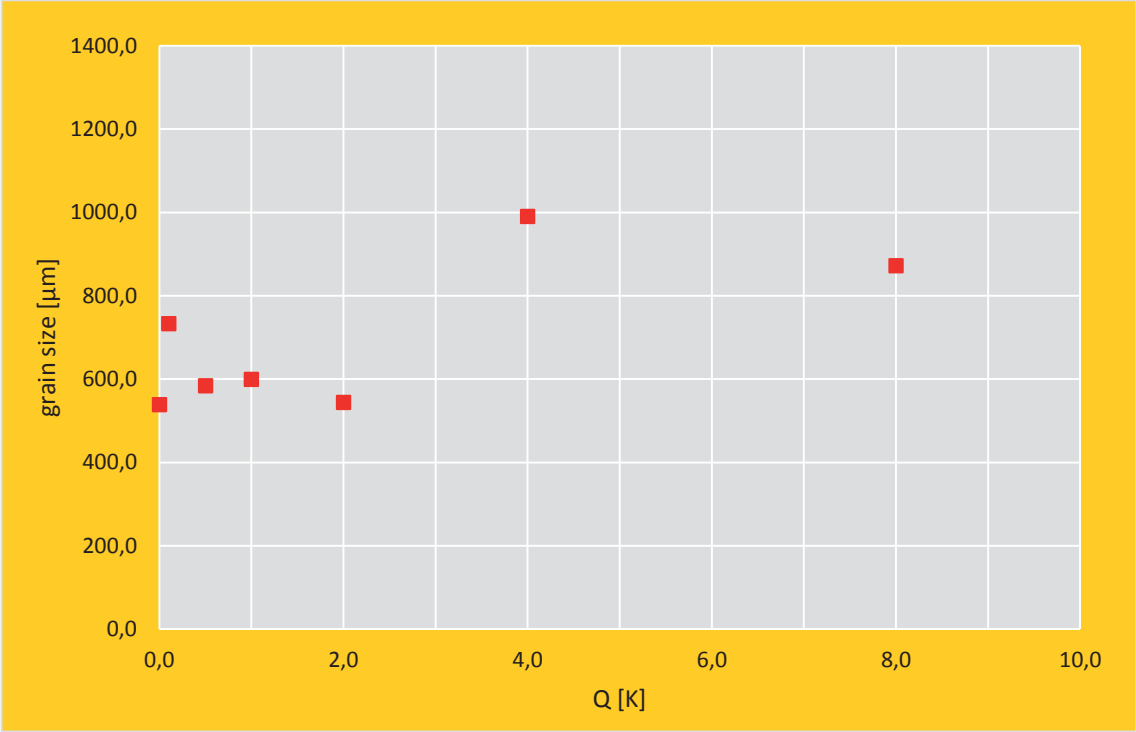

Fig. 4-10: Effect of iron on the grain size of pure copper, TP-1 cast samples, 1150°C +/- 10°C pouring temperature.

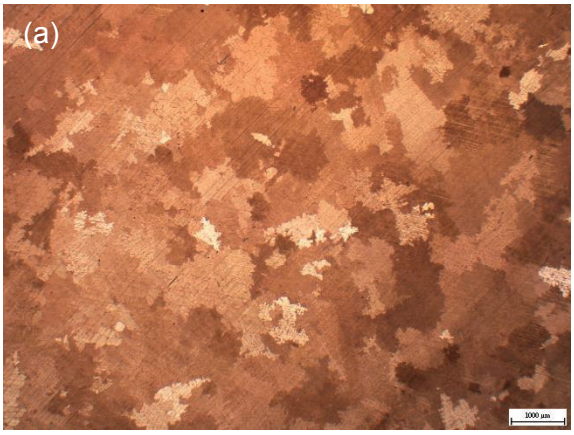

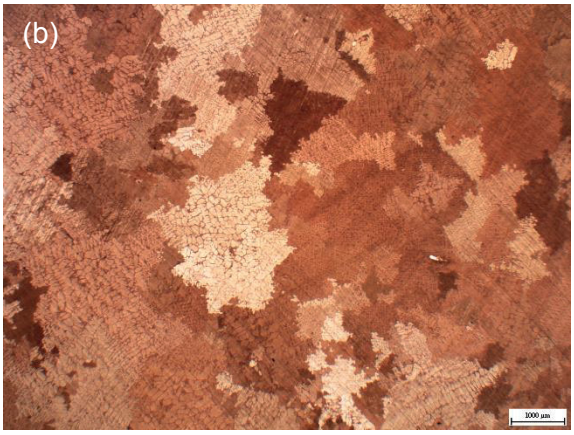

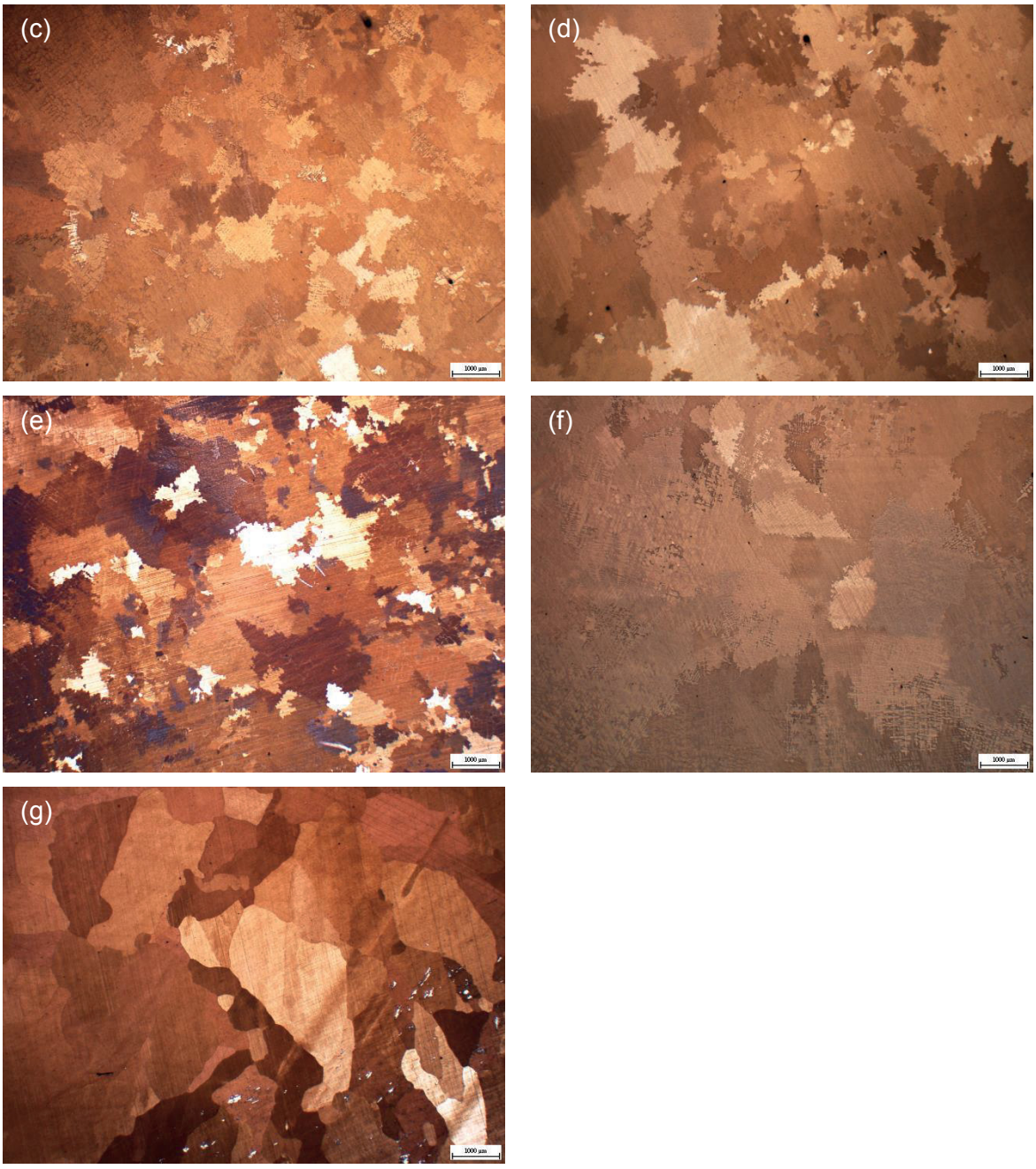

Fig. 4-11: Micrographs of the copper-iron TP-1 cast samples, poured at 1150°C +/- 10°C: (a) 0 wt% iron, (b) 90 ppm iron, (c) 440 ppm iron, (d) 880 ppm iron, (e) 0,175 wt% iron, (f) 0,351 wt% iron, (g) 0,701 wt% iron.

5 Discussion

The results of chapter **4** are discussed with respect to Q, suitable nucleants and the variation of grain size of high purity copper by the addition of tin, zinc, phosphorus, magnesium and iron.

5.1 Growth restriction factor

Q is the parameter that describes the influence of the alloying elements on the grain size that promote undercooling and nucleation by providing a larger constitutional undercooling for more particles to become active and by growth restriction due to a lower growth velocity and therefore less latent heat release the higher the Q is [56,57]. In aluminium alloys titanium is the most powerful segregant with a Q of 245,6 K/wt% , followed by tantalum with a Q of 105 K/wt%, vanadium with a Q of 30 K/wt% and hafnium with a Q of 11,2 K/wt%. All the other elements show a Q below 10 K/wt% [58]. In magnesium alloys iron is the most powerful segregant with a Q of 52,56 K/wt% [59]. As iron has negative influence on the corrosion resistance of magnesium, iron is neglected as a grain refiner in magnesium alloys. Further elements with a high Q are zirconium with a Q of 38,29 K/wt% and calcium with a Q of 11,94 K/wt%. Compared to aluminium and magnesium none of the alloying elements of the copper system shows a significant high Q as titanium and tantalum for aluminium or iron for magnesium. Nevertheless, two alloying elements, phosphorus and beryllium, show a Q above 30 K/wt%, six alloying elements show a Q above 20 K/wt% and several alloying elements show a Q between 10 and 20 K/wt%. Phosphorus, as the common deoxidation reagent [60], is the most powerful segregant for copper alloys. A residual phosphorus content after deoxidation of usually 0,015 to 0,04 wt% [36,60] would result in a Q of 0,5 to 1,3 K. Further powerful segregants with a Q above 20 K/wt% in copper are mainly high oxygen affine elements [43], e.g. lithium, magnesium, yttrium and calcium. Therefore, deoxidation reactions and alloy loss (dross) have to be considered. The main alloying elements tin and zinc [61] show low Q values and can be found at the end of **Tab. 4-1**, similar to further important alloying elements, e.g. aluminium and lead. Nickel, as it can be found in additions of 30 wt% in copper alloys [60], is the only main alloying element with a relative high Q of 17,46 K/wt% in addition to beryllium, however, the health hazards of beryllium [62] have to be considered.

5.2 Nucleation sites

As grain refinement depends on nucleation and growth restriction [16] suitable nucleants for copper alloys were selected under consideration of their lattice disregistry to the copper lattice. A comprehensive list of the observed particles is given in **7.9** in the **Appendix**. The boundary in the lattice disregistry was defined at 5 % [44]. As the majority of the observed compounds has a lattice disregistry greater than 5 %, the rotation of crystallographic planes according to [34] was taken under consideration. Due to the fact that a great number of particles have a lattice dimension in the range of 5, respectively 10 Å, the rotation of crystallographic planes enables further particles to act as nucleants in copper alloys. As the majority of the compounds with a lattice disregistry less than 5 % are ternary compounds, rare earth compounds or radioactive and toxic compounds, the focus was on binary compounds, presented in **4.2**. In addition to a small lattice disregistry, potent nucleating particles should have a high melting point and a high thermodynamic stability [3,59]. Considering the melting point and the lattice disregistry, SrO, ZrO_2, BN, Y_3C/YC_2, MnB_2, AlB_{12} and MgS seem to be the most suitable binary compounds. As some of the elements form several carbides, borides, etc., the thermodynamic stability has to be subjected to a more detailed examination, considering reliable Richardson-Ellingham-diagrams (RED) and furthermore ternary phase diagrams. As many of the components of the borides, carbides, nitrides and sulphides form stable oxides [43], a deoxidation of the melt would be necessary before adding the grain refiner.

5.3 Grain refinement of high purity copper by the addition of alloying elements

As the purpose of the work was to investigate the effect of the addition of several alloying elements on the grain size of high purity copper, five elements with varying Q were added to high purity copper (99,995 wt%) based on the list of calculated Q values in **4.1**. As the main alloying elements of copper, tin and zinc [60] were chosen and added in amounts of 0,1 to 5 wt%, respectively in amounts of 0,1 to 2 wt% to determine the effect of higher amounts of added solute and therefore higher Q values up to 28,9 K. As tin and zinc with a Q of 5,8 K/wt%, respectively 1,6 K/wt%, can be found at the end of **Tab. 4-1** in **4.1**, three further alloying elements with higher Q values were chosen with regard to their importance as an alloying element in copper alloys, regarding further aspects as health hazards, e.g beryllium [62], and costs, e.g yttrium. Iron shows a Q of 11,4 K/wt%, magnesium, a common deoxidation reagent [60], a Q of 22,2 K/wt%. Phosphorus, as it can be found at the upper end of the list, shows the highest Q of 31,9 K/wt%. As all the alloying elements, primarily

magnesium and in particular phosphorus as the common deoxidation reagent [61], show a high affinity to oxygen [43], deoxidation reactions and therefore alloy loss have to be considered in despite of the use of an inert gas coverage.

As grain refinement of alloys depends on nucleation, the cooling rate and the solute level of the added alloying elements [4,16], the aim of the present study was to understand the influence of soluble solutes on the grain size of high purity copper, disregarding the effect of the addition of nucleating particles, while maintaining the cooling rate constant in first instance by using the TP-1 test device, mentioned in **3.3**. The TP-1 test device was invented to determine the grain size of aluminium alloys [59], simulating the cooling rate in the middle of a continuously cast billet with a diameter of 180 mm. However, there has been not much practical work on the grain refinement of copper alloys under defined cooling conditions as given by the TP-1 test. As the TP-1 test provides a constant cooling rate of 3,5 K/s for aluminium alloys at the central region of a cross-section [63] at 38 mm from the base of the TP-1 sample [36], and a cooling rate of 4 K/s was simulated and measured for pure magnesium [59], a cooling rate of approximately 3,5 to 4 K/s can be estimated for copper alloys.

5.3.1 Variation of the grain size by the addition of tin, zinc, phosphorus, magnesium and iron

The change in grain size with the addition of tin, zinc, phosphorus, magnesium and iron of high purity copper is shown in **Fig. 4-2** to **Fig. 4-10**. Disregarding alloy loss through deoxidation reactions the grain size shows a remarkably increase at addition levels of 0,5 wt% tin, respectively despite a Q of 2,9 K. A further increase in the tin content up to 1,5 wt% tin (8,7 K) has no influence on the grain size, whereas tin contents of 2 wt% (11,6 K), respectively 5 wt% (28,9 K) show a slightly decrease in the grain size compared to lower additions (0,5 to 1,5 wt%). As the average grain size of the unalloyed high purity copper was 568 µm, disregarding the value of the tin series, the remarkably low level of the grain size of the unalloyed sample of the tin series and the grain size of the sample with 0,1 wt% tin can be explained by an already contaminated used crucible. Uncontrollable effects of the in preliminary tests used copper wire scrap and wear of the zirconia silicate coating and therefore influences of the graphite crucible may led to the severe decrease in grain size at the beginning of the series. Nevertheless, assuming an average grain size of 568 µm, a significant increase in grain size is shown in **Fig. 4-2**. Compared to tin, similar effects of zinc on the grain size are shown in **Fig. 4-4**. The grain size shows an increase at addition levels of 0,5 wt% zinc, respectively at a Q of 0,8 K. A further increase in the zinc content up to 2 wt% zinc (3,1 K) shows no influence on the grain size. Similar trends of the grain size were

found for magnesium and iron, shown in **Fig. 4-8** and **Fig. 4-10**. The addition of magnesium up to contents of 0,18 wt%, respectively 4 K, has no significant effect on the grain size, whereas the addition of 0,36 wt% (8 K) remarkably increases the grain size. Addition levels of iron up to 0,175 wt%, respectively 2 K, show no significant effect on the grain size. At a content of 0,351 wt% iron the grain size remarkably increases similar to magnesium. As the only solute, phosphorus results in a decrease in grain size up to addition levels of 0,25 wt% (8 K).

5.3.2 Experimental studies of the effect of alloying elements on the grain size of high purity copper and high purity aluminium

Comprehensive work on the influence of solutes on the grain size of copper was carried out by Bustos [64]. The effect of addition levels of 0,1 wt% of 34 elements was investigated. The melting experiments were carried out in a vacuum induction furnace, using graphite crucibles under argon atmosphere. The melt was poured in graphite ladles, respectively water cooled copper ladles, whereas the samples had a diameter of 30 mm and a high of 35 mm. At a casting temperature of 1160°C poured into a water cooled copper ladle, the grain size of the unalloyed high purity copper (99,99 wt%) showed a grain size of 650 µm, similar to the grain size shown in this work. The variation in grain size by the addition of several alloying elements at concentrations of 0,1 wt% is shown in **Tab. 7-2** in the **Appendix**. Contradictory results were found between the grain size of the samples poured in graphite ladles and in water cooled copper ladles. Whereas the grain size of the samples poured in copper ladles varied strongly from element to element, the grain size of the samples poured in graphite ladles showed a decrease for the majority of the examined elements, except aluminium, silicon, calcium and chromium. Further work on the effect of the single addition of alloying elements on high purity copper was carried out by Balart et al. [65]. Under defined cooling conditions given by the TP-1 test, poured at 1150°C, columnar to equiaxed transition (CET) was observed by the single addition of 0,5 wt% boron and 0,1 wt% phosphorus. Magnesium, calcium and zirconium in additions of 0,085 wt% as well as titanium in additions of 0,4 wt% had no influence on the grain size. An increase in grain size was found for boron in additions of 0,085 - 0,17 wt% as well as for magnesium and calcium (0,4 wt%) and phosphorus (0,5 wt%).

Considering the variation of the grain size observed in this work and the results of Bustos [64] and Balart et al. [65], contradictory results were observed compared to the work carried out by Spittle and Sadli [26] for high purity aluminium. Comprehensive work on the influence of various solutes including chromium, copper, iron, magnesium, manganese, silicon, tin, zinc and zirconium on the grain size of high purity aluminium (99,99 wt%) was carried out

by Spittle and Sadli [26] under defined cooling conditions given by the TP-1 test shown in **Fig. 7-4** and **Tab. 7-1** in the **Appendix**. Without the addition of grain refiner, the grain size shows a remarkably decrease with increasing amount of solute. Although the grain size was plotted versus the supercooling parameter P, the decreasing of the grain size to a plateau value can be estimated at a Q of above 5 K.

5.3.3 Increase in grain size with alloy addition in other alloy systems

It has been reported that the grain size in aluminium-silicon alloys [66,67,68] as well as in lead-antimony alloys [66] first decreases with increasing solute content, respectively increasing Q, and then increases after reaching a minimum with increasing solute content. Doppelhofer [69] reported a slightly increase in grain size up to the transition point found by other researchers [66,67,68] and a remarkably increase beyond the transition point under defined cooling conditions given by the TP-1 test at casting temperatures of 720°C shown in **Fig. 7-3** in the **Appendix**. Johnsson [67] and Johnsson and Bäckerud [68] investigated the influence of increasing silicon content in the aluminium-silicon-titanium and the aluminium-silicon-iron-titanium system grain refined with an aluminium-titanium-boron master alloy at pouring temperatures of 775°C and cooling rates of 1 K/s shown in **Fig. 7-1** in the **Appendix**. It was reported that the grain size first decreases, reaching a minimum and then increases with increasing silicon content beyond a Q of approximately 20 K. It was found that two different growth models have to be considered. In the low alloy region with Q below 20 K cellular crystals were observed, leading to a solute build-up ahead of the cellular interface. As the solute content was increased, dendrites with orthogonal branches were observed, forming lancet-like tips, developing a side-wise diffusion profile, increasing the growth rate and the grain size. As grain refined alloys were investigated by Johnsson and Bäckerud [68], other mechanisms have to be considered, primarily silicon interaction with titanium [66]. Furthermore, it was observed, that an increase of zinc in the aluminium-zinc system up to a Q of 50 K didn't show a transition in grain size as it has been found for aluminium-silicon alloys [58]. It is supposed that this may be related to the large solid solubility of zinc in the aluminium-zinc system [66]. However, further explanation for the increase in grain size with increasing silicon level was given by Lee et al. [66] shown in **Fig. 7-2** in the **Appendix**. It was supposed that other factors may influence the grain size, e.g. a decreasing solidification range and increasing superheat and increasing latent heat with increasing silicon content. At casting temperatures of 800°C and cooling rates of 0,7 K/s the cellular-dendritic transition, described by Johnsson and Bäckerud [68], was observed, hence the differences were small. As the alloys in the low alloy region, as well as the alloys

in the high alloy region exhibited a dendritic morphology, the main differences was in the volume fraction of the eutectic and in finer dendrite arm spacing (DAS) and the differences in the morphology were supposed to be due to differences in the silicon content than due to differences in the growth morphology. Lee et al. [66] suggested that a change in the nucleant potency distribution due to a change of the constitutional profile as the silicon content increases is more likely and therefore fewer nucleants are activated. Furthermore, they suggested that silicon impedes the nucleation of aluminium by affecting the interface stability by changing the solid-liquid surface tension and the entropy of fusion. However, both mechanisms have to be subjected to a more detailed examination. Considering the work that has been carried out on the effect of silicon on the grain size of pure aluminium, several explanations have been given to describe the influence of silicon in aluminium alloys. However, it is not clear how these factors that have been given could cause to a transition at about 3 wt% silicon. Considering the results of Lee et al. [66] and Doppelhofer [69] for aluminium alloys and the work carried out by Bustos [64] for copper alloys, there seems to be a remarkably effect of the cooling rate on the grain size and in particular on the effect of the alloying element on the cooling rate and thereby grain size, which has to be examined in detail in future work.

5.3.4 Influence of cooling rate and Q on the grain size

Disregarding the addition of nucleating particles, the size of equiaxed grains depends on the alloy composition, respectively the Q, the convectional conditions and the thermal conditions and therefore the cooling rate [4,70]. Furthermore, the thermal conditions are influenced by the thermal conductivities of the solid and the liquid phase, the width of the mushy zone and the rate of latent heat release [1]. As columnar-to-equiaxed transition (CET) has been observed in this work in the centre of all samples without the addition of nucleating particles, the nucleation of equiaxed grains has to be considered in detail.

Several models of the CET have been proposed [71], e.g. heterogeneous nucleation, partial remelting of columnar dendrites. However, to promote nucleation the melt has to be sufficiently undercooled [4]. The difference between the growth of an equiaxed crystal in a pure metal and in an alloy has already been described in **2.2.2.1**, as shown in **Fig. 2-16**. In a pure metal, the thermal undercooling (ΔT_t) dominates [68]. During the equiaxed alloy growth, the solute build-up ahead of the dendritic tip results in a solute undercooling, respectively a constitutional undercooling and therefore the total undercooling ΔT is the sum of the thermal undercooling (ΔT_t) and the constitutional undercooling (ΔT_c), respectively the undercooling due to the curvature of the tip (ΔT_r) and the kinetic undercooling (ΔT_k). At low

cooling rates, assumed cooling rates of 1 K/s, ΔT_t and ΔT_r are small compared to ΔT_c [68] and are often neglected. In contrast, Men and Fan [56] proposed that ΔT_t increases with increasing cooling rate and that ΔT_c becomes negligible at higher cooling rates. For each cooling rate there is a maximum number of particles that can develop into new grains [68]. Increasing the cooling rate increases ΔT_t and therefore reduces the grain size by increasing the number of particles that become active and nucleate grains before recalescence occurs and nucleation is stopped due to latent heat release [13,56,72]. As already mentioned above, Q is the parameter that describes the influence of the alloying elements on the grain size that promotes undercooling and nucleation by providing a larger constitutional undercooling (ΔT_c) for more particles to become active and by growth restriction due to a lower growth velocity and therefore less latent heat release the higher the Q is [56,57]. Shu et al. [57] proposed that an increasing Q not only slows grain growth, but also widens the solute diffusion zone at the solid-liquid interface of a growing grain. Grain initiation occurs outside the diffusion zone, where the undercooling increases with increasing Q [56], whereas particles are solute suppressed within the diffusion zone, leading to a nucleation free zone (NFZ) [57,73]. By increasing the cooling rate, the thermal gradient in the liquid and the growth velocity increase, whereas the degree of ΔT_c decreases and therefore the NFZ becomes smaller [72,73]. Under consideration of the effects of cooling rate on ΔT_t, on the growth velocity and on the NFZ and the effect of Q on growth restriction and on ΔT_c, the final grain size can be understood as a complex interaction between the cooling rate and Q, whereas the influence of cooling rate has to be subjected to a more detailed examination.

5.3.5 Variation of thermal conductivity in aluminium and copper alloys and its influence on the cooling rate

Under defined cooling conditions as given by the TP-1 test with supposed cooling rates of 3,5 to 4 K/s, it can be assumed that the cooling rate is mainly influenced by the thermal conductivities of the liquid and the solid phase, more precisely by the columnar zone at the mould surface. The thermal conductivity λ_s of solid copper is influenced to a great extent by the alloying elements, respectively by the impurities. With the exception of silver, λ_s decreases by all alloying elements. According to [74], zinc has a minor influence on λ_s followed by increasing effect of nickel, tin, manganese, silicon and phosphorus. At 20°C high purity copper has a λ_s of 395 W/mK. A phosphorus content of 0,05 wt% decreases λ_s to a value of 293 W/mK [75]. Furthermore, a decrease of λ_s at low addition levels is shown in [76], e.g. CuZr0,1 – 360 W/mK, CuFe1P0,03 – 216 W/mK, CuSn1,25Fe0,75P0,03 – 173

W/mK, shown in **Tab. 7-5** in the **Appendix**. It is interestingly to note that copper shows a significant decrease of λ_s from pure copper to low alloyed alloys, which may lead to an insulating columnar zone. As it is difficult to obtain reliable values for λ_s of low alloyed binary aluminium and copper alloys close to the melting point, values for λ_s and the thermal conductivity of the liquid phase λ_l were obtained from [77] and extracted from MAGMA$^{5®}$ for commercial alloys, shown in **Tab. 7-3** and **Tab. 7-4** in the **Appendix**. It is shown that λ_l remains rather constant for aluminium alloys and for the copper-tin system, whereas λ_l shows a decrease in the copper-aluminium and the copper-zinc system. However, it is assumed that λ_s, more precisely λ_s of the columnar zone at the mold surface, is of greater influence on the cooling rate. Considering the variation of λ_s close to the melting point in aluminium alloys, λ_s remains rather constant in the aluminium-zinc system and the aluminium-copper system, whereas a decrease of λ_s is found for the aluminium-silicon system and the aluminium-magnesium system. Furthermore, the latent heat release decreases in the aluminium-zinc system and in the aluminium-copper system, remains constant the aluminium-magnesium system, but increases in the aluminium-silicon system. Comparing the variation of λ_s and latent heat with the variation in grain size, given by Spittle and Sadli [26] for various binary aluminium alloys and the variation in grain size in aluminium-silicon alloys, given by Lee et al. [66] and Doppelhofer [69], there seems to be a correlation between λ_s and latent heat release and therefore cooling rate, and the grain size. As mentioned above the grain size of aluminium alloys decreases with increasing amount of solute, reaching a plateau above a Q of about 5 K, as shown by Spittle and Sadli [26], carried out under constant cooling conditions given by the TP-1 test. As zinc was added in amounts up to 4,2 wt%, the grain size decreased with increasing Q, whereas λ_s remained nearly constant. Interestingly in contrast to aluminium-silicon alloys the latent heat decreased with increasing zinc content for commercial aluminium-zinc alloys. A similar variation in grain size was found for aluminium-copper alloys, whereas copper showed the greatest influence on decreasing grain size. The grain size for aluminium-magnesium alloys decreased with increasing amount of solute up to 1 wt%, but increased for amounts of 2 wt%. Considering the variation of λ_s for commercial aluminium-magnesium alloys, there is a remarkably decrease in λ_s between 1 and 3 wt% magnesium similar to aluminium-silicon alloys observed. Comparing the variation of the grain size given by Lee et al. [66] and Doppelhofer [69] with λ_s and the latent heat release of commercial aluminium-silicon alloys, it is apparent that λ_s shows a remarkably decrease for aluminium-silicon alloys with higher silicon content, whereas the latent heat increases with increasing silicon additions up to 12 wt% silicon.

5.3.6 Interaction of Q and cooling rate assumed for aluminium and copper alloys

Considering the variation of the grain size of aluminium-alloys with increasing solute content, compared to the variation of λ_s and the latent heat release, the following statements can be made:

(1) the influence of Q and therefore higher constitutional undercooling and growth restriction seems to be dominant in aluminium alloys up to a certain saturation level.

(2) in addition to the influence of Q, the variation in grain size with increasing solute content seems to be dependent on the variation of λ_s and the latent heat release of the alloy system.

(3) at high cooling rates, as given by the TP-1 test, thermal undercooling seems to be dominant for the grain size in aluminium-silicon alloys up to the transition point.

(4) the transition in grain size in the aluminium-silicon system seems to be affected by the increase in latent heat release and the heat flow over the columnar zone, influenced by decreasing λ_s with increasing silicon content. Additional affects on the efficiency of nucleating particles (silicon poisoning) in aluminium-silicon alloys may overlap within the transitional composition range for the increase in latent heat.

(5) at nominal high cooling rates, as given by the TP-1 test, the cooling rate within the equiaxed zone in aluminium-silicon alloys seems to be affected by the rapid formation and growth of an insulating columnar zone. Therefore, less nucleants become activated in the centre of the mould, resulting in a remarkably increase in grain size beyond the transition point.

(6) the transition in grain size in the aluminium-silicon system as well as the variation of the grain size in the other alloy systems seems to be of a complex interaction between the overall cooling rate and Q and its effect on constitutional undercooling and growth restriction and thereby latent heat release. The overall cooling rate appears to be affected to a great extent by the heat flow over the columnar zone (λ_s) and latent heat release, dominated by the concentration dependent latent heat release and by undercooling facilitated free growth. Therefore, the final grain size of the respective alloy system is dependent on which factor is dominant.

Considering the variation of the grain size in copper-systems by the work of Bustos [64] and the results obtained in this work, there seems to be a more sensitive mechanism referring to the influence of λ_s on the cooling rate in the equiaxed zone. It is difficult to obtain reliable values of λ_s for binary alloys, in particular at a very low alloy level. Known values for λ_s and latent heat [77,Magma$^{5®}$] are mainly for high alloyed copper alloys. As the grain size differs to a great extent from element to element at very low levels of the added solute, it is difficult to give a precisely correlation between Q and the variation of the cooling rate with decreasing λ_s and therefore the variation in grain size. However, the results given by Bustos [64] show that there is a great influence of the cooling rate on the grain size of low alloyed copper alloys, more precisely at nominal high cooling rates, the cooling rate within the equiaxed zone seems to be affected by the rapid formation and growth of an insulating columnar zone dependent on the alloying element. As discussed above, there is a remarkably decrease of λ_s with increasing solute content in copper alloys compared to aluminium alloys and according to [75,76] the decrease of λ_s seems to appear at very low levels of the added alloying elements. Considering the results given by Bustos [64] and the results obtained in this work, it can be hypothesized:

(1) λ_s of the columnar zone has a great influence on the cooling rate in copper alloys and therefore less nucleants become activated in the centre of the mould at very low alloy levels.

(2) at low cooling rates the influence of Q seems to be dominant on the grain size and the influence of λ_s on the cooling rate becomes negligible.

(3) at high cooling rates, the effect of decreasing λ_s on the cooling rate seems to be the dominant effect in increasing the grain size similar to the aluminium-silicon system discussed above. It can be assumed that at process predetermined high cooling rates, the cooling rate within the equiaxed zone seems to be affected by the rapid formation and growth of an insulating columnar zone dependent on the alloying element.

(4) in contrast to the aluminium alloys there seems to be a more sensitive range for the respective element at high cooling rates where the grain size varies in dependent on the alloy composition, Q, λ_s, the latent heat release and furthermore the cooling rate, influencing the distribution of activated nucleants in the centre of the casting.

As a result of the given interaction discussed above for aluminium and copper alloys a working model for an isothermal melt as described by Maxwell and Hellawell [78] can be made:

Assuming an isothermal melt model the degree of undercooling determines the activation of nucleants in the centre of the casting. ΔT of an isothermal melt can be understood as a balance of latent heat release and the heat flow over the columnar zone. Furthermore, the latent heat release is a function of the number of activated particles and growth restriction. The heat flow over the columnar zone is determined by λ_s dependent on the alloying element. Depending on the thermal conductivity of the columnar zone the heat flow can be become the limiting step to facilitate sufficient undercooling in the melt to further activate nucleation sites for free growth. ΔT of an isothermal melt as a balance of latent heat release and heat flow over the columnar zone is visualized in **Fig. 5-1**.

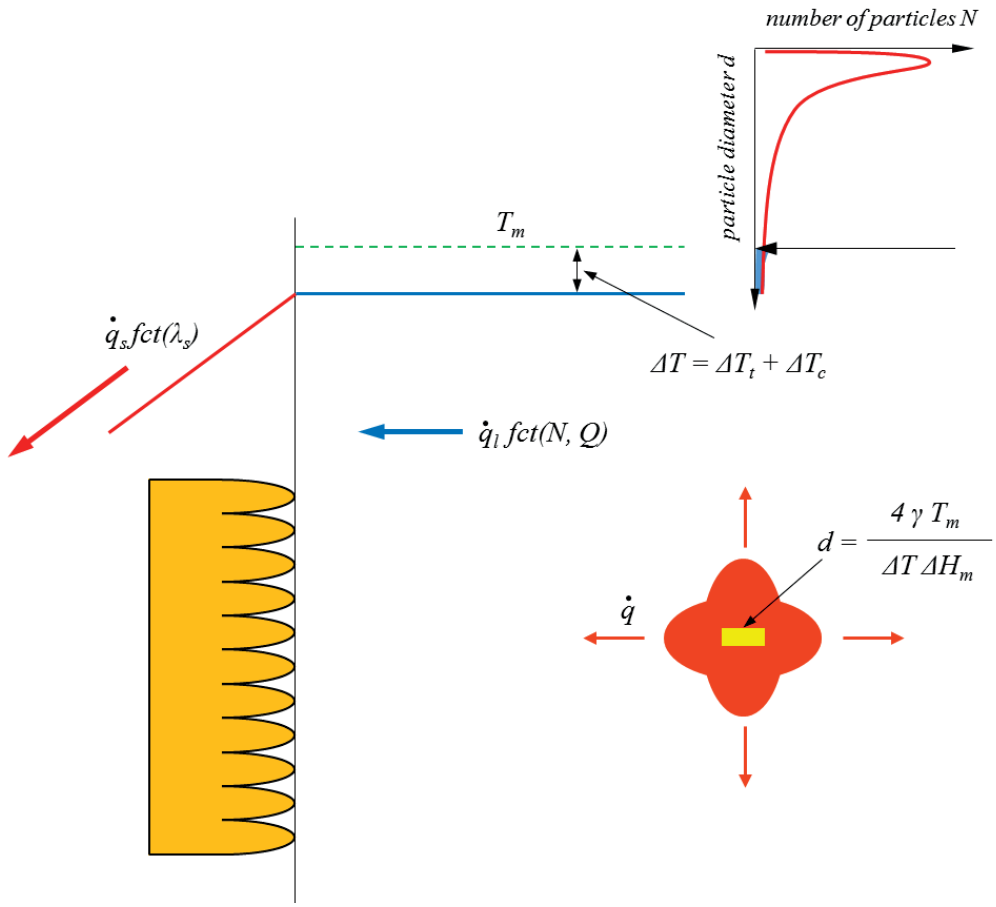

Fig. 5-1: ΔT as a balance of latent heat release and heat flow over the columnar zone.

6 Conclusion

The conclusion can be summarized as follows:

- A comprehensive list of the Q values of the alloying elements in the copper-systems is given. Compared to the aluminium and the magnesium-system the majority of the alloying elements show a relative high Q. However, none of the alloying elements shows a remarkably high Q as it can be found for titanium and tantalum in the aluminium system.
- Phosphorus, beryllium, lithium, yttrium and magnesium seem to be the most powerful reagents in the copper-system. However, the carcinogenic effect of beryllium and the high affinity to oxygen of the other alloying elements have to be taken under consideration.
- To eliminate errors in obtaining data from printed phase diagrams, further work has to be done, more precisely Gulliver-Scheil solidification simulations.
- Metalloid compounds, borides, carbides, nitrides, oxides, sulphides and phosphides, were examined according to their lattice disregistry to the copper lattice.
- Considering of the melting point SrO, ZrO_2, BN, Y_3C/YC_2, MnB_2, AlB_{12} and MgS seem to be the most suitable binary compounds.
- The thermodynamic stability of the examined compounds has to be subjected to a more detailed examination for the alloys under investigation.
- Addition of tin, zinc, magnesium and iron to high purity copper was found to increase grain size.
- Addition of phosphorus to high purity copper was found to decrease grain size.
- It is assumed that the variation of the grain size in alloy systems is of a complex interaction between the overall cooling rate and Q and its effect on constitutional undercooling and growth restriction and thereby latent heat release. The overall cooling rate appears to be affected to a great extent by the heat flow over the columnar zone (λ_s) and latent heat release, dominated by the concentration dependent latent heat release and by undercooling facilitated free growth. Therefore, the final grain size of the respective alloy system is dependent on which factor is dominant.
- Assuming an isothermal melt model the degree of undercooling, determining the activation of nucleants in the centre of the casting can be understood as a balance of latent heat release and the heat flow over the columnar zone.

Furthermore, the latent heat release is a function of the number of activated particles and growth restriction. The heat flow over the columnar zone is determined by λ_s in dependent on the alloying element.

- To confirm the mechanism suggested in this work it is necessary to quantify the effect of the columnar zone, influenced by λ_s, on the cooling rate.

Literature

[1] Quested T.E., Greer A.L., Grain refinement of Al alloys: Mechanisms determining as-cast grain size in directional solidification, Acta Materialia, Vol. 53, 2005, p. 4643-4653.

[2] Perepezko J.H., Nucleation Kinetics, ASM Handbook, Vol. 15: Castings, 1998, p. 101-108.

[3] Murty B. S., Kori S. A., Chakroborty M., Grain refinement of aluminium and its alloys by heterogeneous nucleation and alloying, International Materials Reviews, Vol. 47, No. 1, 2002, p. 3-29.

[4] Greer A. L., Bunn A. M., Tronche A., Evans P. V., Bristow D. J., Modelling of inoculation of metallic melts: Application to grain refinement of aluminium by Al-Ti-B, Acta materialia, Vol. 48, 2000, p. 2823-2835.

[5] Campbell J., Complete casting handbook, Butterworth-Heinemann, 2011, p. 315.

[6] Mannheim R., Reif W., Weber G., Untersuchung der Kornfeinung von Kupfer-Zinn-Legierungen mit Zirconium und/oder Bor und Eisen sowie ihres Einflusses auf die mechanischen Eigenschaften, Gießereiforschung 40, Nr. 1, 1988, p. 1-16.

[7] Sahm P. R., Egry I., Volkmann T., Schmelze, Erstarrung, Grenzfläche, Vieweg, Braunschweig, Wiesbaden, 1999, p. 109-118.

[8] Kurz W., Fischer D.J., Fundamentals of solidification, Fourth Revised Edition,Trans Tech Publications LTD, Switzerland, 1998, p.21-32.

[9] Gottstein G., Physikalische Grundlagen der Materialkunde, 3. Auflage, Springer-Verlag, Berlin/Heidelberg, 2007, p.362-368.

[10] Dantzig J.A, Rappaz M., Solidification, CRC Press, Boca Raton, 2009, p. 33.

[11] Kim W. T., Cantor B., An adsorption model of the heterogeneous nucleation of solidification, Acta Metallurgica et Materialia, Vol. 42, Issue 9, 1994, p. 3115-3127.

[12] Easton M. A., StJohn D. H., A model of grain refinement incorporating alloy constitution and potency of heterogeneous nucleant particles, Acta mater., Vol. 49, 2001, p. 1867-1878.

[13] Quested T. E., Understanding mechanisms of grain refinement of aluminium alloys by inoculation, Materials Science and Technology, Vol. 20, 2004, p. 1357-1368.

[14] Dantzig J.A, Rappaz M., Solidification, CRC Press, Boca Raton, 2009, p. 279-280.

[15] Gottstein G., Physikalische Grundlagen der Materialkunde, 3. Auflage, Springer-Verlag, Berlin/Heidelberg, 2007, p.19-39.

[16] Greer L. A., Cooper P. S., Meredith M. W., Schneider W., Schumacher P., Spittle J. A., Tronche A., Grain refinement of aluminium alloys by inoculation, Advanced Engineering Materials, Vol. 5, No. 1-2, 2003, p. 81-91.

[17] Bunn A. M., Evans P. V., Bristow D. J., Greer A. L., Modelling the effectiveness of Al-Ti-B refiners in commercial purity aluminium, Light Metals 1998, TMS, Warrendale, PA, 1998, p. 963-968.

[18] Kurz W., Fischer D.J., Fundamentals of solidification, Fourth Revised Edition,Trans Tech Publications LTD, Switzerland, 1998, p.46-52.

[19] Sahm P. R., Egry I., Volkmann T., Schmelze, Erstarrung, Grenzfläche, Vieweg, Braunschweig, Wiesbaden, 1999, p. 140-142.

[20] Kurz W., Fischer D.J., Fundamentals of solidification, Fourth Revised Edition,Trans Tech Publications LTD, Switzerland, 1998, p.238-239.

[21] Quested T.E, Dinsdale A. T., Greer A. L., Thermodynamic modelling of growth-restriction effects in aluminium alloys, Acta Materialia, Vol. 53, 2005, p.1323-1334.

[22] Mitransinovic A. M., Robles Hernandes F. C., Determination of the growth restriction factor and grain size for aluminium alloys by a quasi-binary equivalent method, Materials Science and Engineering A, A 540, 2012, p. 63-69.

[23] http://www.doitpoms.ac.uk/tlplib/solidification_alloys/scheil.php, retrieved 15.10.2014.

[24] Kurz W., Fischer D.J., Fundamentals of solidification, Fourth Revised Edition,Trans Tech Publications LTD, Switzerland, 1998, p.125.

[25] Schmid-Fetzer R., Kozlov A., Thermodynamic aspects of grain growth restriction in multicomponent alloy solidification, Acta Materialia, Vol. 59, 2011, p. 6133-6144.

[26] Spittle J. A., Sadli S. B., Effect of alloy variable on grain refinement of binary aluminium alloys with Al-Ti-B, Mater. Sci. Technol., Vol. 11, 1995, p. 533-537.

[27] Cibula A., Grain-refining additions for cast copper alloys, Journal of the institute of metals, Vol. 82, 1953-54, p. 513-524.

[28] Dennison J. P., Tull E. V. The refinement of cast grain-size in copper-aluminium alloys containing 7-9 per cent. aluminium, Journal of the institute of metals, Vol. 85, 1956-57, p. 8-10.

[29] Henke R., Kornfeinung von NE-Metallgußlegierungen, Gießerei-Praxis, Nr. 1, 1965, p. 14-20.

[30] Röhrig K., Kristallisatoren für NE-Metallschmelzen, Metall, Heft 20, 1966, p. 1266-1272.

[31] Couture A., Edwards J. O., Kornfeinung von Kupfer-Sandgußlegierungen und ihr Einfluß auf die Güteeigenschaften, Gießerei-Praxis, Nr. 21, 1974, p. 425-435.

[32] Romankiewicz F., Ellerbrok R., Engler S., Einfluß einer Kornfeinung mit Zirconium auf Erstarrungsmorphologie, Speisungsvermögen und Festigkeitseigenschaften von Messing CuZn30 und Siliciummessing CuZn15Si4, Gießereiforschung, Heft 1, 1987, p. 25-33.

[33] Reif W., Weber G., A new grain refiner for copper-zinc alloys containing 25-42 % zinc, Metall, Heft 11, 1987, p. 1131-1137.

[34] Romankiewicz R., Glazowska I., Rybakowski M., Kornfeinung von Kupferlegierungen, Metall, Vol. 48, Nr. 11, 1994, p. 865-871.

[35] Sadayappan M., Thomson J.P., Elboujdaini M., Ping Gu G., and Sahoo M., Grain refinement of permanent mold cast copper base alloys, Final Report, MTL Report, 2004, p. 1-124.

[36] Balart M. J., Patel J.B., Fan Z., Grain refinement of phosphorus deoxidised copper, Materials Science Forum, Vol. 790-791, 2014, p. 161-166.

[37] Reif W., Kornfeinung von Aluminium-, Blei-, Zinn-, Kupfer- und Nickellegierungen – ein Überblick, Gießerei, Vol. 76, Nr. 2, 1989, p. 41-47.

[38] Weber G., Reif W., Grain refining of copper-based alloys, Int. patent, Nr. 8521134, 1987.

[39] Massalski T., Binary Alloy Phase Diagrams, 2nd Edition, ASM International, Ohio 1990.

[40] Brandes E. A. (ed.), Smithells C. J., Smithells metals reference book, 7th edition, Butterworth-Heinemann, Oxford, 1999.

[41] Pearson W. B., A handbook of lattice spacings and structures of metals and alloys, Vol. 2, 1th edition, 1967.

[42] Steels – Micrographic determination of the apparent grain size, ÖNORM EN ISO 643, 2012.

[43] Stanley H. M., Ellingham Diagrams, http://showard.sdsmt.edu/MET320/Handouts/EllinghamDiagrams/Binder_All_2009_12_06.pdf, retrieved 10.05.2014.

[44] Schumacher P., University of Leoben, Leoben, Austria, personal communication, August 2014.

[45] Binnewies M., Milke E., Thermochemical Data of Elements and Compounds, WILEY-VCH Verlag GmbH, Weinheim, 1999.

[46] Knacke O., Kubaschewski O., Hesselmann K., Thermochemical Properties of Inorganic Substances I, Springer-Verlag, Berling-Heidelberg-New York, Second Edition, 1991.

[47] Knacke O., Kubaschewski O., Hesselmann K., Thermochemical Properties of Inorganic Substances II, Springer-Verlag, Berling-Heidelberg-New York, Second Edition, 1991

[48] Lide D. R., CRC Handbook of Chemistry and Physics, CRC Press, Boca Raton, 1996-1997, p. 4/37-97.

[49] Kislyi P. S., L'vov S. N., Nemchenko V. F., Samsonov G. V., Physical properties of the boride phases of chromium, Soviet Powder Metallurgy and Metal Ceramics, Vol. 1, Issue 6, 1962, p. 441-443.

[50] Dale P. L., Handbook of inorganic compounds, CRC Press, Sec. Edition, Boca Raton, 2011.

[51] http://www.rare-metal.com/Rare_Earth_Nitride.html, retrieved 03.04.2015.

[52] d'. Ans J., Lax E., Blachnik R, Taschenbuch für Chemiker und Physiker. Springer Verlag, 1998, p. 810.

[53] http://www.alfa.com/content/msds/German/41946.pdf, retrieved 03.04.2015.

[54] http://www.americanelements.com/w2ox.html, retrieved 03.04.2015.

[55] Eagleson M., Concise Encyclopedia Chemistry, Walter de Gruyter, 1994.

[56] Men H., Fan Z., Effects of solute content on grain refinement in an isothermal melt, Acta Materialia, Vol. 59, 2011, p. 2704-2712.

[57] Shu D., Sun B., Mi J., Grant P.S., A quantitative study of solute diffusion field effects on heterogeneous nucleation and the grain size of alloys, Acta Materialia, Vol. 59, 2011, p. 2135-2144.

[58] Easton M., StJohn D., Grain refinement of aluminium alloys: Part I. The nucleant and solute paradigms – a review of the literature, Metallurgical and Materials Transactions A, Vol. 30A, 1999, p. 1613-1623.

[59] Klösch G., Kornfeinen von aluminiumhältigen Magnesiumlegierungen, PhD thesis, Leoben, 2006, p. 15-32.

[60] Davis J. R, Copper and Copper Alloys, ASM International, 2001, p. 181-182.

[61] Davis J. R, Copper and Copper Alloys, ASM International, 2001, p. 3, 35-53.

[62] http://www.bgfa.ruhr-uni-bochum.de/publik/info0204/beryllium.php, retrieved 03.04.105.

[63] Zuo Y., Li M., Xia B., Jiang G., Scamans M., Fan Z., Refining grain structure and porosity of an aluminium alloy with intensive melt sharing, Scripta Materialia, Vol. 64, 2011, p. 209-2012.

[64] Bustos O. C., Untersuchung zur Kornfeinung von Reinstkupfer durch chemische Zusätze und Deutung der Vorgänge, PhD Thesis, Berlin, 1990.

[65] Balart M. J., Patel J. B., Gao F., Fan Z., Grain refinement of DHP copper by elemental additions, International Journal of Cast Metals Research, 2015, unpublished paper.

[66] Lee Y.C., Dahle A.K., StJohn D.H., Hutt J.E.C., The effect of grain refinement and silicon content on grain formation in hypoeutectic Al-Si alloys, Materials Science and Engineering A259, 1999, p. 43-52.

[67] Johnsson M., Grain refinement of aluminium studied by use of a thermal analytical technique, Thermochimica Acta, Vol. 256, 1995, p. 107-121.

[68] Johnsson M., Bäckerud L., The influence of composition on equiaxed crystal growth mechanisms and grain size in Al alloys, Zeitschrift für Metallkunde, Vol. 87/3, p. 216-220.

[69] Doppelhofer B., Kornfeinung in AlSi-Legierungen, Master Thesis, Leoben, 2014, p. 48.

[70] Hodaj F., Durand F., Equiaxed grains in multicomponent allos: Effect of the growth rate, Acta Materialia, Vol. 45, 1997, p. 2121-2127.

[71] Wu M., Ahmadein M., Kharicha A., Ludwig A., Li J.H., Schumacher P., Simulation of the as-cast structure of Al-4.0wt%Cu ingots with a 5-phase mixed columnar-equiaxed solidification model.

[72] Easton M. A., StJohn D. H., Improved prediction of the grain size of aluminium alloys that include the effect of cooling rate, Materials Science and Engineering A, Vol. 486, 2008, p. 8-13.

[73] Prasad A., Yuan L., Lee P. D., StJohn D. H., The Interdependence model of grain nucleation: A numerical analysis of the Nucleation-Free Zone, Acta Materialia, Vol. 61, 2013, p. 5914-5927.

[74] http://www.matweb.com/reference/copper-alloys.aspx, retrieved 08.01.2015.

[75] Deutsches Kupferinstitut, Kupfer – Vorkommen, Gewinnung, Eigenschaften, Verarbeitung, Verwendung, www.kupferinstitut.de, retrieved 10.05.2014.

[76] Davis J. R, Copper and Copper Alloys, ASM International, 2001, p. 355-481.

[77] Mills K. C., Recommended values of thermophysical properties for selected commercial alloys, Woodhead Publishing Limited, Cambridge, 2002, p. 19-68, 89-98.

[78] Maxwell I., Hellawell A., A simple model for grain refinement during solidification, Acta Metallurgica, Vol. 23, 1975, p. 229-237.

List of figures

List of tables

7 Appendix

7.1 Grain size of aluminium in dependent on the silicon content obtained from Johnsson and Bäckerud [67,68]

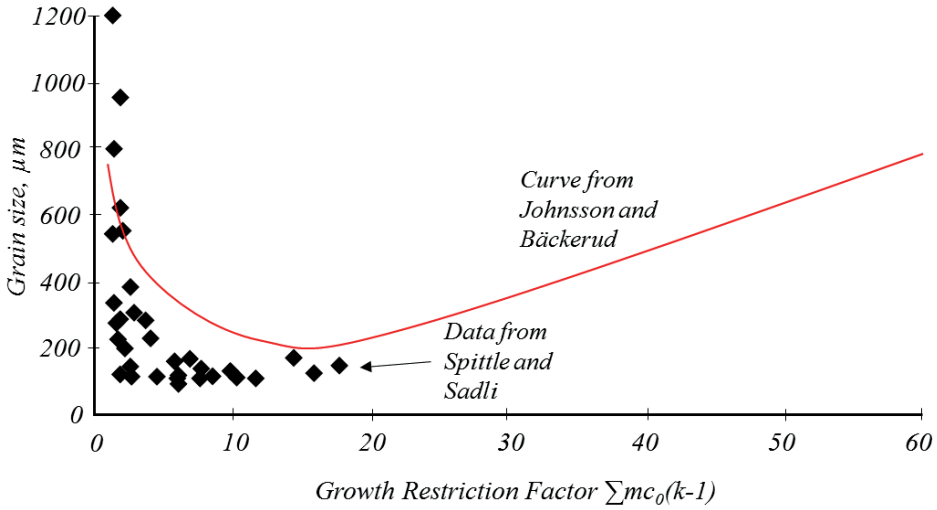

Fig. 7-1: Grain size data of Spittle and Sadli [26] plotted against Q, overlayed by the curve of Bäckerud and Johnsson [67,68] for aluminium-silicon alloys with iron and titanium at casting temperatures of 775°C and cooling rates of 1 K/s, in both cases Al-5Ti-B was added at a concentration of 0,01 wt% titanium after [12]

7.2 Grain size of high purity aluminium in dependent on the silicon content obtained from Lee et al. [66]

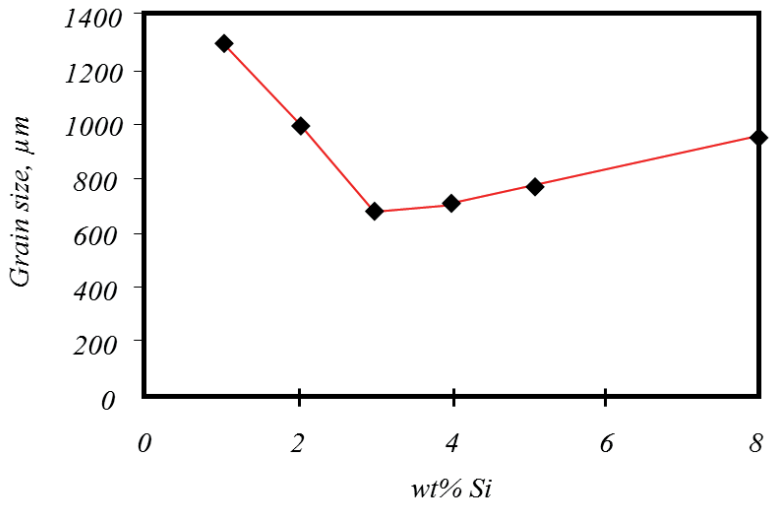

Fig. 7-2: Grain size in dependent on the silicon content without the addition of grain refiner, 99,99 % aluminium, casting temperature 800°C, cooling rate 0,7 K/s, adapted from [66].

7.3 Grain size of commercial purity aluminium in dependent on the silicon content obtained from Doppelhofer [69]

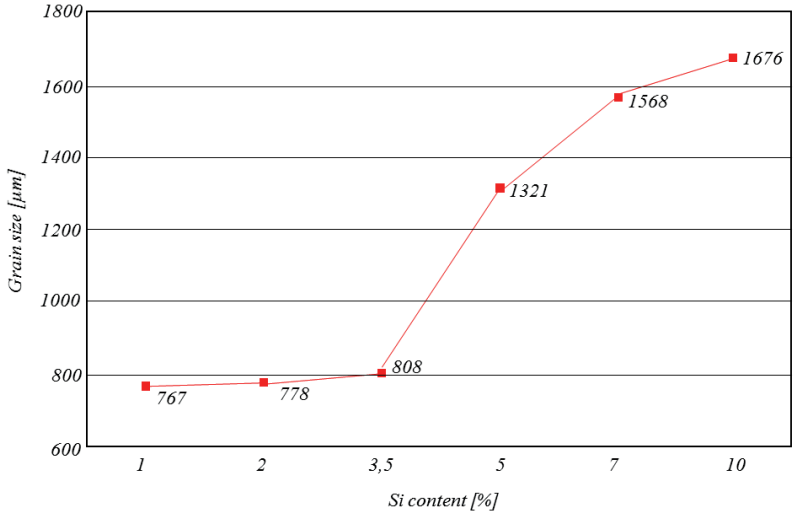

Fig. 7-3: Grain size in dependent on the silicon content without the addition of grain refiner, 99,8 % aluminium, casting temperature 720°C, cooling rate 3,5 K/s, adapted from [69].

7.4 Grain size of high purity aluminium in dependent on the addition of several alloying elements obtained from Spittle and Sadli [26]

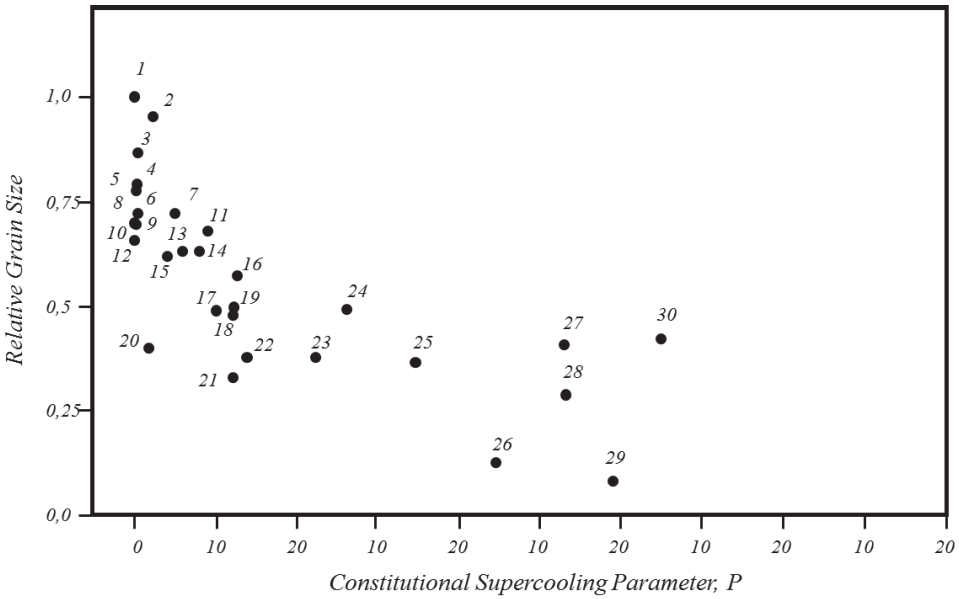

Fig. 7-4: Relative grain size vs. constitutional supercooling parameter P, for binary aluminium alloys given in **Tab. 7-1**, 99,99 % aluminium, cooling rate 3,5 K/s after [26].

Tab. 7-1: Relative grain size measurements for binary aluminium alloys without the addition of grain refiner [26].

Alloy number	Alloy system Al-X	Composition alloy X, wt%	Grain size, µm
1	Al	-	3800
2	Al-Zn	0,90	3635
3	Al-Zr	0,05	3307
4	Al-Mn	0,70	3003
5	Al-Mn	0,60	2984
6	Al-Cr	0,10	2736
7	Al-Zn	1,82	2718
8	Al-Mn	0,10	2706
9	Al-Mn	0,30	2604
10	Al-Mn	0,50	2547
11	Al-Cu	0,97	2583
12	Al-Cr	0,05	2512
13	Al-Zn	2,59	2375
14	Al-Zn	3,13	2380
15	Al-Si	0,15	2364
16	Al-Cu	2,24	2174
17	Al-Zn	4,20	1864
18	Al-Cu	2,32	1832

19	Al-Si	0,35	1858
20	Al-Fe	0,08	1530
21	Al-Fe	0,21	1238
22	Al-Mg	1,06	1396
23	Al-Si	0,55	1417
24	Al-Mg	1,90	1877
25	Al-Si	0,80	1393
26	Al-Cu	4,13	450
27	Al-Mg	4,45	1570
28	Al-Si	1,29	1109
29	Al-Cu	5,15	309
30	Al-Si	1,42	1595

7.5 Grain size of high purity copper in dependent on the addition of various alloying elements at concentrations of 0,1 % obtained from Bustos [64]

Tab. 7-2: Grain size of high purity copper by the addition of various alloying elements at concentrations of 0,1 wt% [64].

element 0,1 wt%	grain size [µm]	element 0,1 wt%	grain size [µm]
-	650	**Ni**	1810
Be	610	**Zn**	395
Mg	405	**Cd**	1650
Ca	470	**Al**	1150
Sr	510	**In**	210
Y	1420	**Tl**	570
La	1630	**Si**	1050
Ce	1800	**Ge**	1100
Ti	1120	**Sn**	580
Zr	590	**Pb**	595
Nb	680	**P**	190
V	640	**As**	210
Ta	480	**Sb**	180
Cr	1580	**Bi**	165
Mo	310	**S**	169
Mn	620	**Se**	190
		Te	130

7.6 Thermal conductivity of the liquid and the solid and latent heat of commercial aluminium alloys at the melting point

Tab. 7-3: Thermal conductivity of the liquid and the solid and latent heat of commercial aluminium alloys at the melting point obtained from [77,Magma$^{5©}$].

Alloy	Thermal conductivity of the liquid [W/mK]	Thermal conductivity of the solid [W/mK]	Latent heat [J/g]
pure Al[77]	91	211	397
Al Si5Cu3Zn1[77]	70	150	400
Al Mg4,5[77]	63	139	358
Al Si12Mg1,2Cu0,9Fe0,8Ni0,8[77]	64	147	489
Al Si7Mg0,4[77]	65,8	134	425
Al Si0,85[77]	97	217	367
Al Cu4,4Mg1,5[77]	85,5	188	297
Al Mg1Mn1[77]	61	183	382
Al Mg1Fe0,7Si0,6[77]	90	200	336
Al Zn5,6Mg2,5Cu1,6[77]	85	193	332
Al Si0,5[Magma5]	90,7	211	395,8
Al Cu4[Magma5]	87	193	389,9
Al Mg3[Magma5]	90	132	389
Al Mg5Cu0,8[Magma5]	90	132	385
Al Mg9Si2Fe0,7[Magma5]	80	169,9	414
Al Si7Mg0,4[Magma5]	68	166	430,5
Al Si10Mg0,3[Magma5]	73	146	476,5
Al Si12[Magma5]	70	145	534
Al Zn5,5Mg2,5Cu1,5[Magma5]	100	170	367

7.7 Thermal conductivity of the liquid and the solid and latent heat of commercial copper alloys at the melting point

Tab. 7-4: Thermal conductivity of the liquid and the solid and latent heat of commercial copper alloys obtained from [77,Magma[5©]].

Alloy	Thermal conductivity of the liquid [W/mK]	Thermal conductivity of the solid [W/mK]	Latent heat [J/g]
pure Cu[77]	146	330	208,7
CuAl9,7Fe4,6Ni4,6[77]	27	42	195
pure Cu[Magma577]	178	296	205
CuAl8Mn5,5Ni1,5[Magma5]	68	130	225
CuAl9Fe3Ni2[Magma5]	68	130	226,7
CuAl10Fe3Ni3[Magma5]	80	130	226,4
CuAl10Ni5,3Fe4,5[Magma5]	68	130	232,8
CuSn5Zn5Pb5Ni2[Magma5]	144	180	186,7
CuSn12Ni1,9Pb0,9[Magma5]	150	180	188
CuZn34Al2Fe2Mn2[Magma5]	70	145	179,5
CuZn39Pb0,75[Magma5]	70	145	177,9
CuZn40Pb1,5Sn0,9[Magma5]	70	140	195,1

7.8 Thermal conductivity of low alloyed copper alloys at 20°C

Tab. 7-5: Thermal conductivity of low alloyed wrought and cast alloys at 20°C obtained from [76].

Wrought alloy	Thermal conductivity [W/mK]	Cast alloy	Thermal conductivity [W/mK]
Oxygen free electronic copper	391	**99,7Cu-0,3Ag**	346
Oxygen free extra-low phosphorus copper	386	**99Cu-0,8Cr-0,06Be**	259
Oxygen free silver copper	388	**99Cu-1Cr**	315
Oxygen free low phosphorus copper	350	**97Cu-1,5Co-1Ag-0,4Be**	218
99,9Cu-0,1Cd 99,8Cu-0,2Cd	377	**97Cu-2,5Co-0,5Be**	218
99,6Cu-0,4S	374	**98Cu-1,5Ni-0,5Be**	183
99,85Cu-0,15Zr	367	**98Cu-1,7Be-0,3Co**	109
99,9Cu-0,1Zr	360	**97,2Cu-2Be-0,5Co-0,25Si**	105
99,75Cu-0,11Mg-0,06P	345	**97Cu-2,4Be-0,5Co**	100
99Cu-1Cd	360	**85Cu-5Sn-5Pb-5Zn**	72

98Cu-1,7Be-0,3Co	118	**-**	-
99,2Cu-0,3Be-0,5Co	233	**-**	-
97Cu-0,5Be-2,5Co	215-245	**-**	-
99Cu-0,8Cr-0,16Zr-0,04Mg	324	**-**	-
99Cu-1Cr	177	**-**	-
99Cu-1Pb	377	**-**	-
98,97Cu-1Fe-0,03P	251	**-**	-
Cu-2,35Fe-0,03P-0,12Zn	260	**-**	-
97Cu-1,5Fe-0,1P-0,8Co-0,6Sn	199	**-**	-
97,97Cu-0,75Fe-1,25Sn-0,03P	173	**-**	-
99,15Cu-0,6Fe-0,2P-0,05Mg	320	**-**	-
95Cu-5Zn	234	**-**	-

7.9 Nucleation sites for copper alloys

7.9.1 Examined borides

7.9.1.1 Cubic structure

Tab. 7-6: Lattice dimension and lattice disregistry of examined borides with cubic structure [40,41].

compound	crystallographic structure	lattice dimension [Å]	misfit [%]	rotation of planes, model 1, misfit [%]	rotation of planes, model 2, misfit [%]
		a	(001)	(001)	(001)
$InNi_3B_{0,5}$	cubic	3,77	**4,52**	-26,10	-63,05
$PrB_{x<4}$	cubic	3,81	5,54	-25,37	-62,69
YB_6	cubic	4,07	12,74	-20,28	-60,14
DyB_6	cubic	4,10	13,51	-19,74	-59,87
HoB_6	cubic	4,10	13,52	-19,73	-59,87
ErB_6	cubic	4,10	13,57	-19,69	-59,85
TbB_6	cubic	4,11	13,85	-19,50	-59,75
LuB_6	cubic	4,11	13,85	-19,50	-59,75
PrB_6	cubic	4,12	14,13	-19,30	-59,65
NdB_6	cubic	4,12	14,13	-19,30	-59,65
GdB_6	cubic	4,12	14,13	-19,30	-59,65
TmB_6	cubic	4,12	14,13	-19,30	-59,65
NdB_6	cubic	4,13	14,29	-19,18	-59,59
SmB_6	cubic	4,13	14,35	-19,14	-59,57
CeB_6	cubic	4,13	14,40	-19,10	-59,55
YbB_6	cubic	4,13	14,40	-19,10	-59,55
CaB_6	cubic	4,15	14,96	-18,71	-59,36
LaB_6	cubic	4,15	14,96	-18,71	-59,36
EuB_6	cubic	4,16	15,32	-18,46	-59,23
SrB_6	cubic	4,19	16,07	-17,93	-58,96
ThB_6	cubic	4,20	16,34	-17,73	-58,87
Nb_9B	cubic	4,21	16,62	-17,54	-58,77
TiB	cubic	4,21	16,62	-17,54	-58,77
BaB_6	cubic	4,25	17,78	-16,71	-58,36
$Mo_3B_{0,1}C_{1,9}$	cubic	4,27	18,28	-16,36	-58,18
BaB_6	cubic	4,28	18,56	-16,17	-58,08
ScB_6	cubic	4,44	22,85	-13,13	-56,56
PB	cubic	4,53	25,60	-11,19	-55,60
HfB	cubic	4,62	27,98	-9,51	-54,75
ZrB	cubic	4,65	28,81	-8,92	-54,46
Be_2B	cubic	4,66	29,17	-8,66	-54,33
AsB	cubic	4,78	32,33	-6,43	-53,22
AlBeB	cubic	4,95	37,17	**-3,00**	-51,50

RuB	cubic	7,02	94,46	37,50	-31,25
OsB	cubic	7,03	94,74	37,70	-31,15
DyB_{12}	cubic	7,10	96,70	39,09	-30,45
ZrB_{12}	cubic	7,41	105,26	45,14	-27,43
ScB_{12}	cubic	7,42	105,60	45,38	-27,31
LuB_{12}	cubic	7,46	106,76	46,20	-26,90
YbB_{12}	cubic	7,47	106,90	46,30	-26,85
UB_{12}	cubic	7,47	106,93	46,32	-26,84
TmB_{12}	cubic	7,48	107,09	46,44	-26,78
ErB_{12}	cubic	7,48	107,31	46,59	-26,70
HoB_{12}	cubic	7,49	107,53	46,75	-26,63
TbB_{12}	cubic	7,50	107,87	46,98	-26,51
CuSB	cubic	9,82	172,02	92,35	**-3,83**
CuSeB	cubic	10,22	183,10	100,18	**0,09**
LaB_{13}	cubic	10,44	189,20	104,49	**2,25**
$Al_{2,5}Ni_{20,5}B_6$	cubic	10,48	190,42	105,35	**2,68**
$Al_3Co_{20}B_6$	cubic	10,52	191,30	105,98	**2,99**
Co_7GaB_2	cubic	10,52	191,41	106,06	**3,03**
$GaNi_7B_2$	cubic	10,53	191,69	106,26	**3,13**
$GeNi_7B_2$	cubic	10,53	191,69	106,26	**3,13**
$Ni_{19,5}Zn_{3,5}B_6$	cubic	10,56	192,38	106,75	**3,37**
Ni_5TaB_2	cubic	10,57	192,66	106,94	**3,47**
$Mg_3Ni_20B_6$	cubic	10,57	192,77	107,02	**3,51**
$In_2Ni_{21}B_6$	cubic	10,58	193,10	107,25	**3,63**
$Fe_{23}B_3C_3$	cubic	10,59	193,46	107,51	**3,75**
$Ni_{21}Sn_2B_6$	cubic	10,60	193,57	107,59	**3,79**
$Co_{21}Sn_2B_6$	cubic	10,60	193,66	107,65	**3,82**
AgSeB	cubic	10,88	201,39	113,11	6,56

7.9.1.2 Tetragonal structure

Tab. 7-7: Lattice dimension and lattice disregistry of examined borides with tetragonal structure [40,41].

compound	crystallographic structure	lattice dimension [Å]		misfit [%]		rotation of planes, model 1, misfit [%]	rotation of planes, model 2, misfit [%]
		a	c	(001)	(100)	(001)	(001)
Pt_3B_2	tetragonal	2,78	2,96	-22,99	-18,01	-45,55	-72,77
$IrB_{1,1}$	tetragonal	2,81	10,26	-22,16	184,29	-44,96	-72,48
MoB	tetragonal	3,11	16,97	-13,85	370,08	-39,08	-69,54
WB	tetragonal	3,12	16,93	-13,57	368,98	-38,89	-69,44
$Be_{4\text{-}5}B$	tetragonal	3,37	7,05	-6,68	95,29	-34,01	-67,00
$YbB_{x<4}$	tetragonal	3,77	3,56	**4,43**	**-1,39**	-26,16	-63,08
YB_x (x~3)	tetragonal	3,78	3,55	**4,71**	**-1,66**	-25,96	-62,98
$GdB_{x<4}$	tetragonal	3,79	3,63	**4,99**	**0,55**	-25,76	-62,88
$LaB_{x<4}$	tetragonal	3,82	3,96	5,82	9,70	-25,18	-62,59
Ni_2B	tetragonal	4,98	4,24	37,95	17,45	**-2,45**	-51,23
Co_2B	tetragonal	5,01	4,21	38,78	16,62	**-1,87**	-50,93
Fe_2B	tetragonal	5,10	4,24	41,27	17,45	**-0,10**	-50,05
MnB_2	tetragonal	5,15	4,21	42,60	16,57	**0,84**	-49,58
Mn_2B	tetragonal	5,15	4,21	42,66	16,62	**0,88**	-49,56
Cr_2B	tetragonal	5,18	4,31	43,49	19,39	**1,46**	-49,27
Co_5PB_2	tetragonal	5,42	10,20	50,14	182,55	6,16	-46,92
Cr_5B_3	tetragonal	5,46	10,64	51,25	194,74	6,95	-46,53
CrB_6	tetragonal	5,47	7,15	51,50	98,12	7,12	-46,44
Fe_5PB_2	tetragonal	5,48	10,33	51,86	186,20	7,38	-46,31
$CuSe_2B$	tetragonal	5,54	5,37	53,43	48,67	8,49	-45,75
Mo_2B	tetragonal	5,54	4,74	53,46	31,30	8,51	-45,74
Mn_5PB_2	tetragonal	5,54	10,49	53,46	190,58	8,51	-45,74
Fe_5SiB_2	tetragonal	5,55	10,34	53,80	186,37	8,75	-45,63
W_2B	tetragonal	5,56	4,74	54,02	31,30	8,91	-45,55
Mn_5SiB_2	tetragonal	5,61	10,44	55,40	189,20	9,89	-45,06
V_3B_2	tetragonal	5,73	3,03	58,67	-16,18	12,20	-43,90
$Ta_{2,4}B$	tetragonal	5,78	4,86	60,10	34,75	13,21	-43,40
Ta_2B	tetragonal	5,78	4,86	60,11	34,63	13,22	-43,39
SiV_5B_2	tetragonal	5,81	10,79	60,94	198,89	13,80	-43,10
$Mo_5(Si,B)_3$	tetragonal	6,01	11,03	66,57	205,54	17,78	-41,11
Ti_2B	tetragonal	6,11	4,56	69,25	26,32	19,68	-40,16
Ta_3B_2	tetragonal	6,18	3,28	71,08	-9,02	20,97	-39,51
Nb_3B_2	tetragonal	6,19	3,29	71,52	-8,89	21,29	-39,36
MoB_4	tetragonal	6,34	4,50	75,62	24,65	24,18	-37,91
WB4	tetragonal	6,34	4,50	75,62	24,65	24,18	-37,91
$Nb_5(Si,B)_3$	tetragonal	6,39	11,68	76,87	223,55	25,07	-37,47
LuB_4	tetragonal	7,00	3,94	93,82	9,09	37,05	-31,47
YbB_4	tetragonal	7,01	4,00	94,18	10,80	37,31	-31,35

ErB_4	tetragonal	7,07	4,00	95,87	10,73	38,50	-30,75
UB_4	tetragonal	7,08	3,98	96,12	10,25	38,68	-30,66
HoB_4	tetragonal	7,09	4,01	96,29	11,02	38,80	-30,60
YB_4	tetragonal	7,09	4,01	96,29	11,14	38,80	-30,60
PuB_4	tetragonal	7,10	4,01	96,68	11,19	39,07	-30,46
DyB_4	tetragonal	7,10	4,02	96,70	11,29	39,09	-30,45
TbB_4	tetragonal	7,13	4,07	97,51	12,74	39,66	-30,17
GdB_4	tetragonal	7,14	4,05	97,89	12,13	39,93	-30,03
SmB_4	tetragonal	7,17	4,07	98,73	12,73	40,52	-29,74
PrB_4	tetragonal	7,20	4,11	99,45	13,85	41,03	-29,49
CeB_4	tetragonal	7,21	4,09	99,72	13,30	41,23	-29,39
NdB_4	tetragonal	7,22	4,10	99,97	13,63	41,40	-29,30
ThB_4	tetragonal	7,26	4,11	101,00	13,93	42,13	-28,94
ThB_4	tetragonal	7,26	4,11	101,11	13,85	42,20	-28,90
LaB_4	tetragonal	7,32	4,18	102,88	15,82	43,46	-28,27
$Co_{4,7}Si_2B$	tetragonal	8,62	4,25	138,64	17,73	68,75	-15,63
ε_1-$Co_3P_{0,5}B_{0,5}$	tetragonal	8,69	4,30	140,61	19,20	70,14	-14,93
ε-$Co_3P_{0,5}B_{0,5}$	tetragonal	8,78	4,34	143,21	20,11	71,98	-14,01
ε_1-$Fe_3P_{0,37}B_{0,63}$	tetragonal	8,81	4,38	144,10	21,19	72,60	-13,70
$Fe_{4,86}Si_2B$	tetragonal	8,82	4,34	144,27	20,14	72,72	-13,64
$Al_3B_{48}C_2$	tetragonal	8,82	5,09	144,32	41,00	72,76	-13,62
BeB_6	tetragonal	10,16	14,28	181,44	295,57	99,01	**-0,50**
AlB_{12}	tetragonal	10,28	14,30	184,76	296,12	101,36	**0,68**
GaB_{12}	tetragonal	12,93	4,84	258,17	34,07	153,27	26,63
CuSB	tetragonal	13,88	9,81	284,49	171,75	171,87	35,94
AgSB	tetragonal	15,39	10,88	326,32	201,39	201,45	50,73

7.9.1.3 Hexagonal structure

7.9.1.3.1 (0001) plane

Tab. 7-8: Lattice dimension and lattice disregistry ((0001) plane) of examined borides with hexagonal structure [40,41].

compound	crystallographic structure	lattice dimension [Å]		misfit [%]
		a	c	(0001)
OsB	hcp	2,87	2,88	12,47
OsB_2	hcp	2,88	2,87	12,67
Ru_2B_5	hcp	2,89	12,81	13,22
TcB_2	hcp	2,89	7,45	13,29
ReB_2	hcp	2,90	7,48	13,61
ReB_3	hcp	2,90	7,48	13,61
Os_2B_5	hcp	2,91	12,91	14,00
CrB_2	hcp	2,97	3,07	16,31
Re_2B_5	hcp	2,97	13,80	16,35
Ti_2B_5	hcp	2,98	13,98	16,74
W_2B_5	hcp	2,98	13,87	16,74
Ti_2B_5	hcp	2,98	13,98	16,74
VB_2	hcp	3,00	3,06	17,52
AlB_2	hcp	3,00	3,25	17,52
AgB_2	hcp	3,00	3,24	17,52
MoB_{12}	hcp	3,00	3,17	17,68
WB_2	hcp	3,02	3,05	18,31
TiB_2	hcp	3,03	3,22	18,70
Ti_2B	hcp	3,03	3,23	18,70
MoB_2	hcp	3,05	3,11	19,48
TaB_2	hcp	3,08	3,27	20,66
MgB_2	hcp	3,08	3,52	20,79
NbB_2	hcp	3,09	3,30	21,05
UB_2	hcp	3,13	3,99	22,59
AuB_2	hcp	3,14	3,52	23,01
ScB_2	hcp	3,15	3,52	23,24
ZrB_2	hcp	3,17	3,53	24,18
HoB_2	hcp	3,17	3,81	24,18
PuB_2	hcp	3,18	3,94	24,58
LuB_2	hcp	3,25	3,70	27,16
$RhB_{1,1}$	hcp	3,31	4,22	29,63
PtB	hcp	3,36	4,06	31,55
PB	hcp	3,56	5,90	39,54
ThB_2C	hcp	3,87	3,81	51,53
WB_{12}	hcp	3,99	3,17	56,46
$Al_4B_{1-3}C_4$	hcp	5,90	15,90	131,13

Ni_6Si_2B	hcp	6,11	2,90	139,16
SiB_3	hcp	6,32	12,71	147,55
$Si_{11}B_{31}$	hcp	6,32	12,71	147,55
SiB_4	hcp	6,33	12,74	147,98
Pd_3B_2	hcp	6,48	3,42	153,85
TmB_4	hcp	7,05	3,99	176,18
Tc_7B_3	hcp	7,42	4,78	190,56
Ru_7B_3	hcp	7,47	4,71	192,52
Re_7B_3	hcp	7,50	4,77	193,97
$Nb_5(Si,B)_3$	hcp	7,58	5,27	196,91
$Al_3Ta_5B_x$	hcp	7,79	5,31	205,13
BeB_3	hcp	9,79	9,55	283,52
BeB_2	hcp	9,79	9,55	283,52

7.9.1.3.2 (10-10) plane

Tab. 7-9: Lattice dimension and lattice disregistry ((10-10) plane) of examined borides with hexagonal structure [40,41].

compound	crystallographic structure	lattice dimension [Å]		misfit [%]	
		a	c	a	c
OsB	hcp	2,87	2,88	-20,47	-20,33
OsB_2	hcp	2,88	2,87	-20,33	-20,47
Ru_2B_5	hcp	2,89	12,81	-19,94	254,85
TcB_2	hcp	2,89	7,45	-19,89	106,45
ReB_2	hcp	2,90	7,48	-19,67	107,15
ReB_3	hcp	2,90	7,48	-19,67	107,06
Os_2B_5	hcp	2,91	12,91	-19,39	257,62
CrB_2	hcp	2,97	3,07	-17,76	-15,07
Re_2B_5	hcp	2,97	13,80	-17,73	282,27
Ti_2B_5	hcp	2,98	13,98	-17,45	287,26
W_2B_5	hcp	2,98	13,87	-17,45	284,21
Ti_2B_5	hcp	2,98	13,98	-17,45	287,26
VB_2	hcp	3,00	3,06	-16,90	-15,24
AlB_2	hcp	3,00	3,25	-16,90	-9,97
AgB_2	hcp	3,00	3,24	-16,90	-10,25
MoB_{12}	hcp	3,00	3,17	-16,79	-12,08
WB_2	hcp	3,02	3,05	-16,34	-15,51
TiB_2	hcp	3,03	3,22	-16,07	-10,80
Ti_2B	hcp	3,03	3,23	-16,07	-10,53
MoB_2	hcp	3,05	3,11	-15,51	-13,85
TaB_2	hcp	3,08	3,27	-14,68	-9,42
MgB_2	hcp	3,08	3,52	-14,59	-2,46
NbB_2	hcp	3,09	3,30	-14,40	-8,59
UB_2	hcp	3,13	3,99	-13,32	10,51

AuB_2	hcp	3,14	3,52	-13,02	-2,49
ScB_2	hcp	3,15	3,52	-12,85	-2,58
ZrB_2	hcp	3,17	3,53	-12,19	-2,22
HoB_2	hcp	3,17	3,81	-12,19	5,54
PuB_2	hcp	3,18	3,94	-11,91	9,14
LuB_2	hcp	3,25	3,70	-10,08	2,60
$RhB_{1,1}$	hcp	3,31	4,22	-8,34	17,01
PtB	hcp	3,36	4,06	-6,98	12,41
PB	hcp	3,56	5,90	-1,33	63,43
ThB_2C	hcp	3,87	3,81	7,15	5,54
WB_{12}	hcp	3,99	3,17	10,64	-12,08
$Al_4B_{1-3}C_4$	hcp	5,90	15,90	63,43	340,44
Ni_6Si_2B	hcp	6,11	2,90	69,11	-19,81
SiB_3	hcp	6,32	12,71	75,04	252,16
$Si_{11}B_{31}$	hcp	6,32	12,71	75,04	252,16
SiB_4	hcp	6,33	12,74	75,35	252,80
Pd_3B_2	hcp	6,48	3,42	79,50	-5,26
TmB_4	hcp	7,05	3,99	95,29	10,53
Tc_7B_3	hcp	7,42	4,78	105,46	32,33
Ru_7B_3	hcp	7,47	4,71	106,84	30,55
Re_7B_3	hcp	7,50	4,77	107,87	32,19
$Nb_5(Si,B)_3$	hcp	7,58	5,27	109,94	45,84
Al_3Ta5B_x	hcp	7,79	5,31	115,76	46,95
BeB_3	hcp	9,79	9,55	171,19	164,54
BeB_2	hcp	9,79	9,55	283,52	164,54

7.9.1.4 Orthorhombic structure

Tab. 7-10: Lattice dimension and lattice disregistry of examined borides with orthorhombic structure [40,41].

compound	crystallographic structure	lattice dimension [Å]			misfit [%]		
		a	c	b	a	c	b
RuB_2	orthorhombic	2,87	4,65	4,05	-20,64	28,67	12,05
Re_3B	orthorhombic	2,89	7,26	9,13	-19,94	101,05	152,94
Tc_3B	orthorhombic	2,89	7,25	9,16	-19,92	100,72	153,77
NiB	orthorhombic	2,93	3,00	7,40	-18,98	-17,01	104,88
CrB	orthorhombic	2,96	2,94	7,81	-18,01	-18,56	116,34
Cr_3B_4	orthorhombic	2,98	2,95	13,02	-17,45	-18,28	260,66
Mn_3B_4	orthorhombic	3,03	2,96	12,86	-16,07	-18,01	256,23
V_3B_4	orthorhombic	3,03	2,99	13,18	-16,07	-17,29	265,10
Mo_2BC	orthorhombic	3,09	3,05	17,35	-14,52	-15,60	380,61
VB	orthorhombic	3,10	2,98	8,17	-14,13	-17,45	126,32
β-MoB	orthorhombic	3,15	3,08	8,47	-12,71	-14,63	134,63
$Ti_{0,5}WB$	orthorhombic	3,18	3,07	8,46	-11,91	-14,93	134,40
WB	orthorhombic	3,19	3,07	8,40	-11,63	-14,96	132,69
TaB	orthorhombic	3,28	3,16	0,87	-9,14	-12,47	-75,98
Ta_3B_4	orthorhombic	3,29	3,13	14,00	-8,86	-13,30	287,81
NbB	orthorhombic	3,30	3,17	8,72	-8,59	-12,19	141,55
Nb_3B_4	orthorhombic	3,31	3,14	14,08	-8,31	-13,02	290,03
UBC	orthorhombic	3,60	3,35	11,97	-0,33	-7,31	231,58
CoB	orthorhombic	3,95	3,04	5,34	9,42	-15,79	47,92
FeB	orthorhombic	4,05	2,95	5,50	12,19	-18,28	52,35
MnB	orthorhombic	4,15	2,98	5,56	14,96	-17,45	54,02
Cr_4B	orthorhombic	4,26	14,71	7,38	18,01	307,48	104,43
Ni_3B	orthorhombic	4,39	6,62	5,21	21,58	83,35	44,35
Ni_3B	orthorhombic	4,39	6,62	5,21	21,58	83,35	44,35
Co_3B	orthorhombic	4,41	6,63	5,23	22,16	83,66	44,88
RuB_2	orthorhombic	4,65	4,05	2,87	28,67	12,05	-20,64
OsB_2	orthorhombic	4,68	4,08	2,87	29,73	12,91	-20,45
ScB_2C_2	orthorhombic	5,18	3,44	10,08	43,35	-4,71	179,09
Co_3B	orthorhombic	5,22	4,41	6,63	44,68	22,11	83,63
Rh_2B	orthorhombic	5,42	7,44	3,98	50,14	106,09	10,25
Pd_3B	orthorhombic	5,46	4,85	7,57	51,33	34,40	109,61
Mo_5SiB_2	orthorhombic	6,00	1,87	11,21	66,15	-48,25	210,44
Cr_2NiB_4	orthorhombic	6,05	5,96	12,67	67,59	65,10	250,97
TiB	orthorhombic	6,12	4,56	3,06	69,53	26,32	-15,24
$TiB_{1,1}$	orthorhombic	6,12	4,56	3,06	69,53	26,32	-15,24
$Al_6Mo_7B_7$	orthorhombic	6,35	5,77	7,04	75,90	59,83	95,01
$AlB_{24}C_4$	orthorhombic	8,88	5,69	9,10	145,98	57,62	152,08
AlB_{10}	orthorhombic	8,88	5,69	9,10	146,01	57,62	152,08

As_2B_{13}	orthorhombic	9,71	3,07	4,34	168,95	-14,99	20,30
$Ru_{11}B_8$	orthorhombic	11,61	2,84	11,34	221,58	-21,44	214,18
Ni_4B_3	orthorhombic	11,97	6,58	2,99	231,66	82,38	-17,31
β-AlB_{12}	orthorhombic	12,34	10,16	12,63	241,83	181,47	249,89
SiB_6	orthorhombic	14,39	9,89	18,27	298,67	173,83	406,02
Mn_4B	orthorhombic	14,53	4,21	7,29	302,49	16,62	101,94
$Cr_{0,9}Fe_{1,1}B_{0,9}$	orthorhombic	14,57	4,22	7,32	303,60	16,90	102,77
Cr_2B	orthorhombic	14,70	4,29	7,34	307,20	18,84	103,32
γ-AlB_{12}	orthorhombic	16,56	10,16	17,53	358,73	181,44	385,60

7.9.2 Examined carbides

7.9.2.1 Cubic structure

Tab. 7-11: Lattice dimension and lattice disregistry of examined carbides with cubic structure [40,41].

compound	crystallographic structure	lattice dimension [Å]	misfit [%]	rotation of planes, model 1, misfit [%]	rotation of planes, model 2, misfit [%]
		a	(001)	(001)	(001)
TiC_2	cubic	3,13	-13,30	-38,69	-69,35
NbC (α)	cubic	3,30	-8,55	-35,34	-67,67
$Ta/TaC_{0,03}$	cubic	3,31	-8,42	-35,24	-67,62
$GeNi_3C_{0,15}$	cubic	3,58	**-0,83**	-29,88	-64,94
$GaNi_3C_x$	cubic	3,60	**-0,36**	-29,54	-64,77
$Co_3GeC_{0,25}$	cubic	3,61	**0,00**	-29,29	-64,64
$(Cr_1Fe)_2C$	cubic	3,62	**0,28**	-29,09	-64,55
$AlNi_3C_{0,29}$	cubic	3,62	**0,28**	-29,09	-64,55
Ni_6Zn_3C	cubic	3,64	**0,83**	-28,70	-64,35
Co_3GaC_x	cubic	3,65	**1,02**	-28,56	-64,28
$Fe_3GeC_{0,45}$	cubic	3,66	**1,39**	-28,31	-64,15
$Ni_3ZnC_{0,7}$	cubic	3,66	**1,39**	-28,31	-64,15
T-$AlCo_3C_{0,59}$	cubic	3,70	**2,49**	-27,53	-63,76
Fe_6Al_2C	cubic	3,72	**3,05**	-27,13	-63,57
$AlFe_3C$	cubic	3,72	**3,05**	-27,13	-63,57
Co_3ZnC_1	cubic	3,73	**3,32**	-26,94	-63,47
$MgNi_3C$	cubic	3,73	**3,32**	-26,94	-63,47
Fe_3GaC_x	cubic	3,74	**3,60**	-26,74	-63,37
$AlFe_3C$	cubic	3,76	**4,10**	-26,39	-63,20
$Co_3SnC_{0,7}$	cubic	3,78	**4,71**	-25,96	-62,98
$InNi_3C_{0,5}$	cubic	3,79	**4,99**	-25,76	-62,88
Fe_3ZnC_x	cubic	3,81	5,54	-25,37	-62,69
Co_3MgC_x	cubic	3,82	5,82	-25,18	-62,59
$AlMn_3C$	cubic	3,83	6,09	-24,98	-62,49

$Co_3InC_{0,75}$	cubic	3,86	6,93	-24,39	-62,20
Fe_3SnC_1	cubic	3,86	6,93	-24,39	-62,20
$AlMn_3C$	cubic	3,87	7,17	-24,22	-62,11
$GeMn_3C$	cubic	3,87	7,20	-24,20	-62,10
$PbPt_3C_x$	cubic	3,88	7,34	-24,10	-62,05
Fe_3InC_x	cubic	3,88	7,48	-24,00	-62,00
$GaMn_3C$	cubic	3,88	7,59	-23,92	-61,96
Pt-Sn-C	cubic	3,89	7,76	-23,80	-61,90
$AlPt_3C_x$	cubic	3,89	7,84	-23,75	-61,87
$Mg_6Pt_{18}C$	cubic	3,90	8,14	-23,53	-61,77
Mn_3ZnC	cubic	3,92	8,72	-23,12	-61,56
$Mn_{3,15}Sn_{0,85}C$	cubic	3,97	9,89	-22,30	-61,15
$InPd_3C_x$	cubic	3,98	10,11	-22,14	-61,07
TcC	cubic	3,99	10,39	-21,94	-60,97
$InPt_3C_x$	cubic	3,99	10,47	-21,89	-60,94
ω-$ReWC_2$	cubic	4,06	12,55	-20,42	-60,21
$AlTi_3C$	cubic	4,16	15,12	-18,59	-59,30
VC_{1-x}	cubic	4,17	15,47	-18,35	-59,17
VC	cubic	4,17	15,51	-18,32	-59,16
$InTi_3C$	cubic	4,20	16,32	-17,75	-58,88
Ti_3TlC	cubic	4,21	16,59	-17,56	-58,78
MoC_{1-x}	cubic	4,27	18,28	-16,36	-58,18
W_2C	cubic	4,27	18,28	-16,36	-58,18
α-Mo_3C_2	cubic	4,28	18,59	-16,15	-58,07
TiC	cubic	4,32	19,67	-15,38	-57,69
Be_2C	cubic	4,33	19,94	-15,19	-57,59
AlY_3C	cubic	4,34	20,22	-14,99	-57,50
SiC	cubic	4,35	20,50	-14,79	-57,40
$(Sc_{0,25}Ti_{0,75})C$	cubic	4,38	21,33	-14,21	-57,10
Nb_3C/Nb_4C	cubic	4,40	21,88	-13,82	-56,91
γ-$TaC_{0,38}/TaC_{0,5}$	cubic	4,42	22,44	-13,42	-56,71
NbC	cubic	4,42	22,55	-13,35	-56,67
NbC (δ)	cubic	4,43	22,74	-13,21	-56,60
TaC	cubic	4,45	23,27	-12,84	-56,42
HfC	cubic	4,46	23,55	-12,64	-56,32
ScC	cubic	4,51	24,93	-11,66	-55,83
$HfC_{0,97}$	cubic	4,64	28,52	-9,12	-54,56
ZrC	cubic	4,70	30,16	-7,97	-53,98
PuC	cubic	4,91	36,01	**-3,83**	-51,91
UC	cubic	4,95	37,12	**-3,04**	-51,52
Lu_3C	cubic	4,97	37,53	**-2,75**	-51,37
NpC	cubic	5,00	38,61	**-1,98**	-50,99
Tm_3C	cubic	5,02	38,95	**-1,75**	-50,87
Er_3C	cubic	5,03	39,45	**-1,40**	-50,70
Ho_3C	cubic	5,06	40,19	**-0,87**	-50,43
Dy_3C	cubic	5,08	40,69	**-0,52**	-50,26

Tb_3C	cubic	5,11	41,47	**0,03**	-49,98
Gd_3C	cubic	5,13	41,99	**0,41**	-49,80
Y_3C	cubic	5,13	42,02	**0,42**	-49,79
Sm_3C	cubic	5,17	43,27	**1,31**	-49,35
ThC	cubic	5,34	47,92	**4,60**	-47,70
UC_2	cubic	5,48	51,66	7,24	-46,38
CaC_2 IV	cubic	5,58	54,57	9,30	-45,35
LaC_2 HT	cubic	6,00	66,20	17,52	-41,24
π-Cr-Fe-W-C	cubic	6,37	76,57	24,85	-37,57
Re_2W_3C	cubic	6,86	90,00	34,35	-32,82
Al_2Mo_3C	cubic	6,87	90,19	34,49	-32,76
Al_2Ta_3C	cubic	7,04	94,99	37,88	-31,06
Al_2Nb_3C	cubic	7,07	95,71	38,39	-30,81
Pu_2C_3	cubic	7,13	97,51	39,66	-30,17
U_2C_3	cubic	8,09	124,10	58,46	-20,77
Ho_2C_3	cubic	8,18	126,48	60,15	-19,93
Dy_2C_3	cubic	8,20	127,09	60,58	-19,71
Tb_2C_3	cubic	8,26	128,86	61,83	-19,09
Gd_2C_3	cubic	8,34	131,04	63,37	-18,31
Sm_2C_3	cubic	8,43	133,40	65,04	-17,48
Ce_2C_3	cubic	8,45	134,01	65,47	-17,27
Nd_2C_3	cubic	8,55	136,78	67,43	-16,29
Pr_2C_3	cubic	8,61	138,43	68,59	-15,70
La_2C_3	cubic	8,80	143,85	72,43	-13,79
$Fe_{21}W_2C_6$	cubic	10,54	191,97	106,45	**3,23**
Fe_6W_6C	cubic	10,54	191,97	106,45	**3,23**
$Fe_{21}Mo_2C_6$	cubic	10,56	192,52	106,84	**3,42**
$Mn_{23}C_6$	cubic	10,59	193,35	107,43	**3,72**
$Cr_{23}C_6$	cubic	10,64	194,74	108,41	**4,21**
Ni_5W_6C	cubic	10,87	201,19	112,97	6,49
Co_3W_3C	cubic	11,01	204,99	115,66	7,83
Mo_3Ni_3C	cubic	11,05	206,09	116,44	8,22
Fe_3W_3C	cubic	11,06	206,37	116,64	8,32
Fe_3Mo_3C	cubic	11,10	207,48	117,42	8,71
Mn_3Mo_3C	cubic	11,13	208,31	118,01	9,00
Mn_3W_3C	cubic	11,13	208,31	118,01	9,00
Co_2W_4C	cubic	11,21	210,53	119,58	9,79
Ni_3W_3	cubic	11,22	210,72	119,71	9,86
$Fe_3W_6C_2$	cubic	11,25	211,63	120,36	10,18
$Co_2W_6C_2$	cubic	11,25	211,63	120,36	10,18
$Ni_3W_6C_2$	cubic	11,25	211,63	120,36	10,18
Co_2Mo_4C	cubic	11,25	211,63	120,36	10,18
Mo_4Ni_2C	cubic	11,25	211,63	120,36	10,18
Fe_2Mo_4C	cubic	11,26	211,91	120,55	10,28
Cr_3Nb_3C	cubic	11,49	218,28	125,06	12,53
Ti_2ZnC_x	cubic	11,56	220,17	126,39	13,20

$CoNb_2(C,N,O)_x$	cubic	11,64	222,44	128,00	14,00
Nb_2ZnC_x	cubic	11,75	225,37	130,07	15,04
Hf_5Zn_3C	cubic	11,96	231,22	134,21	17,10
V_3Zr_3C	cubic	12,12	235,73	137,40	18,70
$ZnZr_2C_x$	cubic	12,16	236,84	138,18	19,09
$RuZr_2(C,N,O)_x$	cubic	12,30	240,72	140,93	20,46

7.9.2.2 Tetragonal structure

Tab. 7-12: Lattice dimension and lattice disregistry of examined carbides with tetragonal structure [40,41].

compound	crystallographic structure	lattice dimension [Å]		misfit [%]		rotation of planes, model 1, misfit [%]	rotation of planes, model 2, misfit [%]
		a	c	(001)	(100)	(001)	(001)
$UC_{2,3}$	tetragonal	3,51	5,97	**-2,77**	65,37	-31,25	-65,62
$UC_{0,4}$	tetragonal	3,54	5,97	**-1,94**	65,37	-30,66	-65,33
UC_2	tetragonal	3,55	6,00	**-1,66**	66,20	-30,46	-65,23
LuC_2	tetragonal	3,56	5,96	**-1,30**	65,21	-30,21	-65,10
TmC_2	tetragonal	3,60	6,05	**-0,28**	67,51	-29,49	-64,74
ErC_2	tetragonal	3,62	6,09	**0,28**	68,81	-29,09	-64,55
PuC_2	tetragonal	3,63	6,09	**0,55**	68,81	-28,90	-64,45
YbC_2	tetragonal	3,64	6,11	**0,75**	69,22	-28,76	-64,38
HoC_2	tetragonal	3,64	6,14	**0,91**	70,06	-28,64	-64,32
YC_2	tetragonal	3,66	6,17	**1,50**	70,89	-28,23	-64,12
TbC_2	tetragonal	3,69	6,22	**2,22**	72,22	-27,72	-63,86
GdC_2	tetragonal	3,72	6,28	**2,99**	73,82	-27,17	-63,59
SmC_2	tetragonal	3,77	6,33	**4,43**	75,37	-26,16	-63,08
Co_2Mn_2C	tetragonal	3,79	3,79	**4,99**	4,99	-25,76	-62,88
PrC_2	tetragonal	3,86	6,43	6,79	78,23	-24,49	-62,25
CaC_2 I	tetragonal	3,88	6,37	7,48	76,45	-24,00	-62,00
$GaPt_3C_x$	tetragonal	3,92	3,88	8,59	7,48	-23,22	-61,61
Mn_3ZnC	tetragonal	3,92	3,90	8,61	8,01	-23,20	-61,60
LaC_2	tetragonal	3,94	6,57	9,14	82,05	-22,83	-61,41
Pd_3SnC_x	tetragonal	4,09	3,80	13,19	5,26	-19,97	-59,98
SrC_2	tetragonal	4,12	6,69	14,13	85,32	-19,30	-59,65
EuC_2	tetragonal	4,95	6,65	36,98	84,07	**-3,14**	-51,57
$FeUC_2$	tetragonal	4,97	7,45	37,53	106,37	**-2,75**	-51,37
NdC_2	tetragonal	5,41	6,23	49,86	72,58	5,97	-47,02
PrC_2	tetragonal	5,44	6,38	50,69	76,73	6,56	-46,72
CaC_2	tetragonal	5,48	6,37	51,80	76,45	7,34	-46,33
CeC_2	tetragonal	5,48	6,48	51,80	79,50	7,34	-46,33
MgC_2	tetragonal	5,55	5,03	53,74	39,34	8,71	-45,64
SrC_2	tetragonal	5,81	6,68	60,94	85,04	13,80	-43,10

ThC_2	tetragonal	5,85	5,28	62,05	46,26	14,59	-42,71
BaC_2	tetragonal	6,22	7,06	72,30	95,57	21,83	-39,08
Mn_4C	tetragonal	7,66	10,57	112,19	192,80	50,04	-24,98
CaC_2 II	tetragonal	23,40	22,31	548,20	518,01	358,35	129,17

7.9.2.3 Hexagonal structure

7.9.2.3.1 (0001) plane

Tab. 7-13: Lattice dimension and lattice disregistry ((0001 plane) of examined carbides with hexagonal structure [40,41].

compound	crystallographic structure	lattice dimension [Å]		misfit [%]
		a	c	(0001)
$\delta TaC_{0,38}/TaC_{0,5}$	hcp	2,46	6,69	**-3,63**
Ni_3C	hcp	2,63	4,31	**2,95**
Fe_2C	hcp	2,76	4,35	8,12
V_6C	hcp	2,86	4,54	12,04
H-$AlCr_2C$	hcp	2,86	12,82	12,04
V_2C	hcp	2,88	4,57	12,98
Cr_2GaC	hcp	2,89	12,62	13,06
MoC (γ)	hcp	2,90	2,81	13,61
WC	hcp	2,90	2,83	13,61
OsC	hcp	2,91	2,82	13,90
RuC	hcp	2,91	2,82	13,91
AlV_2C	hcp	2,91	13,14	14,12
MoC (γ`)	hcp	2,93	10,97	14,78
GaV_2C	hcp	2,94	12,84	15,10
Cr_2GeC	hcp	2,95	12,08	15,72
W_2C	hcp	2,99	4,71	17,13
GeV_2C	hcp	3,00	12,25	17,56
Mo_2C	hcp	3,01	4,74	17,92
η-Mo_3C_2	hcp	3,01	14,64	18,03
$GaMo_2C$	hcp	3,02	13,18	18,19
$AlTi_2C$	hcp	3,04	13,60	19,09
$GaTi_2C$	hcp	3,06	13,31	20,03
$AlTa_2C$	hcp	3,08	13,83	20,46
$GeTi_2C$	hcp	3,08	12,93	20,62
Ta_2C	hcp	3,09	4,93	21,05
$CdTi_2C$	hcp	3,10	14,41	21,40
$\beta TaC_{0,38}/TaC_{0,5}$	hcp	3,10	4,94	21,48
H-$AlNb_2C$	hcp	3,10	13,83	21,56
$GaTa_2C$	hcp	3,10	13,57	21,60
NbC (β)	hcp	3,12	4,96	22,23

$GaNb_2C$	hcp	3,13	13,57	22,66
$InTi_2C$	hcp	3,13	14,06	22,70
Ti_2TlC	hcp	3,16	-12,52	23,71
$SnTi_2C$	hcp	3,16	13,67	23,91
$InNb_2C$	hcp	3,17	14,37	24,26
$PbTi_2C$	hcp	3,21	13,81	25,71
$S_2Ti_4C_2$	hcp	3,21	11,20	25,75
$Al_8C_3N_4$	hcp	3,21	55,08	25,79
$Al_7C_3N_3$	hcp	3,23	31,70	26,38
Nb_2SnC	hcp	3,25	13,77	27,12
$Al_6C_3N_2$	hcp	3,25	40,03	27,24
Al_5C_3N	hcp	3,28	21,67	28,53
Hf_2InC	hcp	3,31	14,73	29,55
Hf_2SnC	hcp	3,31	14,39	29,75
Hf_2TlC	hcp	3,32	14,63	30,14
Al_4C_3	hcp	3,33	24,95	30,45
$InZr_2C$	hcp	3,35	14,91	31,12
$SnZr_2C$	hcp	3,35	14,59	31,12
Hf_2PbC	hcp	3,36	14,47	31,55
$TlZr_2C$	hcp	3,36	14,79	31,75
$FeHf_2SC_2$	hcp	3,37	-6,79	31,82
$PbZr_2C$	hcp	3,38	14,67	32,57
$S_2Zr_4C_2$	hcp	3,40	12,11	33,04
εFeC	hcp	4,77	4,35	86,75
$\varepsilon Fe_{2\text{-}3}C$	hcp	4,77	4,35	86,75
RbC_8	hcp	4,93	22,78	92,98
KC_{16}	hcp	4,94	17,45	93,52
CsC_8	hcp	4,95	17,76	93,72
RbC_{16}	hcp	4,95	17,99	93,92
CsC_{16}	hcp	4,95	18,55	93,92
KC_8	hcp	4,95	21,39	93,92
KC_{16}	hcp	4,95	17,49	93,92
KC_8	hcp	4,97	21,35	94,70
B_4C	hcp	5,06	12,12	98,22
ScC_2	hcp	5,46	10,24	113,89
Fe_7C_3	hcp	6,88	4,54	169,60
$Cr_{5\text{-}x}Si_{3\text{-}y}C_{x+y}$	hcp	6,99	4,73	173,95
α-Al_4SiC_4	hcp	7,15	10,80	180,10
$Mo_{5\text{-}x}Si_{3\text{-}y}C_{x+y}$	hcp	7,28	5,06	185,19
$Co_3W_9C_4$	hcp	7,29	7,29	185,43
Mg_2C_3	hcp	7,45	10,61	191,85
$Ge_3Ta_5C_x$	hcp	7,59	5,22	197,18
$Ga_3Ta_5C_x$	hcp	7,66	5,28	200,12
$Ga_3Nb_5C_x$	hcp	7,72	5,27	202,43
χ Mn-W-C	hcp	7,76	7,76	203,84
$Ni_3W_{16}C_6$	hcp	7,82	7,82	206,28

$Fe_3W_{10}C_4$	hcp	7,85	7,85	207,52
$Co_3W_6C_2$	hcp	7,85	7,85	207,52
$Ni_3W_{10}C_4$	hcp	7,85	7,85	207,52
$Ge_3Hf_5C_x$	hcp	7,88	5,54	208,82
NaC_{64}	hcp	9,82	56,00	284,70
$Fe_{10}Si_2C_3$	hcp	11,70	10,80	358,35
Mn_7C_3	hcp	13,87	4,53	443,36
Mn_8C_3	hcp	13,90	4,55	444,53
Cr_7C_3	hcp	13,98	4,52	447,66

7.9.2.3.2 (10-10) plane

Tab. 7-14: Lattice dimension and lattice disregistry ((10-10) plane) of examined carbides with hexagonal structure [40,41].

compound	crystallographic structure	lattice dimension [Å]		misfit [%]	
		a	c	a	c
$\delta TaC_{0,38}/TaC_{0,5}$	hcp	2,46	6,69	-31,86	85,32
Ni_3C	hcp	2,63	4,31	-27,20	19,28
Fe_2C	hcp	2,76	4,35	-23,55	20,50
V_6C	hcp	2,86	4,54	-20,78	25,76
H-$AlCr_2C$	hcp	2,86	12,82	-20,78	255,12
V_2C	hcp	2,88	4,57	-20,11	26,54
Cr_2GaC	hcp	2,89	12,62	-20,06	249,47
MoC (γ)	hcp	2,90	2,81	-19,67	-22,16
WC	hcp	2,90	2,83	-19,67	-21,61
OsC	hcp	2,91	2,82	-19,46	-21,84
RuC	hcp	2,91	2,82	-19,45	-21,83
AlV_2C	hcp	2,91	13,14	-19,31	263,99
MoC (γ`)	hcp	2,93	10,97	-18,84	203,88
GaV_2C	hcp	2,94	12,84	-18,61	255,68
Cr_2GeC	hcp	2,95	12,08	-18,17	234,63
W_2C	hcp	2,99	4,71	-17,17	30,47
GeV_2C	hcp	3,00	12,25	-16,87	239,34
Mo_2C	hcp	3,01	4,74	-16,62	31,30
η-Mo_3C_2	hcp	3,01	14,64	-16,54	305,54
$GaMo_2C$	hcp	3,02	13,18	-16,43	265,10
$AlTi_2C$	hcp	3,04	13,60	-15,79	276,73
$GaTi_2C$	hcp	3,06	13,31	-15,12	268,56
$AlTa_2C$	hcp	3,08	13,83	-14,82	283,10
$GeTi_2C$	hcp	3,08	12,93	-14,71	258,17
Ta_2C	hcp	3,09	4,93	-14,40	36,57
$CdTi_2C$	hcp	3,10	14,41	-14,16	299,17
$\beta TaC_{0,38}/TaC_{0,5}$	hcp	3,10	4,94	-14,10	36,76

H-$AlNb_2C$	hcp	3,10	13,83	-14,04	283,10
$GaTa_2C$	hcp	3,10	13,57	-14,02	275,90
NbC (β)	hcp	3,12	4,96	-13,57	37,31
$GaNb_2C$	hcp	3,13	13,57	-13,27	275,76
$InTi_2C$	hcp	3,13	14,06	-13,24	289,47
Ti_2TlC	hcp	3,16	13,98	-12,52	287,26
$SnTi_2C$	hcp	3,16	13,67	-12,38	278,67
$InNb_2C$	hcp	3,17	14,37	-12,13	298,06
$PbTi_2C$	hcp	3,21	13,81	-11,11	282,55
$S_2Ti_4C_2$	hcp	3,21	11,20	-11,08	210,25
$Al_8C_3N_4$	hcp	3,21	55,08	-11,05	1425,76
$Al_7C_3N_3$	hcp	3,23	31,70	-10,64	778,12
Nb_2SnC	hcp	3,25	13,77	-10,11	281,44
$Al_6C_3N_2$	hcp	3,25	40,03	-10,03	1008,86
Al_5C_3N	hcp	3,28	21,67	-9,11	500,28
Hf_2InC	hcp	3,31	14,73	-8,39	308,03
Hf_2SnC	hcp	3,31	14,39	-8,25	298,61
Hf_2TlC	hcp	3,32	14,63	-7,98	305,26
Al_4C_3	hcp	3,33	24,95	-7,76	591,14
$InZr_2C$	hcp	3,35	14,91	-7,29	313,02
$SnZr_2C$	hcp	3,35	14,59	-7,29	304,16
Hf_2PbC	hcp	3,36	14,47	-6,98	300,83
$TlZr_2C$	hcp	3,36	14,79	-6,84	309,70
$FeHf_2SC_2$	hcp	3,37	11,99	-6,79	232,13
$PbZr_2C$	hcp	3,38	14,67	-6,26	306,37
$S_2Zr_4C_2$	hcp	3,40	12,11	-5,93	235,46
εFeC	hcp	4,77	4,35	32,05	20,61
$εFe_{2\text{-}3}C$	hcp	4,77	4,35	32,05	20,61
RbC_8	hcp	4,93	22,78	36,45	531,02
KC_{16}	hcp	4,94	17,45	36,84	383,38
CsC_8	hcp	4,95	17,76	36,98	391,97
RbC_{16}	hcp	4,95	17,99	37,12	398,34
CsC_{16}	hcp	4,95	18,55	37,12	413,85
KC_8	hcp	4,95	21,39	37,12	492,47
KC_{16}	hcp	4,95	17,49	37,12	384,49
KC_8	hcp	4,97	21,35	37,67	491,41
B_4C	hcp	5,06	12,12	40,17	235,73
ScC_2	hcp	5,46	10,24	51,25	183,66
Fe_7C_3	hcp	6,88	4,54	90,64	25,76
$Cr_{5\text{-}x}Si_{3\text{-}y}C_{x+y}$	hcp	6,99	4,73	93,71	30,91
α-Al_4SiC_4	hcp	7,15	10,80	98,06	199,17
$Mo_{5\text{-}x}Si_{3\text{-}y}C_{x+y}$	hcp	7,28	5,06	101,66	40,17
$Co_3W_9C_4$	hcp	7,29	7,29	101,83	101,83
Mg_2C_3	hcp	7,45	10,61	106,37	193,91
$Ge_3Ta_5C_x$	hcp	7,59	5,22	110,14	44,52
$Ga_3Ta_5C_x$	hcp	7,66	5,28	112,22	46,26

$Ga_3Nb_5C_x$	hcp	7,72	5,27	113,85	45,98
χ Mn-W-C	hcp	7,76	7,76	114,85	114,85
$Ni_3W_{16}C_6$	hcp	7,82	7,82	116,57	116,57
$Fe_3W_{10}C_4$	hcp	7,85	7,85	117,45	117,45
$Co_3W_6C_2$	hcp	7,85	7,85	117,45	117,45
$Ni_3W_{10}C_4$	hcp	7,85	7,85	117,45	117,45
$Ge_3Hf_5C_x$	hcp	7,88	5,54	118,37	53,38
NaC_{64}	hcp	9,82	56,00	172,02	1451,25
$Fe_{10}Si_2C_3$	hcp	11,70	10,80	224,10	199,17
Mn_7C_3	hcp	13,87	4,53	284,21	25,48
Mn_8C_3	hcp	13,90	4,55	285,04	26,04
Cr_7C_3	hcp	13,98	4,52	287,26	25,21

7.9.2.4 Orthorhombic structure

Tab. 7-15: Lattice dimension and lattice disregistry of examined carbides with orthorhombic structure [40,41].

compound	crystallographic structure	lattice dimension [Å]			misfit [%]		
		a	c	b	a	c	b
Co_2C	orthorhombic	2,91	4,43	4,47	-19,39	22,60	23,80
Co_3C	orthorhombic	4,48	6,73	5,03	24,18	86,45	39,42
Fe_3C	orthorhombic	4,52	6,72	5,09	25,21	86,15	41,00
Mn_7C_3	orthorhombic	4,55	11,98	6,96	25,93	231,83	92,77
Mn_3C	orthorhombic	5,08	4,53	6,77	40,72	25,48	87,59
Fe_3C	orthorhombic	5,09	4,52	6,74	40,97	25,30	86,80
$CrUC_2$	orthorhombic	5,43	10,64	3,23	50,50	194,65	-10,47
UWC_2	orthorhombic	5,63	10,98	3,26	56,07	204,16	-9,83
$Fe_{20}C_9$	orthorhombic	9,06	7,93	15,69	150,97	119,67	334,63
$Fe_{20}C_9$	orthorhombic	9,06	7,94	15,69	151,00	119,86	334,74
Cr_3C_2	orthorhombic	11,46	2,82	5,52	217,45	-21,88	52,91

7.9.3 Examined nitrides

7.9.3.1 Cubic structure

Tab. 7-16: Lattice dimension and lattice disregistry of examined nitrides with cubic structure [40,41].

compound	crystallographic structure	lattice dimension [Å]	misfit [%]	rotation of planes, model 1, misfit [%]	rotation of planes, model 2, misfit [%]
		a	(001)	(001)	(001)
Ni_4N I	cubic	3,72	**3,05**	-27,13	-63,57
Co_4N	cubic	3,74	**3,55**	-26,78	-63,39
$Co_{42,5}Zn_{42,5}N_{15}$	cubic	3,75	**3,88**	-26,55	-63,27
T Ni-Zn-N	cubic	3,75	**3,88**	-26,55	-63,27
Fe_3NiN	cubic	3,79	**4,99**	-25,76	-62,88
Fe_4N (γ´)	cubic	3,80	5,26	-25,57	-62,78
Al-Ni-N	cubic	3,80	5,26	-25,57	-62,78
Cu_3N	cubic	3,81	5,54	-25,37	-62,69
$Co_{63}Sn_{21}N_{16}$	cubic	3,82	5,82	-25,18	-62,59
$In_{21,9}Ni_{65,7}N1_{2,4}$	cubic	3,84	6,48	-24,71	-62,35
Mn_4N	cubic	3,85	6,65	-24,59	-62,29
Fe_3PtN	cubic	3,86	6,84	-24,45	-62,23
Co_3InN	cubic	3,86	6,93	-24,39	-62,20
Fe_3PdN	cubic	3,87	7,09	-24,27	-62,14
Cr_3GaN	cubic	3,88	7,35	-24,09	-62,04
$GaMn_3N$	cubic	3,90	7,98	-23,65	-61,82
Fe_3SnN	cubic	3,90	8,03	-23,61	-61,80
$CuMn_3N$	cubic	3,91	8,20	-23,49	-61,75
$ReN_{0,4}$	cubic	3,92	8,59	-23,22	-61,61
$Re_{2\text{-}3}N$	cubic	3,93	8,86	-23,02	-61,51
$TcN_{1\text{-}x}$	cubic	3,98	10,25	-22,04	-61,02
$AgMn_3N$	cubic	4,02	11,34	-21,27	-60,63
$VN_{0,71}$	cubic	4,07	12,74	-20,28	-60,14
W_2N (β)	cubic	4,12	14,13	-19,30	-59,65
W_2N (γ)	cubic	4,12	14,13	-19,30	-59,65
VN	cubic	4,13	14,40	-19,10	-59,55
$W_{0,75}(N,O)$	cubic	4,13	14,40	-19,10	-59,55
γ-Mo_3N_2	cubic	4,14	14,60	-18,97	-59,48
$W_{0,62}(N_{0,62}O_{0,38})$	cubic	4,14	14,63	-18,95	-59,47
CrN	cubic	4,14	14,68	-18,91	-59,45
$WN_{0,67\text{-}1}$	cubic	4,14	14,68	-18,91	-59,45
Mo_2N (γ)	cubic	4,17	15,51	-18,32	-59,16
$InTi_3N$	cubic	4,19	16,07	-17,93	-58,96
Ti_3TlN	cubic	4,19	16,09	-17,91	-58,95
TiN	cubic	4,24	17,45	-16,95	-58,47

$NbN_{0,9}N_{0,1}$	cubic	4,37	21,14	-14,34	-57,17
Ag_3N	cubic	4,38	21,27	-14,25	-57,12
NbN (1)	cubic	4,38	21,33	-14,21	-57,10
ScN	cubic	4,44	22,99	-13,03	-56,52
HfN	cubic	4,52	25,15	-11,50	-55,75
$Zr_{1-x}N$	cubic	4,55	26,04	-10,88	-55,44
ZrN_{1-x}	cubic	4,58	26,79	-10,35	-55,17
ZrN	cubic	4,63	28,25	-9,31	-54,66
$Li_9SiN_3O_2$	cubic	4,68	29,64	-8,33	-54,17
$CrLi_9N_5$	cubic	4,74	31,27	-7,18	-53,59
$GeLi_9N_3O_2$	cubic	4,75	31,58	-6,96	-53,48
$Li_9TiN_3O_2$	cubic	4,76	31,86	-6,76	-53,38
LuN	cubic	4,77	32,02	-6,65	-53,32
YbN	cubic	4,79	32,55	-6,27	-53,14
TmN	cubic	4,81	33,21	-5,80	-52,90
ErN	cubic	4,84	33,96	-5,28	-52,64
HoN	cubic	4,88	35,10	**-4,47**	-52,24
YN	cubic	4,88	35,10	**-4,47**	-52,24
UN	cubic	4,89	35,46	**-4,22**	-52,11
NpN	cubic	4,89	35,46	**-4,22**	-52,11
ZnLiN	cubic	4,89	35,46	**-4,22**	-52,11
DyN	cubic	4,89	35,57	**-4,14**	-52,07
PuN	cubic	4,90	35,73	**-4,02**	-52,01
TbN	cubic	4,94	36,73	**-3,32**	-51,66
LiMgN	cubic	4,98	37,95	**-2,45**	-51,23
GdN	cubic	4,99	38,23	**-2,26**	-51,13
EuN	cubic	5,01	38,70	**-1,93**	-50,96
CeN	cubic	5,01	38,78	**-1,87**	-50,93
SmN	cubic	5,05	39,84	**-1,12**	-50,56
NdN	cubic	5,14	42,38	**0,68**	-49,66
PrN	cubic	5,16	42,94	**1,07**	-49,46
ThN	cubic	5,20	44,04	**1,85**	-49,07
LaN	cubic	5,28	46,26	**3,42**	-48,29
UN_2	cubic	5,32	47,37	**4,21**	-47,90
$Fe_7Mo_{13}N_4$	cubic	6,69	85,45	31,13	-34,43
Be_3N_2	cubic	8,13	125,21	59,25	-20,38
$SiLi_5N_3$	cubic	9,43	161,22	84,71	-7,65
Li_5SiN_3	cubic	9,44	161,39	84,83	-7,59
$AlLi_3N_2$	cubic	9,48	162,60	85,69	-7,16
Li_7MnN_4	cubic	9,57	165,12	87,47	-6,26
Li_7VN_4	cubic	9,60	166,04	88,12	-5,94
$GaLi_3N_2$	cubic	9,61	166,20	88,24	-5,88
$GeLi_5N_3$	cubic	9,66	167,59	89,21	-5,39
$TiLi_5N_3$	cubic	9,73	169,53	90,59	**-4,71**
Zn_3N_2	cubic	9,76	170,44	91,23	**-4,38**
Mg_3N_2	cubic	9,95	175,62	94,90	**-2,55**

$Ta_{27}N$	cubic	10,11	180,06	98,03	**-0,99**
U_2N_3	cubic	10,70	196,37	109,57	**4,78**
Cd_3N_2	cubic	10,79	198,89	111,35	5,67
Fe_3Mo_3N	cubic	11,07	206,51	116,74	8,37
Ca_3N_2 (α)	cubic	11,40	215,79	123,30	11,65
Ti_2ZnN_x	cubic	11,50	218,45	125,18	12,59
T Hg-Mn-N	cubic	11,51	218,95	125,53	12,76
Nb_2ZnN_x	cubic	11,55	219,86	126,18	13,09
$Hf_2Zn_2N_x$	cubic	11,97	231,47	134,38	17,19
$ZnZr_2N_x$	cubic	12,13	236,04	137,62	18,81

7.9.3.2 Tetragonal structure

Tab. 7-17: Lattice dimension and lattice disregistry of examined carbides with orthorhombic structure [40,41].

compound	crystallographic structure	lattice dimension [Å]		misfit [%]		rotation of planes, model 1, misfit [%]	rotation of planes, model 2, misfit [%]
		a	c	(001)	(100)	(001)	(001)
FeNiN	tetragonal	2,83	3,71	-21,61	2,85	-44,57	-72,28
α´-FeN	tetragonal	2,84	3,10	-21,22	-14,13	-44,29	-72,15
VN	tetragonal	2,97	3,40	-17,73	-5,96	-41,83	-70,91
Ni_4N II	tetragonal	3,72	7,28	**3,05**	101,66	-27,13	-63,57
Mo_2N (β)	tetragonal	4,18	4,02	15,79	11,36	-18,12	-59,06
Mn_3N_2	tetragonal	4,19	4,03	16,07	11,63	-17,93	-58,96
β-$MoN_{0,4}$	tetragonal	4,20	8,01	16,34	121,88	-17,73	-58,87
Mn_5N_6	tetragonal	4,22	4,14	16,81	14,60	-17,40	-58,70
$NbN_{0,6}O_{0,2}$	tetragonal	4,37	4,30	21,05	18,98	-14,40	-57,20
$NbN_{0,75}$	tetragonal	4,38	8,68	21,33	140,44	-14,21	-57,10
Ti_2N	tetragonal	4,94	3,04	36,92	-15,91	**-3,18**	-51,59
α´´-$Fe_{16}N_2$	tetragonal	5,72	6,29	58,45	74,29	12,04	-43,98

7.9.3.3 Hexagonal structure

7.9.3.3.1 (0001) plane

Tab. 7-18: Lattice dimension and lattice disregistry ((0001) plane) of examined nitrides with hexagonal structure [40,41].

compound	crystallographic structure	lattice dimension [Å]		misfit [%]
		a	c	(0001)
BN	hcp	2,50	6,66	**-2,06**
Fe_4N (ε)	hcp	2,66	4,34	**4,21**
Co_3N	hcp	2,66	4,35	**4,21**
Ni_3N	hcp	2,67	4,31	**4,60**
Fe_3N (ε)	hcp	2,72	4,39	6,56
Cr_2N	hcp	2,76	4,46	8,12
Fe_2N (ε)	hcp	2,76	4,43	8,12
ε-$Fe_{2-3}N$	hcp	2,77	4,42	8,44
Mn_2N	hcp	2,82	4,53	10,32
$VN_{0,4}$	hcp	2,84	4,55	11,26
β-Be_3N_2	hcp	2,84	9,69	11,31
MoN	hcp	2,86	2,80	12,04
$Mo_{0,84}N$	hcp	2,86	11,20	12,04

$W_{1,35\text{-}1,15}N$	hcp	2,89	15,46	13,02
W-N	hcp	2,89	30,92	13,02
W_2N hex	hcp	2,89	22,85	13,22
$W_{1,17}N$	hcp	2,89	23,35	13,22
$W_{2,56}N_4$	hcp	2,89	11,00	13,22
$W_{0,6}N$	hcp	2,89	10,80	13,22
W_3N_6	hcp	2,89	16,40	13,22
WN	hcp	2,89	2,83	13,33
NbN (2)	hcp	2,93	5,45	14,78
$TaN_{0,8\text{-}0,9}$	hcp	2,94	2,88	15,10
$(Co_{0,3}Ti_{0,7})N$	hcp	2,94	2,90	15,17
$(Ni_{0,3}Ti_{0,7})N$	hcp	2,94	2,89	15,17
NbN (3)	hcp	2,95	11,25	15,57
$NbN_{0,8\text{-}0,9}$	hcp	2,95	2,77	15,57
$AlTi_2N$	hcp	2,99	13,61	17,29
$GaTi_2N$	hcp	3,00	13,30	17,68
$MnTa_3N_4$	hcp	3,02	10,49	18,43
Ta_2N	hcp	3,05	4,92	19,39
Nb_2N	hcp	3,05	4,96	19,48
$Ta_2N_{0,38}O_{0,65}$	hcp	3,06	4,93	19,68
Ta_2N	hcp	3,06	4,96	19,88
$InTi_2N$	hcp	3,07	13,98	20,42
AlN	hcp	3,10	4,97	21,44
GaN	hcp	3,18	5,17	24,58
$InZr_2N$	hcp	3,28	14,84	28,38
Al_5C_3N	hcp	3,28	21,55	28,49
InN	hcp	3,53	5,69	38,29
Ca_3N_2 (β)	hcp	3,55	4,11	39,07
TaZrNO	hcp	3,65	3,88	42,79
Li_3N	hcp	3,66	3,88	43,38
$CuLi_2N$	hcp	3,68	3,77	44,16
$CoLi_2N$	hcp	3,74	3,62	46,51
$NiLi_2N$	hcp	3,77	3,52	47,69
Th_2N_3	hcp	3,88	6,18	52,00
Si_xN	hcp	4,53	4,56	77,62
Co_3N	hcp	4,61	4,35	80,44
ε-$Fe_{2\text{-}3}N$	hcp	4,79	4,42	87,53
$VN_{0,37\text{-}0,43}$	hcp	4,91	4,54	92,47
$FeTa_2N_{2,6}$	hcp	5,16	10,31	101,99
$CoTa_2N_{2,5}$	hcp	5,16	10,30	102,18
$NiTa_2N_{2,45}$	hcp	5,17	10,36	102,46
TaN	hcp	5,18	2,90	103,00
$Ge_{24,3}Mn_{72,9}N_{2,8}$	hcp	5,60	4,52	119,38
δ´´-MoN	hcp	5,67	5,52	121,93
δ´-MoN	hcp	5,72	5,60	124,08
δ-MoN	hcp	5,73	5,61	124,28

$TaN_{0,5}O_{0,5}$	hcp	5,94	2,87	132,66
(β) Si_3N_4	hcp	7,60	2,91	197,85
β-Si_3N_4	hcp	7,61	2,91	198,04
α-Si_3N_4	hcp	7,75	5,62	203,53
(α) Si_3N_4	hcp	7,76	5,62	203,92
β-Ge_3N_4	hcp	8,04	3,07	214,89
ε-$Fe_{2-3}N$	hcp	9,47	4,40	270,91
$TaN_{0,9}O_{0,1}$	hcp	10,34	5,80	305,07
$TaN_{0,65}O_{0,35}$	hcp	10,34	2,86	305,07

7.9.3.3.2 (10-10) plane

Tab. 7-19: Lattice dimension and lattice disregistry ((10-10) plane) of examined nitrides with hexagonal structure [40,41].

compound	crystallographic structure	lattice dimension [Å]		misfit [%]	
		a	c	a	c
BN	hcp	2,50	6,66	-30,75	84,49
Fe_4N (ε)	hcp	2,66	4,34	-26,32	20,22
Co_3N	hcp	2,66	4,35	-26,32	20,50
Ni_3N	hcp	2,67	4,31	-26,04	19,39
Fe_3N (ε)	hcp	2,72	4,39	-24,65	21,61
Cr_2N	hcp	2,76	4,46	-23,55	23,55
Fe_2N (ε)	hcp	2,76	4,43	-23,55	22,71
ε-$Fe_{2-3}N$	hcp	2,77	4,42	-23,32	22,35
Mn_2N	hcp	2,82	4,53	-21,99	25,61
$VN_{0,4}$	hcp	2,84	4,55	-21,33	26,04
β-Be_3N_2	hcp	2,84	9,69	-21,29	168,50
MoN	hcp	2,86	2,80	-20,78	-22,44
$Mo_{0,84}N$	hcp	2,86	11,20	-20,78	210,25
$W_{1,35-1,15}N$	hcp	2,89	15,46	-20,08	328,25
W-N	hcp	2,89	30,92	-20,08	756,51
W_2N hex	hcp	2,89	22,85	-19,94	532,96
$W_{1,17}N$	hcp	2,89	23,35	-19,94	546,81
$W_{2,56}N_4$	hcp	2,89	11,00	-19,94	204,71
$W_{0,6}N$	hcp	2,89	10,80	-19,94	199,17
W_3N_6	hcp	2,89	16,40	-19,94	354,29
WN	hcp	2,89	2,83	-19,86	-21,72
NbN (2)	hcp	2,93	5,45	-18,84	50,97
$TaN_{0,8-0,9}$	hcp	2,94	2,88	-18,61	-20,14
$(Co_{0,3}Ti_{0,7})N$	hcp	2,94	2,90	-18,56	-19,67
$(_{Ni0,3}Ti_{0,7})N$	hcp	2,94	2,89	-18,56	-19,94
NbN (3)	hcp	2,95	11,25	-18,28	211,63
$NbN_{0,8-0,9}$	hcp	2,95	2,77	-18,28	-23,21

$AlTi_2N$	hcp	2,99	13,61	-17,06	277,01
$GaTi_2N$	hcp	3,00	13,30	-16,79	268,42
$MnTa_3N_4$	hcp	3,02	10,49	-16,26	190,58
Ta_2N	hcp	3,05	4,92	-15,58	36,25
Nb_2N	hcp	3,05	4,96	-15,51	37,40
$Ta_2N_{0,38}O_{0,65}$	hcp	3,06	4,93	-15,37	36,51
Ta_2N	hcp	3,06	4,96	-15,24	37,40
$InTi_2N$	hcp	3,07	13,98	-14,85	287,12
AlN	hcp	3,10	4,97	-14,13	37,67
GaN	hcp	3,18	5,17	-11,91	43,21
$InZr_2N$	hcp	3,28	14,84	-9,22	311,08
Al_5C_3N	hcp	3,28	21,55	-9,14	496,95
InN	hcp	3,53	5,69	-2,22	57,62
Ca_3N_2 (β)	hcp	3,55	4,11	-1,66	13,85
TaZrNO	hcp	3,65	3,88	0,97	7,51
Li_3N	hcp	3,66	3,88	1,39	7,48
$CuLi_2N$	hcp	3,68	3,77	**1,94**	**4,43**
$CoLi_2N$	hcp	3,74	3,62	**3,60**	**0,28**
$NiLi_2N$	hcp	3,77	3,52	**4,43**	**-2,49**
Th_2N_3	hcp	3,88	6,18	7,48	71,19
Si_xN	hcp	4,53	4,56	25,60	26,20
Co_3N	hcp	4,61	4,35	27,59	20,39
ε-$Fe_{2-3}N$	hcp	4,79	4,42	32,60	22,38
$VN_{0,37-0,43}$	hcp	4,91	4,54	36,09	25,79
$FeTa_2N_{2,6}$	hcp	5,16	10,31	42,83	185,60
$CoTa_2N_{2,5}$	hcp	5,16	10,30	42,96	185,32
$NiTa_2N_{2,45}$	hcp	5,17	10,36	43,16	186,98
TaN	hcp	5,18	2,90	43,55	-19,61
$Ge_{24,3}Mn_{72,9}N_{2,8}$	hcp	5,60	4,52	55,12	25,21
δ´´-MoN	hcp	5,67	5,52	56,93	52,91
δ´-MoN	hcp	5,72	5,60	58,45	55,12
δ-MoN	hcp	5,73	5,61	58,59	55,35
$TaN_{0,5}O_{0,5}$	hcp	5,94	2,87	64,52	-20,61
(β) Si_3N_4	hcp	7,60	2,91	110,61	-19,42
β-Si_3N_4	hcp	7,61	2,91	110,75	-19,37
α-Si_3N_4	hcp	7,75	5,62	114,63	55,60
(α) Si_3N_4	hcp	7,76	5,62	114,90	55,76
β-Ge_3N_4	hcp	8,04	3,07	122,66	-14,85
ε-$Fe_{2-3}N$	hcp	9,47	4,40	162,27	21,79
$TaN_{0,9}O_{0,1}$	hcp	10,34	5,80	186,43	60,72
$TaN_{0,65}O_{0,35}$	hcp	10,34	2,86	186,43	-20,66

7.9.3.4 Orthorhombic structure

Tab. 7-20: Lattice dimension and lattice disregistry of examined nitrides with orthorhombic structure [40,41].

compound	crystallographic structure	lattice dimension [Å]			misfit [%]		
		a	c	b	a	c	b
Co_2N	orthorhombic	2,84	4,33	4,63	-21,33	19,94	28,25
$BeSiN_2$	orthorhombic	4,98	4,67	5,75	37,95	29,36	59,28
Si_2ON	orthorhombic	5,50	4,85	8,88	52,30	34,43	145,90
Fe_2N (ξ)	orthorhombic	5,52	4,43	4,83	52,91	22,71	33,80
Si_3N_4	orthorhombic	13,38	7,74	8,60	270,64	114,40	138,23
Ge_3N_4	orthorhombic	13,84	8,18	9,06	283,38	126,59	150,97

7.9.4 Examined phosphides

7.9.4.1 Cubic structure

Tab. 7-21: Lattice dimension and lattice disregistry of examined phosphides with cubic structure [40,41].

compound	crystallographic structure	lattice dimension [Å]	misfit [%]	rotation of planes, model 1, misfit [%]	rotation of planes, model 2, misfit [%]
		a	(001)	(001)	(001)
AlP	cubic	5,42	50,14	6,16	-46,92
GaP	cubic	5,44	50,69	6,56	-46,72
Rh_2P	cubic	5,51	52,63	7,93	-46,04
Ir_2P	cubic	5,54	53,46	8,51	-45,74
UP	cubic	5,59	54,85	9,49	-45,25
PtP_2	cubic	5,68	57,34	11,26	-44,37
ZnLiP	cubic	5,77	59,83	13,02	-43,49
Th_4P_3	cubic	5,82	61,22	14,00	-43,00
NdP	cubic	5,83	61,50	14,19	-42,90
PrP	cubic	5,86	62,33	14,78	-42,61
InP	cubic	5,86	62,33	14,78	-42,61
CeP	cubic	5,90	63,43	15,57	-42,22
LaP	cubic	6,01	66,48	17,72	-41,14
MgLiP	cubic	6,02	66,84	17,98	-41,01
U_3P_4	cubic	8,20	127,15	60,62	-19,69
Th_3P_4	cubic	8,60	138,23	68,45	-15,77
Ni_7P_3	cubic	8,63	139,06	69,04	-15,48
Be_3P_2	cubic	10,15	181,16	98,81	**-0,59**
Mg_3P_2	cubic	12,01	232,69	135,25	17,62

7.9.4.2 Tetragonal structure

Tab. 7-22: Lattice dimension and lattice disregistry of examined phosphides with tetragonal structure [40,41].

compound	crystallographic structure	lattice dimension [Å]		misfit [%]		rotation of planes, model 1, misfit [%]	rotation of planes, model 2, misfit [%]
		a	c	(001)	(100)	(001)	(001)
ZnP_2	tetragonal	5,07	18,65	40,44	416,62	265,31	82,65
CdP_2	tetragonal	5,28	19,70	46,26	445,71	285,87	92,94
Zn_3P_2	tetragonal	8,10	11,45	124,38	217,17	124,28	12,14
Cd_3P_2	tetragonal	8,75	12,28	142,38	240,17	140,53	20,27

7.9.4.3 Hexagonal structure

7.9.4.3.1 (0001) plane

Tab. 7-23: Lattice dimension and lattice disregistry ((0001) plane) of examined phosphides with hexagonal structure [40,41].

compound	crystallographic structure	lattice dimension [Å]		misfit [%]
		a	c	(0001)
Li_3P	hcp	4,26	7,58	66,89
Na_3P	hcp	4,98	8,80	95,09
Ni_2P	hcp	5,85	3,37	129,17
Fe_2P	hcp	5,93	3,45	132,31
Mn_2P	hcp	6,07	3,45	137,79
Cu_3P	hcp	6,94	7,14	171,87

7.9.4.3.2 (10-10) plane

Tab. 7-24: Lattice dimension and lattice disregistry ((10-10) plane) of examined phosphides with hexagonal structure [40,41].

compound	crystallographic structure	lattice dimension [Å]		misfit [%]	
		a	c	a	c
Li_3P	hcp	4,26	7,58	18,01	109,97
Na_3P	hcp	4,98	8,80	37,95	143,77
Ni_2P	hcp	5,85	3,37	62,05	-6,65
Fe_2P	hcp	5,93	3,45	64,27	-4,43
Mn_2P	hcp	6,07	3,45	68,14	-4,43
Cu_3P	hcp	6,94	7,14	92,24	97,78

7.9.4.4 Orthorhombic structure

Tab. 7-25: Lattice dimension and lattice disregistry of examined phosphides with orthorhombic structure [40,41].

compound	crystallographic structure	lattice dimension [Å]			misfit [%]		
		a	c	b	a	c	b
FeP_2	orthorhombic	2,73	5,66	4,98	-24,38	56,79	37,95
CoP	orthorhombic	5,59	3,27	5,07	54,85	-9,42	40,44
FeP	orthorhombic	5,78	3,09	5,18	60,11	-14,40	43,49
MnP	orthorhombic	5,91	3,17	5,25	63,71	-12,19	45,43
CrP	orthorhombic	5,93	3,12	5,36	64,27	-13,57	48,48
Co_2P	orthorhombic	6,66	3,53	5,71	84,49	-2,22	58,17
$AlLi_3P_2$	orthorhombic	11,47	11,73	11,61	217,73	224,93	221,61

7.9.5 Examined sulphides

7.9.5.1 Cubic structure

Tab. 7-26: Lattice dimension and lattice disregistry of examined sulphides with cubic structure [40,41].

compound	crystallographic structure	lattice dimension [Å]	misfit [%]	rotation of planes, model 1, misfit [%]	rotation of planes, model 2, misfit [%]
		a	(001)	(001)	(001)
BeS	cubic	4,86	34,63	**-4,81**	-52,40
Ag_2S	cubic	4,88	35,18	**-4,41**	-52,21
Ga_2S_3 (α)	cubic	5,18	43,49	**1,46**	-49,27
MgS	cubic	5,19	43,77	**1,66**	-49,17
MnS	cubic	5,21	44,32	**2,05**	-48,97
(Fe, Ge)Cu_3S_4	cubic	5,29	46,54	**3,62**	-48,19
In_2S_3 (α)	cubic	5,37	48,75	5,18	-47,41
Cu_3VS_4	cubic	5,38	49,03	5,38	-47,31
FeS_2	cubic	5,40	49,58	5,77	-47,11
ZnS	cubic	5,40	49,58	5,77	-47,11
US	cubic	5,47	51,52	7,14	-46,43
Cu_5FeS_4	cubic	5,49	52,08	7,54	-46,23
CoS_2	cubic	5,52	52,91	8,12	-45,94
PuS	cubic	5,53	53,19	8,32	-45,84
$Cu_{1,8}S$	cubic	5,56	54,02	8,91	-45,55
RhS_2	cubic	5,57	54,29	9,10	-45,45
RuS_2	cubic	5,59	54,85	9,49	-45,25
MnS	cubic	5,60	55,12	9,69	-45,16
CoAsS	cubic	5,61	55,40	9,89	-45,06
OsS_2	cubic	5,64	56,23	10,47	-44,76
$AgBiS_2$	cubic	5,65	56,45	10,63	-44,69
NiAsS	cubic	5,66	56,79	10,86	-44,57
ThS	cubic	5,67	57,06	11,06	-44,47
NiS_2	cubic	5,68	57,34	11,26	-44,37
CaS	cubic	5,69	57,62	11,45	-44,27
Li_2S	cubic	5,71	58,17	11,84	-44,08
$NaBiS_2$	cubic	5,76	59,56	12,82	-43,59
CeS	cubic	5,77	59,83	13,02	-43,49
CdS	cubic	5,81	60,94	13,80	-43,10
HgS	cubic	5,84	61,77	14,39	-42,80
NiSbS	cubic	5,90	63,43	15,57	-42,22
PbS	cubic	5,92	63,99	15,96	-42,02
DyS	cubic	5,96	65,10	16,74	-41,63
SrS	cubic	6,01	66,48	17,72	-41,14
$KBiS_2$	cubic	6,01	66,48	17,72	-41,14

MnS_2	cubic	6,10	68,98	19,48	-40,26
BaS	cubic	6,37	76,45	24,77	-37,61
Na_2S	cubic	6,53	80,89	27,91	-36,05
K_2S	cubic	7,39	104,71	44,75	-27,62
Rb_2S	cubic	7,65	111,91	49,84	-25,08
Am_2S_3	cubic	8,43	133,52	65,12	-17,44
Pu_2S_3	cubic	8,44	133,80	65,32	-17,34
Ce_3S_4	cubic	8,61	138,45	68,61	-15,70
Ce_2S_3	cubic	8,62	138,70	68,79	-15,61
La_2S_3	cubic	8,71	141,27	70,61	-14,70
Ac_2S_3	cubic	8,97	148,48	75,70	-12,15
Co_3S_4	cubic	9,38	159,83	83,73	-8,13
Ni_2FeS_4	cubic	9,45	161,77	85,10	-7,45
Ni_3S_4	cubic	9,46	162,05	85,30	-7,35
$CuCo_2S_4$	cubic	9,46	162,05	85,30	-7,35
$ZnCrS_4$	cubic	9,90	174,24	93,92	**-3,04**
Co_9S_8	cubic	9,91	174,52	94,11	**-2,94**
$CoCr_2S_4$	cubic	9,91	174,52	94,11	**-2,94**
$ZnAl_2S_4$	cubic	9,97	176,18	95,29	**-2,36**
$FeCr_2S_4$	cubic	9,99	176,70	95,66	**-2,17**
$MnCr_2S_4$	cubic	10,06	178,67	97,05	**-1,48**
$(Ni,Fe)_9S_8$	cubic	10,10	179,78	97,83	**-1,08**
$CdCr_2S_4$	cubic	10,19	182,27	99,60	**-0,20**
$(Cu, Fe)_3AsS_3$	cubic	10,20	182,55	99,79	**-0,10**
$(Cu,Fe)_3,(Sb,As)S_3$	cubic	10,20	182,55	99,79	**-0,10**
$HgCr_2S_4$	cubic	10,21	182,83	99,99	**-0,01**
In_2NiS_4	cubic	10,46	189,75	104,88	**2,44**
In_2CoS_4	cubic	10,56	192,52	106,84	**3,42**
In_2FeS_4	cubic	10,60	193,63	107,63	**3,81**
In_2MgS_4	cubic	10,69	196,12	109,39	**4,69**
In_2MnS_4	cubic	10,69	196,12	109,39	**4,69**
In_2S_3 (β)	cubic	10,74	197,51	110,37	5,18
In_2BeS_4	cubic	10,77	198,34	110,96	5,48
In_2CaS_4	cubic	10,77	198,34	110,96	5,48
$CdMg_2S_4$	cubic	10,80	199,17	111,54	5,77
In_2HgS_4	cubic	10,81	199,45	111,74	5,87

7.9.5.2 Tetragonal structure

Tab. 7-27: Lattice dimension and lattice disregistry of examined sulphides with tetragonal structure [40,41].

compound	crystallographic structure	lattice dimension [Å]		misfit [%]		rotation of planes, model 1, misfit [%]	rotation of planes, model 2, misfit [%]
		a	c	(001)	(100)	(001)	(001)
PtS	tetragonal	4,91	6,10	36,01	68,98	**-3,83**	-51,91
$CuFeS_2$	tetragonal	5,24	10,30	45,15	185,32	**2,64**	-48,68
$SnCu_2FeS_4$	tetragonal	5,46	10,28	51,25	184,76	6,95	-46,53
$AgFeS_2$	tetragonal	5,66	10,30	56,79	185,32	10,86	-44,57
(Pt,Ni, Pd)S	tetragonal	6,37	6,58	76,45	82,27	24,77	-37,61
PdS	tetragonal	6,43	6,63	78,12	83,66	25,95	-37,03
TlS	tetragonal	7,79	6,80	115,79	88,37	52,59	-23,71

7.9.5.3 Hexagonal structure

7.9.5.3.1 (0001) plane

Tab. 7-28: Lattice dimension and lattice disregistry ((0001) plane) of examined sulphides with hexagonal structure [40,41].

compound	crystallographic structure	lattice dimension [Å]		misfit [%]
		a	c	(0001)
MoS_2	hcp	3,15	12,30	23,40
WS_2	hcp	3,15	12,30	23,40
VS	hcp	3,36	5,81	31,63
CoS	hcp	3,37	5,18	32,02
TiS_2	hcp	3,40	5,69	33,19
TaS_2	hcp	3,40	5,90	33,19
NiS	hcp	3,43	5,33	34,37
FeS (a´´) LT	hcp	3,44	5,79	34,76
FeS (β) LT	hcp	3,44	5,74	34,76
$Fe_{2-x}S_2$	hcp	3,44	5,82	34,76
FeS	hcp	3,44	5,88	34,92
FeS	hcp	3,45	5,76	35,04
CrS	hcp	3,45	5,75	35,15
$CrNaS_2$	hcp	3,51	19,57	37,50
PtS_2	hcp	3,54	5,02	38,68
$AlsS_3$	hcp	3,58	5,83	40,21
$CrRbS_2$	hcp	3,59	16,20	40,64
$CrKS_2$	hcp	3,62	21,16	41,81

SnS_2	hcp	3,64	5,87	42,60
ZrS_2	hcp	3,68	5,85	44,16
Ga_2S_3 (β)	hcp	3,69	6,03	44,56
CuS	hcp	3,75	16,20	46,91
$ZnAl_2S_4$	hcp	3,76	6,13	47,30
ZnS	hcp	3,81	6,23	49,30
MnS	hcp	3,98	6,43	55,92
Ni_3S_2	hcp	4,04		58,27
CdS	hcp	4,13	6,69	61,79
HgS	hcp	4,14	9,49	62,18
FeS (a´) LT	hcp	5,96	11,74	133,48
NiS	hcp	9,59	3,15	275,69
Th_7S_{12}	hcp	11,04	3,98	332,49
CrS	hcp	12,00	11,52	370,10
Tl_2S	hcp	12,20	18,17	377,93

7.9.5.3.2 (10-10) plane

Tab. 7-29: Lattice dimension and lattice disregistry ((10-10) plane) of examined sulphides with hexagonal structure [40,41].

compound	crystallographic structure	lattice dimension [Å]		misfit [%]	
		a	c	a	c
MoS_2	hcp	3,15	12,30	-12,74	240,72
WS_2	hcp	3,15	12,30	-12,74	240,72
VS	hcp	3,36	5,81	-6,93	60,94
CoS	hcp	3,37	5,18	-6,65	43,49
TiS_2	hcp	3,40	5,69	-5,82	57,62
TaS_2	hcp	3,40	5,90	-5,82	63,43
NiS	hcp	3,43	5,33	-4,99	47,65
FeS (a´´) LT	hcp	3,44	5,79	-4,71	60,39
FeS (β) LT	hcp	3,44	5,74	-4,71	59,00
$Fe_{2-x}S_2$	hcp	3,44	5,82	-4,71	61,22
FeS	hcp	3,44	5,88	-4,60	62,77
FeS	hcp	3,45	5,76	-4,52	59,58
CrS	hcp	3,45	5,75	-4,43	59,28
$CrNaS_2$	hcp	3,51	19,57	-2,77	442,11
PtS_2	hcp	3,54	5,02	-1,94	39,06
$AlsS_3$	hcp	3,58	5,83	-0,86	61,47
$CrRbS_2$	hcp	3,59	16,20	-0,55	348,75
$CrKS_2$	hcp	3,62	21,16	0,28	486,15
SnS_2	hcp	3,64	5,87	0,83	62,60
ZrS_2	hcp	3,68	5,85	1,94	62,05
Ga_2S_3 (β)	hcp	3,69	6,03	2,22	67,04

CuS	hcp	3,75	16,20	3,88	348,75
$ZnAl_2S_4$	hcp	3,76	6,13	4,16	69,81
ZnS	hcp	3,81	6,23	5,57	72,58
MnS	hcp	3,98	6,43	10,25	78,12
Ni_3S_2	hcp	4,04		11,91	-100,00
CdS	hcp	4,13	6,69	14,40	85,32
HgS	hcp	4,14	9,49	14,68	162,88
FeS (a´) LT	hcp	5,96	11,74	65,10	225,21
NiS	hcp	9,59	3,15	165,65	-12,74
Th_7S_{12}	hcp	11,04	3,98	205,82	10,25
CrS	hcp	12,00	11,52	232,41	219,11
Tl_2S	hcp	12,20	18,17	237,95	403,32

7.9.5.4 Orthorhombic structure

Tab. 7-30: Lattice dimension and lattice disregistry of examined sulphides with orthorhombic structure [40,41].

compound	crystallographic structure	lattice dimension [Å]			misfit [%]		
		a	c	b	a	c	b
CuAsS	orthorhombic	3,78	11,47	5,47	4,71	217,73	51,52
InS	orthorhombic	3,93	10,62	4,43	8,86	194,18	22,71
SnS	orthorhombic	3,98	11,18	4,33	10,25	209,70	19,94
$PbSnS_2$	orthorhombic	4,04	11,33	4,28	11,91	213,85	18,56
ThS_2	orthorhombic	4,26	8,60	7,25	18,01	138,23	100,83
GeS	orthorhombic	4,29	3,64	10,42	18,84	0,83	188,64
FeS_2	orthorhombic	4,44	3,83	5,41	22,99	6,09	49,86
SiS_2	orthorhombic	5,60	9,55	5,53	55,12	164,54	53,19
$CuSbS_2$	orthorhombic	6,01	14,46	3,78	66,48	300,55	4,71
$CuBiS_2$	orthorhombic	6,13	14,51	3,89	69,81	301,94	7,76
$CuFe_2S_3$	orthorhombic	6,23	6,46	11,12	72,58	78,95	208,03
$AgBiS_2$	orthorhombic	8,08	5,65	7,82	123,82	56,51	116,62
Np_2S_3	orthorhombic	10,30	3,85	10,60	185,32	6,65	193,63
U_2S_3	orthorhombic	10,39	3,88	10,63	187,81	7,48	194,46
Th_2S_3	orthorhombic	10,97	3,95	10,83	203,88	9,42	200,00
Bi_2S_3	orthorhombic	11,13	3,97	11,27	208,31	9,97	212,19
Ni_6S_5	orthorhombic	11,22	3,27	16,56	210,80	-9,42	358,73
Sb_2S_3	orthorhombic	11,30	3,90	11,50	213,02	8,03	218,56
GeS_2	orthorhombic	11,66	6,86	22,34	222,99	90,03	518,84
Cu_2S (γ)	orthorhombic	11,90	13,41	27,28	229,64	271,47	655,68
Cu_5FeS_4	orthorhombic	21,94	10,97	21,94	507,76	203,88	507,76

7.9.6 Examined oxides

7.9.6.1 Cubic structure

Tab. 7-31: Lattice dimension and lattice disregistry of examined oxides with cubic structure [40,41].

compound	crystallographic structure	lattice dimension [Å]	misfit [%]	rotation of planes, model 1, misfit [%]	rotation of planes, model 2, misfit [%]
		a	(001)	(001)	(001)
ReO_3	cubic	3,75	**3,91**	-26,53	-63,26
γ´-Al_2O_3	cubic	3,96	9,70	-22,43	-61,22
$VO_{0,89-1,20}$	cubic	4,06	12,52	-20,44	-60,22
$UO_{2,82}$	cubic	4,15	14,85	-18,79	-59,40
CrO	cubic	4,16	15,24	-18,52	-59,26
TiO	cubic	4,18	15,85	-18,08	-59,04
NiO	cubic	4,19	16,19	-17,84	-58,92
MgO	cubic	4,21	16,57	-17,58	-58,79
NbO	cubic	4,21	16,64	-17,52	-58,76
CoO	cubic	4,26	18,01	-16,55	-58,28
Cu_2O	cubic	4,26	18,03	-16,54	-58,27
FeO	cubic	4,28	18,56	-16,17	-58,08
ZnO	cubic	4,28	18,56	-16,17	-58,08
TaO	cubic	4,42	22,49	-13,38	-56,69
MnO	cubic	4,44	23,12	-12,94	-56,47
Cr_3O	cubic	4,54	25,87	-10,99	-55,50
CoO	cubic	4,55	26,04	-10,88	-55,44
ZrO	cubic	4,58	26,98	-10,21	-55,11
La_2O_3	cubic	4,63	28,20	-9,35	-54,67
ZnO	cubic	4,63	28,25	-9,31	-54,66
CdO	cubic	4,69	29,94	-8,12	-54,06
Ag_2O	cubic	4,73	31,02	-7,35	-53,68
CaO	cubic	4,80	32,94	-6,00	-53,00
AgO	cubic	4,82	33,41	-5,67	-52,83
MgO_2	cubic	4,84	34,04	-5,22	-52,61
YbO	cubic	4,86	34,63	**-4,81**	-52,40
WO_2	cubic	4,87	34,90	**-4,61**	-52,30
ZnO_2	cubic	4,87	34,93	**-4,59**	-52,29
Ag_2O_3	cubic	4,90	35,84	**-3,94**	-51,97
UO	cubic	4,93	36,57	**-3,43**	-51,72
PuO	cubic	4,96	37,34	**-2,89**	-51,44
PaO	cubic	4,96	37,42	**-2,83**	-51,41
SmO	cubic	4,99	38,18	**-2,29**	-51,15
NpO	cubic	5,01	38,78	**-1,87**	-50,93
W_3O	cubic	5,04	39,50	**-1,36**	-50,68

AmO	cubic	5,05	39,97	**-1,02**	-50,51
ZrO_2	cubic	5,10	41,27	**-0,10**	-50,05
SrO	cubic	5,14	42,37	**0,67**	-49,66
EuO	cubic	5,14	42,49	**0,76**	-49,62
TbO_2	cubic	5,22	44,60	**2,25**	-48,88
CdO_2	cubic	5,31	47,17	**4,07**	-47,97
CmO_2	cubic	5,37	48,81	5,22	-47,39
$SmO_{0,49}$	cubic	5,38	48,93	5,31	-47,35
Pb_2O	cubic	5,39	49,31	5,58	-47,21
Pr_6O_{11}	cubic	5,39	49,36	5,61	-47,19
AmO_2	cubic	5,39	49,39	5,64	-47,18
PuO_2	cubic	5,40	49,47	5,69	-47,15
α-CeO_2	cubic	5,41	49,83	5,95	-47,03
α´-Pu_2O_3	cubic	5,41	49,83	5,95	-47,03
NpO_2	cubic	5,43	50,53	6,44	-46,78
$PbO_{1,5}$	cubic	5,44	50,69	6,56	-46,72
$PrO_{1,83}$	cubic	5,47	51,47	7,10	-46,45
UO_2	cubic	5,47	51,50	7,13	-46,44
PrO_2	cubic	5,47	51,51	7,13	-46,43
NaO_2	cubic	5,49	52,08	7,54	-46,23
PaO_2	cubic	5,52	52,85	8,08	-45,96
BaO	cubic	5,54	53,44	8,50	-45,75
Mo_3O	cubic	5,55	53,71	8,69	-45,65
Na_2O	cubic	5,56	54,02	8,91	-45,55
ThO_2	cubic	5,60	54,99	9,60	-45,20
PoO_2	cubic	5,64	56,15	10,41	-44,79
δ-Bi_2O_3	cubic	5,67	56,93	10,96	-44,52
Pt_3O_4	cubic	5,69	57,62	11,45	-44,27
KO_2	cubic	6,09	68,70	19,29	-40,36
Pt_3O_4	cubic	6,24	72,83	22,21	-38,90
K_2O	cubic	6,45	78,64	26,32	-36,84
Rb_2O	cubic	6,76	87,15	32,33	-33,83
γ-Al_2O_3	cubic	7,86	117,70	53,94	-23,03
Co_3O_4	cubic	8,08	123,90	58,32	-20,84
γ-Fe_2O_3	cubic	8,32	130,47	62,97	-18,52
γ-Ga_2O_3	cubic	8,35	131,30	63,56	-18,22
Fe_3O_4	cubic	8,39	132,52	64,42	-17,79
Rb_2O_3	cubic	9,32	158,17	82,55	-8,72
β-Fe_2O_3	cubic	9,40	160,39	84,12	-7,94
β-Mn_2O_3	cubic	9,41	160,61	84,28	-7,86
δ-Ga_2O_3	cubic	9,52	163,71	86,47	-6,76
Sc_2O_3	cubic	9,86	172,99	93,03	**-3,48**
Cs_2O_3	cubic	9,88	173,68	93,52	**-3,24**
In_2O_3	cubic	10,12	180,27	98,18	**-0,91**
γ-Bi_2O_3	cubic	10,25	183,80	100,67	**0,34**
Lu_2O_3	cubic	10,39	187,83	103,53	**1,76**

Yb_2O_3	cubic	10,43	189,01	104,36	**2,18**
Tm_2O_3	cubic	10,49	190,49	105,41	**2,70**
Er_2O_3	cubic	10,55	192,17	106,59	**3,30**
Tl_2O_3	cubic	10,59	193,35	107,43	**3,72**
Y_2O_3	cubic	10,60	193,69	107,67	**3,83**
Ho_2O_3	cubic	10,61	193,81	107,75	**3,88**
Dy_2O_3	cubic	10,66	195,42	108,89	**4,45**
Tb_2O_3	cubic	10,73	197,20	110,15	5,08
Gd_2O_3	cubic	10,81	199,51	111,78	5,89
Eu_2O_3	cubic	10,86	200,83	112,72	6,36
Sm_2O_3	cubic	10,93	202,77	114,09	7,05
α-Pu_2O_3	cubic	10,95	203,19	114,38	7,19
Cm_2O_3	cubic	11,00	204,71	115,46	7,73
Am_2O_3	cubic	11,03	205,54	116,05	8,02
As_2O_3	cubic	11,07	206,65	116,83	8,42
Nd_2O_3	cubic	11,08	206,93	117,03	8,51
$CeO_{1,67}$	cubic	11,11	207,76	117,62	8,81
Pr_2O_3	cubic	11,14	208,59	118,20	9,10
Sb_2O_3	cubic	11,15	208,86	118,40	9,20
La_2O_3	cubic	11,40	215,79	123,30	11,65
U_4O_9	cubic	21,77	503,05	326,42	113,21

7.9.6.2 Tetragonal structure

Tab. 7-32: Lattice dimension and lattice disregistry of examined oxides with tetragonal structure [40,41].

compound	crystallographic structure	lattice dimension [Å]		misfit [%]		rotation of planes, model 1, misfit [%]	rotation of planes, model 2, misfit [%]
		a	c	(001)	(100)	(001)	(001)
V_4O	tetragonal	2,95	3,48	-18,34	-3,66	-42,26	-71,13
PdO	tetragonal	3,03	5,33	-16,07	47,65	-40,65	-70,33
PtO	tetragonal	3,05	5,35	-15,51	48,20	-40,26	-70,13
Nb_2O	tetragonal	3,39	3,27	-6,18	-9,31	-33,66	-66,83
ZrO_2	tetragonal	3,64	5,27	**0,83**	45,98	-28,70	-64,35
TiO_2	tetragonal	3,79	9,51	**4,85**	163,55	-25,86	-62,93
SnO	tetragonal	3,80	4,83	5,37	33,68	-25,49	-62,74
α-Ta_2O_5	tetragonal	3,81	35,67	5,54	888,09	-25,37	-62,69
PbO	tetragonal	3,97	5,02	10,03	39,00	-22,20	-61,10
TiO	tetragonal	4,19	4,14	16,04	14,68	-17,95	-58,97
CoO	tetragonal	4,26	4,21	18,11	16,71	-16,48	-58,24
GeO_2	tetragonal	4,40	2,86	21,75	-20,78	-13,91	-56,96
β-MnO_2	tetragonal	4,40	2,87	21,80	-20,42	-13,87	-56,94
CrO_2	tetragonal	4,42	2,92	22,49	-19,16	-13,39	-56,69

RuO_2	tetragonal	4,49	3,11	24,38	-13,85	-12,05	-56,03
IrO_2	tetragonal	4,50	3,15	24,65	-12,74	-11,86	-55,93
OsO_2	tetragonal	4,52	3,20	25,21	-11,36	-11,46	-55,73
VO_2	tetragonal	4,53	2,87	25,48	-20,53	-11,27	-55,63
TiO_2	tetragonal	4,59	2,96	27,25	-17,95	-10,02	-55,01
TaO_2	tetragonal	4,71	3,07	30,44	-15,10	-7,76	-53,88
SnO_2	tetragonal	4,74	3,19	31,22	-11,77	-7,21	-53,61
β-BeO	tetragonal	4,75	2,74	31,58	-24,10	-6,96	-53,48
NbO_2	tetragonal	4,78	2,97	32,41	-17,73	-6,37	-53,19
TeO_2	tetragonal	4,80	3,78	32,96	4,71	-5,98	-52,99
MoO_2	tetragonal	4,87	2,80	34,90	-22,55	**-4,61**	-52,30
PbO_2	tetragonal	4,96	3,38	37,26	-6,29	**-2,94**	-51,47
SrO_2	tetragonal	5,03	6,56	39,34	81,72	**-1,48**	-50,74
HfO_2	tetragonal	5,14	5,25	42,38	45,43	**0,68**	-49,66
WO_3	tetragonal	5,27	3,93	46,04	8,84	**3,27**	-48,37
δ-$TiO_{0,5-0,6}$	tetragonal	5,33	6,65	47,73	84,07	**4,46**	-47,77
$U_{0,88}U_{2,13}$	tetragonal	5,38	5,55	49,03	53,74	5,38	-47,31
BaO_2	tetragonal	5,38	6,84	49,14	89,50	5,46	-47,27
Li_2O_2	tetragonal	5,45	7,74	50,83	114,29	6,65	-46,67
PoO_2	tetragonal	5,45	8,36	50,97	131,58	6,75	-46,62
α-KO_2	tetragonal	5,70	6,70	58,01	85,57	11,73	-44,14
Mn_3O_4	tetragonal	5,76	9,44	59,56	161,50	12,82	-43,59
RbO_2	tetragonal	6,01	7,04	66,48	95,01	17,72	-41,14
CsO_2	tetragonal	6,29	7,21	74,24	99,72	23,21	-38,40
NbO_z	tetragonal	6,65	4,90	84,07	35,60	30,16	-34,92
Na_2O_2	tetragonal	6,66	9,93	84,49	175,07	30,45	-34,77
TaO_z	tetragonal	6,68	4,76	85,04	31,80	30,84	-34,58
γ-UO_3	tetragonal	6,89	19,94	90,86	452,35	34,96	-32,52
SiO_2	tetragonal	7,46	8,61	106,65	138,50	46,12	-26,94
γ-Al_2O_3	tetragonal	7,95	7,79	120,22	115,79	55,72	-22,14
γ-Mn_2O_3	tetragonal	8,10	9,40	124,38	160,39	58,66	-20,67
SeO_2	tetragonal	8,37	5,06	131,86	40,19	63,95	-18,03
Cr_3O_4	tetragonal	8,72	7,50	141,55	107,76	70,80	-14,60
Pb_3O_4	tetragonal	8,81	6,56	143,93	81,83	72,49	-13,76
SeO_3	tetragonal	9,64	5,28	166,93	46,26	88,74	-5,63
α-MnO_2	tetragonal	9,82	2,85	171,88	-21,14	92,25	**-3,87**
β-Bi_2O_3	tetragonal	10,95	5,63	203,32	55,96	114,48	7,24
NbO_2	tetragonal	13,70	5,99	279,50	65,84	168,35	34,17
$VO_{1,27}$	tetragonal	16,62	16,52	360,47	357,48	225,60	62,80
Mo_5O_{14}	tetragonal	45,99	3,94	1173,96	9,06	800,83	350,41

7.9.6.3 Hexagonal structure

7.9.6.3.1 (0001) plane

Tab. 7-33: Lattice dimension and lattice disregistry ((0001) plane) of examined oxides with hexagonal structure [40,41].

compound	crystallographic structure	lattice dimension [Å]		misfit [%]
		a	c	(0001)
BeO	hcp	2,70	4,38	5,69
ε-MnO_2	hcp	2,79	4,41	9,14
Ti_2O	hcp	2,96	4,85	15,93
PtO_2	hcp	3,08	4,19	20,66
Al_2O	hcp	3,10	4,99	21,44
Li_2O_2	hcp	3,14	7,65	23,09
CoO	hcp	3,21	5,24	25,75
ZnO	hcp	3,25	1,60	27,30
Gd_2O_3	hcp	3,76	5,89	47,30
Nd_2O_3	hcp	3,82	5,98	49,65
β-Pu_2O_3	hcp	3,84	5,96	50,43
Pr_2O_3	hcp	3,86	6,01	51,18
Ce_2O_3	hcp	3,88	6,06	52,00
β-$CeO_{1,81}$	hcp	3,88	9,54	52,00
γ-$CeO_{1,78}$	hcp	3,91	9,50	53,17
δ-$CeO_{1,72}$	hcp	3,91	9,65	53,25
La_2O_3	hcp	3,94	6,13	54,23
Cs_2O	hcp	4,26	18,99	66,73
Ni_2O_3	hcp	4,61	5,61	80,60
α-Al_2O_3	hcp	4,76	12,99	86,43
V_2O_4	hcp	4,95	14,00	93,99
Cr_2O_3	hcp	4,96	13,60	94,33
δ-$TiO_{0,5\text{-}0,6}$	hcp	4,99	2,88	95,54
δ-Fe_2O_3	hcp	5,10	4,42	99,79
Ti_2O_3	hcp	5,15	13,64	101,71
χ-Al_2O_3	hcp	5,56	13,44	117,81
Zr_3O	hcp	5,63	5,20	120,54
Na_2O_2	hcp	6,21	4,47	143,20
Cs_3O	hcp	8,78	7,52	243,96
η-Al_2O_3	hcp	9,71	17,86	280,39

7.9.6.3.2 (10-10) plane

Tab. 7-34: Lattice dimension and lattice disregistry ((10-10) plane) of examined sulphides with hexagonal structure [40,41].

compound	crystallographic structure	lattice dimension [Å]		misfit [%]	
		a	c	a	c
BeO	hcp	2,70	4,38	-25,26	21,30
ε-MnO_2	hcp	2,79	4,41	-22,83	22,22
Ti_2O	hcp	2,96	4,85	-18,02	34,22
PtO_2	hcp	3,08	4,19	-14,68	16,07
Al_2O	hcp	3,10	4,99	-14,13	38,23
Li_2O_2	hcp	3,14	7,65	-12,96	111,91
CoO	hcp	3,21	5,24	-11,08	45,15
ZnO	hcp	3,25	1,60	-9,99	-55,62
Gd_2O_3	hcp	3,76	5,89	4,16	63,16
Nd_2O_3	hcp	3,82	5,98	5,82	65,65
β-Pu_2O_3	hcp	3,84	5,96	6,37	65,01
Pr_2O_3	hcp	3,86	6,01	6,90	66,43
Ce_2O_3	hcp	3,88	6,06	7,48	67,87
β-$CeO_{1,81}$	hcp	3,88	9,54	7,48	164,27
γ-$CeO_{1,78}$	hcp	3,91	9,50	8,31	163,16
δ-$CeO_{1,72}$	hcp	3,91	9,65	8,37	167,31
La_2O_3	hcp	3,94	6,13	9,06	69,81
Cs_2O	hcp	4,26	18,99	17,89	426,04
Ni_2O_3	hcp	4,61	5,61	27,70	55,40
α-Al_2O_3	hcp	4,76	12,99	31,83	259,86
V_2O_4	hcp	4,95	14,00	37,17	287,87
Cr_2O_3	hcp	4,96	13,60	37,42	276,70
δ-$TiO_{0,5-0,6}$	hcp	4,99	2,88	38,27	-20,24
δ-Fe_2O_3	hcp	5,10	4,42	41,27	22,44
Ti_2O_3	hcp	5,15	13,64	42,63	277,89
χ-Al_2O_3	hcp	5,56	13,44	54,02	272,30
Zr_3O	hcp	5,63	5,20	55,94	43,98
Na_2O_2	hcp	6,21	4,47	71,97	23,80
Cs_3O	hcp	8,78	7,52	143,21	108,31
η-Al_2O_3	hcp	9,71	17,86	168,98	394,74

7.9.6.4 Orthorhombic structure

Tab. 7-35: Lattice dimension and lattice disregistry of examined oxides with orthorhombic structure [40,41].

compound	crystallographic structure	lattice dimension [Å]			misfit [%]		
		a	c	b	a	c	b
Ti_3O_5	orthorhombic	3,76	9,74	9,48	4,02	169,67	162,71
MoO_3	orthorhombic	3,96	3,70	13,86	9,77	2,39	283,80
U_3O_8	orthorhombic	4,15	6,72	11,97	14,90	86,07	231,47
Rb_2O_2	orthorhombic	4,20	5,98	7,08	16,37	65,73	95,98
Cs_2O_3	orthorhombic	4,32	6,43	7,52	19,72	78,12	108,23
β-ReO_2	orthorhombic	4,81	4,60	5,64	33,22	27,43	56,32
Sb_2O_4	orthorhombic	4,81	5,44	11,78	33,35	50,55	226,32
Sb_2O_3	orthorhombic	4,93	5,43	12,49	36,57	50,42	245,98
$PbO_{1,92}$	orthorhombic	4,98	5,44	5,95	37,87	50,80	64,76
SnO	orthorhombic	5,00	11,12	5,72	38,50	208,03	58,45
Fe_3O_4	orthorhombic	5,12	8,39	5,95	41,83	132,35	64,68
Ta_2O	orthorhombic	5,29	3,05	4,92	46,54	-15,51	36,29
PbO	orthorhombic	5,49	5,89	4,78	52,05	63,19	32,27
TeO_2	orthorhombic	5,51	5,60	11,77	52,63	55,12	226,04
CrO_3	orthorhombic	5,74	4,79	8,56	59,09	32,66	137,04
Mn_3O_4	orthorhombic	5,80	9,47	6,36	60,69	162,38	76,07
β-HgO_2	orthorhombic	6,08	4,80	6,01	68,42	32,96	66,48
β-Ta_2O_5	orthorhombic	6,19	3,90	44,02	71,52	7,98	1119,36
β-Ta_2O_5	orthorhombic	6,20	3,89	3,66	71,75	7,76	1,39
γ-Nb_2O_5	orthorhombic	6,24	3,92	43,79	72,85	8,59	1113,02
Np_3O_8	orthorhombic	6,58	4,18	4,09	82,38	15,87	13,19
HgO	orthorhombic	6,61	3,52	5,52	83,16	-2,46	52,91
U_3O_8	orthorhombic	6,70	4,14	11,92	85,71	14,74	230,19
U_3O_{8-x}	orthorhombic	6,72	4,15	3,98	86,14	14,85	10,34
U_2O_5	orthorhombic	6,73	8,29	31,71	86,43	129,64	778,39
K_2O_2	orthorhombic	6,74	6,48	7,00	86,59	79,47	93,93
β-Ta_4O	orthorhombic	7,24	3,22	3,27	100,50	-10,91	-9,34
WO_3	orthorhombic	7,28	3,81	7,45	101,66	5,54	106,37
$PbO_{1,5}$	orthorhombic	7,72	5,50	7,66	113,96	52,41	112,24
$PbO_{1,47-1,51}$	orthorhombic	7,80	7,65	5,50	116,07	111,91	52,35
$PbO_{1,4}$	orthorhombic	7,81	5,52	7,67	116,45	52,80	112,41
Cr_2O_5	orthorhombic	8,47	10,09	12,88	134,63	179,50	256,79
TiO_2	orthorhombic	9,19	5,15	5,45	154,43	42,52	50,89
γ-MnO_2	orthorhombic	9,27	4,53	2,87	156,79	25,57	-20,61
Eu_3O_4	orthorhombic	10,09	3,50	12,07	179,61	-3,05	234,29
V_2O_5	orthorhombic	11,51	4,37	3,56	218,84	21,02	-1,30
Cr_5O_{12}	orthorhombic	12,04	8,18	8,21	233,52	126,59	127,42
Re_2O_7	orthorhombic	15,25	12,50	5,48	322,44	246,26	51,80
$Mo_{17}O_{47}$	orthorhombic	21,62	3,95	19,63	498,75	9,45	443,77

Mo_4O_{11}	orthorhombic	24,49	6,75	5,46	578,39	87,04	51,16
$Nb_{12}O_{29}$	orthorhombic	28,90	20,72	3,84	700,55	473,96	6,23